Non-Polar GaN Epilayers and Heterostructures for Photonic Applications

THÈSE N^{O} 4563 (2009)

PRÉSENTÉE LE 18 DÉCEMBRE 2009

À LA FACULTE SCIENCES DE BASE
LABORATOIRE EN SEMICONDUCTEURS AVANCÉS POUR LA PHOTONIQUE ET L'ÉLECTRONIQUE
PROGRAMME DOCTORAL EN PHOTONIQUE

ÉCOLE POLYTECHNIQUE FÉDÉRALE DE LAUSANNE

POUR L'OBTENTION DU GRADE DE DOCTEUR ÈS SCIENCES

PAR

Tiankai ZHU

acceptée sur proposition du jury:

Prof. O. Martin, président du jury
Prof. N. Grandjean, directeur de thèse
Dr I. Grzegory, rapporteur
Dr E. Richter, rapporteur
Prof. P. Stadelmann, rapporteur

ÉCOLE POLYTECHNIQUE
FÉDÉRALE DE LAUSANNE
Suisse
2009

Abstract

This PhD thesis describes the experimental study of wurtzite III-nitride semiconductors grown on non-polar crystal orientations, namely $(11\bar{2}0)$ *a*- and $(10\bar{1}0)$ *m*-planes. Hindered by poor material quality, they were not as extensively investigated as the polar basal (0001) *c*-plane. Nevertheless, the renewed interest in this topic has been gaining momentum since 2000, thanks to the improvement in material quality. The motivation is to overcome the quantum-confined Stark effect (QCSE) in heterostructures grown on *c*-plane, which is induced by the intrinsic spontaneous and piezoelectric polarization field. QCSE weakens the performance of *c*-plane optoelectronic devices such as light emitting diodes (LEDs) and laser diodes and it can be avoided by growing these devices on non-polar planes. In addition, non-polar LEDs are also featured by the spontaneously polarized light emission and thus have a large potential for liquid crystal display backlighting application.

This thesis includes two aspects:
(1) Since previous study in our laboratory was lacking before this work, the first target was to establish the heteroepitaxial growth procedures for *a*- and *m*-plane GaN layers on *r*- and *m*-plane sapphire substrates, respectively, by hydride vapor phase epitaxy (HVPE). Then, smooth planar templates have been obtained. Particularly, *m*-plane GaN has been demonstrated on *m*-plane sapphire. Further analysis revealed that actually three orientations (two semi-polar and one non-polar) can be grown on *m*-plane sapphire through the modification of sapphire surface chemistry and/or growth procedure. Nevertheless, the material quality of these non-polar templates is inferior to that of *c*-plane as they are characterized by the presence of high-density stacking faults and threading dislocations. To reduce the defect density, epitaxial lateral overgrowth (ELO) technique has been applied. As a result, material quality close to that of planar *c*-plane was achieved in GaN layers overgrown on the mask areas. Overall, the experimental results revealed peculiar characteristics of non-polar orientation, induced by the intrinsic anisotropy of wurtzite structure parallel and perpendicular to the basal plane. It also lays the foundation for further improvement in material quality.

(2) Based on these aforementioned results, the next stage was to investigate the heterostructures grown on those HVPE ELO templates. GaN/AlGaN single quantum wells (QWs) and AlN/GaN distributed Bragg reflectors (DBR) have been grown by NH_3-source molecular beam epitaxy (MBE). The experiments confirm that QWs are free from QCSE and their optical properties are comparable to those grown on planar *c*-plane templates.

Furthermore, nitride-based microcavities (MCs) have been demonstrated on *a*-plane ELO templates. Their optical properties are encouraging and open the way for more sophisticated structure aimed at polariton physics.

In conclusion, non-polar *a*- and *m*-plane GaN planar and ELO templates have been obtained through epitaxy on *r*- and *m*-plane sapphire substrates, respectively, by HVPE. Nanostructures such as QWs, DBRs, and MCs have been grown on non-polar HVPE GaN ELO templates by MBE.

Keywords: Non-polar III-nitride semiconductors, gallium nitride, hydride vapor phase epitaxy, molecular beam epitaxy, epitaxial lateral overgrowth, quantum well, distributed Bragg reflector, microcavity.

Résumé

Ce travail de thèse est consacré à l’étude expérimentale de la croissance et à la caractérisation des semiconducteurs nitrures d’éléments-III en phase wurtzite, et plus précisément, dans leurs plans non-polaires $(11\bar{2}0)\,a$ et $(10\bar{1}0)\,m$. Ces plans cristallographiques n’ont pas été aussi étudiés que le plan c, polaire, principalement en raison de la mauvaise qualité des matériaux obtenus jusqu’ici. Cependant, ces derniers connaissent un regain d’intérêt depuis les années 2000 grâce à l’amélioration de la qualité du matériau, et surtout, de par la possibilité qu’ils offrent de s’affranchir de l’effet Stark confiné quantique (Quantum-Confined Stark Effect, QCSE) présent dans les hétérostructures élaborées sur le plan c. Cet effet est induit par la présence d’une polarisation d’origine spontanée et piézoélectrique, inhérente aux matériaux nitrures d’éléments-III en phase wurtzite. Il en résulte une forte dégradation des performances des dispositifs optoélectroniques telles que les diodes électroluminescentes (LED) et les diodes laser. En outre, les LED non-polaires bénéficient d’une polarisation de l’émission de lumière, et donc présentent un large potentiel pour le rétro éclairage des écrans à cristaux liquides.

Objectifs et réalisations:

(1) L’objectif premier était d’établir des procédures de croissance pour les couches de GaN suivant les plans *a*- and *m*, en utilisant des substrats de saphir d’orientation r- et m- respectivement, et ce par épitaxie en phase vapeur aux hydrures (Hydride Vapor Phase Epitaxy, HVPE). Des couches planaires lisses ont ainsi été obtenues. En particulier, la croissance par cette technique de couches de GaN plan *m* à partir de saphir plan *m*, a été démontrée pour la première fois. En fait, une analyse plus approfondie révèle que trois orientations (deux semi-polaires et une non-polaire) peuvent êtres obtenues sur le saphir plan *m*, en jouant sur la chimie de surface du saphir et/ou des procédures de croissance. Toutefois, la qualité de ces couches est inférieure à celle relevée sur des couches élaborées sur plan *c* . Elles se caractérisent par une forte densité de fautes d’empilement et de dislocations traversantes. Afin de réduire la densité de défauts et de dislocations, la technique de croissance épitaxiale latérale (ELO) a été appliquée. Comme résultat, un matériau de qualité proche de celle du plan *c* est obtenu dans les régions se situant au dessus des masques. Dans l'ensemble, les résultats expérimentaux mettent en évidence la spécificité de l’orientation non-polaire, induite par l'anisotropie intrinsèque du plan basal. Ils fixent également les bases pour l’amélioration de la qualité du matériau.

(2) Basée sur les résultats en (1), l’ étape suivante a été d'étudier les hétérostructures obtenues par croissance par épitaxie par jets moléculaires (molecualr beam epitaxy, MBE) à

base de NH_3 sur les couches de GaN ELO élaborées par HVPE. Des puits quantiques GaN/AlGaN et des miroirs de Bragg AlN/GaN ont ainsi été. Les expériences confirment que les puits quantiques sont exempts de tout champ électrique (pas de QCSE) et leurs propriétés optiques sont comparables à celles observées sur plan *c*. En outre, des microcavités présentant des facteurs de qualité satisfaisants ont été réalisées. Ces résultats préliminaires ouvrent ainsi la voie à des structures plus sophistiquées visant la physique des polaritons.

Mots-clés : Non-polaire, semiconducteurs nitrures d'éléments-III, nitrure de gallium, épitaxie en phase vapeur aux hydrures, épitaxie par jet moléculaire, épitaxie latérale, puits quantiques, miroir de Bragg, microcavité.

Contents

Introduction

General background and motivation

The research on III-V nitride semiconductors (*i.e.* GaN, AlN, InN and their related ternary alloys) has evolved rapidly in the past two decades. Within such a broad field, this thesis focuses on epilayers and heterostructures grown on specific crystal orientations, namely $\{11\bar{2}0\}$ *a*- and $\{10\bar{1}0\}$ *m*-planes. These planes are referred to as the non-polar planes, in comparison to the polar $\{0001\}$ *c*-plane.

Before digging into further details, let us take a brief look at history. Although AlN was first synthesized by J. W. Mallets in 1877, it is GaN that plays a predominant role in the history of III-V nitrides. The story began about forty years ago, when pioneers like H. P. Maruska *et al.*[1] (1969) and M. Ilegems *et al.*[2, 3] (1971) initiated the study of GaN epitaxy on sapphire substrates by hydride vapor phase epitaxy (HVPE). After that, the lack of good-quality GaN epilayers and *p*-type conductivity hindered further progress for over a decade. The breakthroughs occurred in the late 1980s, when the research group led by I. Akasaki solved these two critical issues: (1) they used metalorganic vapor phase deposition (MOVPE) with an AlN buffer layer to grow high-quality GaN epilayers on sapphire substrates (1986)[4] and (2) they obtained high *p*-type doping (1989)[5]. Since the demonstration of nitride-based high-brightness blue light emitting diodes (LEDs) (1993)[6] and blue laser diodes (LDs) (1996)[7] by S. Nakamura at Nichia (Japan), the scientific research on III-V nitrides has been mainly driven by the booming industry towards wide commercial applications in photonics (*e.g.* LEDs and LDs) and electronics (*e.g.* high-power/high frequency transistors). The market has already reached several billions US dollars and is still growing rapidly.

Nevertheless, there are some obstacles in the road ahead. Until now, research has been largely concentrated on polar *c*-plane GaN crystal orientation, for which significant achievements have been obtained. However, photonic devices grown on this plane suffer from the quantum confined Stark effect (QCSE), arising from the polarization-induced electrostatic field in heterostructures grown along *c*-axis, which limits the efficiency of devices.[*]

In theory, one obvious solution is to grow devices on non-polar *a*- or *m*-planes, where the polar *c*-axis is parallel to the surface.[8] Non-polar LEDs and LDs have been fabricated on high quality bulk GaN substrates, with much improved and quite encouraging performance.[9, 10] In addition to the elimination of QCSE, non-polar LEDs are also featured by spontaneously polarized light emission, which has the potential for liquid crystal display (LCD) backlighting applications.[11]

Non-polar devices with high performance require GaN templates with good material quality. Bulk GaN would be the best choice. Unfortunately, its availability is still marginal as GaN single crystals are usually limited to small size (~ 1 cm^2) and not mass-commercially available. In substitution, thick GaN epilayers are first grown on foreign substrates (*e.g.* single

---

[*] More information about QCSE will be presented in Chapter 1, section 4.

crystal sapphire) and then are separated from the substrate to form free-standing GaN wafers with dislocation density of the order of 10^6 cm^{-2}. Through heteroepitaxy, many efforts, including this thesis, have been devoted to solving the problem of QCSE by growing non-polar III-nitride templates on specific foreign substrates.

Just like the old saying “the devil is in the details”, an obvious solution may not necessarily be an easy one. Nitrides are different in structure from common III-V compound semiconductors like GaAs or InP. This difference leads to some unique, bittersweet properties: bitter for “growers” who pursue perfect material quality and sweet for “characterizers” because there are things that are rarely observed in defect-free GaAs and Si epilayers. Readers may agree with me on that point as both sides are presented in this thesis. Particularly, nitrides are anisotropic in the sense that parameters parallel and perpendicular to the basal *c*-plane are different. That peculiarity alone makes growing nitrides on non-polar orientations quite complicated.

State of the art before this PhD thesis

Two aspects are concerned here:

(1) From the crystal growth point of view, the history of non-polar GaN heteroepitaxy is as long as that of polar one, as *a*-plane was often discussed together with *c*-plane in some early works.[12, 13] However, its material quality was quite poor, featured by rough surface. The real breakthrough came in 2000, when K. H. Ploog’s group reported *m*-plane GaN grown on (100) $LiAlO_2$ by molecular beam epitaxy (MBE). For the first time, the surface was smooth enough to enable the growth of heterostructures with sharp interfaces. After that and before this thesis, several groups reported planar *a*-plane GaN epilayers grown on sapphire and SiC,[14, 15] and *m*-plane GaN grown on $LiAlO_2$[16, 17]. Their material quality was not as good as that of standard *c*-plane GaN grown on *c*-plane sapphire: the densities of threading dislocations (TDs) and stacking faults (SFs) were of the order of 10^{10} cm^{-2} and 10^5 cm^{-1}, respectively.[14] To reduce the defect density, methods such as single-step epitaxy lateral overgrowth (ELO)[18] and selective area ELO[19] techniques have been employed.

Besides, there is another problem concerning $LiAlO_2$ substrate used for *m*-plane GaN heteroepitaxy. It is not thermally stable under common GaN MOVPE/HVPE growth environment (T ~ 1000 °C and H_2/NH_3 gas), and it may decompose and thus introduce impurities. *M*-plane sapphire could be a better choice. However, GaN epilayers grown on *m*-plane sapphire by HVPE were reported to be of semi-polar orientations, *i.e.* $(10\bar{1}3)$ and $(11\bar{2}2)$ planes.[20] More information about heteroepitaxy of non-polar GaN layers can be found in the feature article by B. A. Haskell *et al.*[21]

(2) From optical properties point of view, non-polar nanostructures have been grown on planar and ELO templates, mostly multiple quantum wells (MQWs). Characterizations show that they are free from QCSE.[22, 23] Furthermore, visible[24] and UV[25] LEDs have been demonstrated on these templates. However, their performance is lower than that of *c*-plane LEDs due to inferior material quality.

Reports on advanced nanostructures other than MQWs were lacking. One of them is nitride-based microcavity (MC). MC is a structure composed of a cavity layer, sandwiched by two distributed Bragg reflectors (DBRs). It is also one of our group's main research topics.[26] Actually, a new class of light emitters called polariton laser, based on strong light-matter interaction (the so-called strong coupling regime), has lately been demonstrated to be achievable using high-quality nitride-based polar MC.[27] But the QCSE still plays a detrimental role in such system and thus it is worth developing non-polar MCs to take advantage of the absence of QCSE. More details will be given in chapter 4, section 4.

Objectives

The first goal is to establish HVPE growth of non-polar GaN epilayers with reasonable material quality on sapphire substrates. This provides not only some insights about the influence of various growth parameters, but also the templates for the next-step investigations of heterostructures grown by MBE. For *a*-plane GaN grown on *r*-plane sapphire, since several groups had already reported relevant results before this thesis, the point is mainly about optimization. As for *m*-plane GaN, the study endeavors to grow it on a cost-effective and thermally-stable substrate like sapphire.

Once the templates are ready, the following step is to prepare heterostructures like QWs and DBRs by NH_3-source MBE. The tasks are to optimize the growth parameters and to investigate the structural and optical properties. They also serve as preliminary steps for more sophisticated structures aimed at polariton physics.

Context

This work was conducted in our laboratory from 2005 to 2009, except the characterizations of transmission electron microscopy (TEM) and cathodoluminescence (CL). TEM studies were completed in collaboration with research groups at Interdisciplinary Center for Electron Microscopy (CIME) of EPFL and Centre de Recherche sur l'Hétéroépitaxie et Ses Applications (CRHEA) of Centre National de la Recherche Scientifique (CNRS) in France. CL investigations were conducted at Laboratory of Quantum Electronics (LOEQ) of EPFL. This work was funded by the National Centre of Competence in Research Quantum Photonics (NCCR QP) of Swiss National Science Foundation (SNSF) and the Sandoz Family Foundation.

Outline

Chapter 1 provides some fundamental knowledge about nitride semiconductor properties, *i.e.* structural and optical parameters, with an emphasis on the aforementioned unique anisotropy. It also introduces one of the main issues of nitride-based photonics that gives rise to this thesis: the QCSE. Since GaN are heteroepitaxially grown on sapphire substrates, some specificities about sapphire crystal, especially *r*- and *m*-planes, are included as well. The information is helpful for readers to have a better understanding of the following chapters.

This thesis is mainly about experimental work, so Chapter 2 briefly explains the experimental techniques employed. They are categorized into two types: (1) epitaxial growth techniques, namely HVPE and MBE; (2) techniques that allow to characterize various aspects of the samples. One may see the whole picture by combining these complementary data together.

Chapters 3 and 4 are the "results and discussion" part for the samples grown by HVPE and MBE, respectively. Chapter 3 focuses purely on HVPE GaN templates and its four sections are divided into two halves, according to the crystal orientations. The first half deals with *a*-plane GaN: 3.1 for planar templates and 3.2 for ELOs; and the second half with *m*-plane GaN (3.3 planar and 3.4 ELO). Particularly, since three different GaN crystal orientations (two semi-polar and one non-polar) can be grown on *m*-plane sapphire, part of section 3.3 is assigned to a discussion of this issue. Chapter 4 deals with two aspects: sections 4.1 & 4.2 are about the epitaxy of non-polar GaN layers; 4.3 & 4.4 describe heterostructures grown on ELO templates: 4.3 for single QWs and 4.4 for DBR and MC.

Bibliography

---

[1] H. P. Maruska and J. J. Tietjen, “The preparation and properties of vapor-deposited single-crystalline GaN”, *Applied Physics Letters*, vol. 15, no. 10, pp. 327-329, 1969.

[2] R. Dingle, D. D. Sell, S. E. Stokowski, M. Ilegems, “Absorption, reflectance and luminescence of GaN epitaxial layers”, *Physical Review B*, vol. 4, no. 4, pp. 1211-1218, 1971.

[3] M. Ilegems, “Vapor epitaxy of gallium nitride”, *Journal of Crystal Growth*, vol. 13/14, pp. 360-364, 1972.

[4] H. Amano, N. Sawaki, I. Akasaki, Y. Toyoda, “Metalorganic vapor phase epitaxial growth of a high quality GaN film using an AlN buffer layer”, *Applied Physics Letters*, vol. 48, no. 5, pp. 353-355, 1986.

[5] H. Amano, M. Kito, K. Hiramatsu, I. Akasaki, “p-type conduction in Mg-doped GaN treated with low-energy electron beam irradiation (LEEBI)”, *Japanese Journal of Applied Physics*, Part 2 (Letters), vol. 28, no. 12, pp. L2112-14, 1989.

[6] S. Nakamura, M. Senoh, and T. Mukai, “High-power InGaN/GaN double-heterostructure violet light emitting diodes”, *Applied Physics Letters*, vol. 62, no. 19, pp. 2390-2392, 1993.

[7] S. Nakamura, M. Senoh, S. Nagahama, N. Iwasa, T. Yamada, T. Matsushita, H. Kiyoku, and Y. Sugimoto, “InGaN multi-quantum-well structure laser diodes grown on $MgAl_2O_4$ substrates”, *Applied Physics Letters*, vol. 68, no. 15, pp. 2105-2107, 1996.

[8] P. Waltereit, O. Brandt, A. Trampert, H. T. Grahn, J. Menniger, M. Ramsteiner, M. Reiche, and K. H. Ploog, “Nitride semiconductors free of electrostatic fields for efficient white light-emitting diodes”, *Nature*, vol. 406, pp. 865-868, 2000.

[9] K. Okamoto, H. Ohta, S. F. Chichibu, J. Ichihara, and H. Takasu, “Continuous-wave operation of m-plane InGaN multiple quantum well laser diodes”, *Japanese Journal of Applied Physics*, vol. 46, no. 9, pp.L187-L189, 2007.

[10] K. Iso, H. Yamada, H. Hirasawa, N. Fellows, M. Saito, K. Fujito, S. P. DenBaars, J. S. Speck, and S. Nakamura, “High brightness blue InGaN/GaN light emitting diode on nonpolar *m*-plane bulk GaN substrate”, *Japanese Journal of Applied Physics*, vol. 46, no. 40, pp.L960-L962, 2007.

[11] H. Masui, H. Yamada, K. Iso, J. S. Speck, S. Nakamura, and S. P. DenBaars, “Non-polar-oriented InGaN light-emitting diodes for liquid-crystal-display backlighting”, Journal of the Society for Information Display, vol. 16, no. 4, pp. 571-578, 2008.

---

[12] H. P. Maruska, L. J. Anderson, and D. A. Stevenson, “Microstructural observations on gallium nitride light-emitting diodes*”, Journal of Electrochemical Society: solid-state science and technology*, vol. 121, no. 9, pp. 1202-1207, 1974.

[13] M. Sano and M. Aoki, “Epitaxial growth of undoped and Mg-doped GaN”, *Japanese Journal of Applied Physics*, vol. 15, no. 10, pp. 1943-1950, 1976.

[14] T. Paskova, V. Darakchieva, P. P. Paskov, J. Birch, E. Valcheva, P. O. A. Persson, B. Arnaudov, S. Tungasmitta, and B. Monemar, “Properties of nonpolar a-plane GaN films grown by HVPE with AlN buffers”, *Journal of Crystal Growth*, vol. 281, no. 1, pp. 55-61, 2005.

[15] M. D. Craven, F. Wu, A. Chakraborty, B. Imer, U.K. Mishra, S. P. DenBaars, and J. S. Speck, “Microstructural evolution of a-plane GaN grown a-plane SiC by metalorganic chemical vapor deposition”, *Applied Physics Letters*, vol. 84, no. 8, pp. 1281-1283, 2004.

[16] B. A. Haskell, A. Chakraborty, F. Wu, H. Sasano, P. T. Fini, S. P. DenBaars, J. S. Speck, and S. Nakamura, “Microstructure and enhanced morphology of planar nonpolar *m*-plane GaN grown by hydride vapor phase epitaxy”, *Journal of Electronic Materials*, vol. 34, no. 4, pp. 357-360, 2005.

[17] Y. Dikme, P. van Gemmern, B. Chai, D. Hill, A. Szymakowski, H. Kalisch, M. Heuken, and R. H. Jansen, “Growth studies of GaN and alloys on $LiAlO_2$ by MOVPE”, *physica. status. solidi. (c)*, vol. 2, no. 7, pp. 2161-2165, 2005.

[18] B.A. Haskell, F.Wu, M.D. Craven, S. Matsuda, P.F. Fini, T. Fujii, K. Fujito, S.P. DenBaars, J.S. Speck, S. Nakamura, “Defect reduction in $(11\bar{2}0)$ a-plane gallium nitride via lateral epitaxial overgrowth by hydride vapor-phase epitaxy”, *Applied Physics Letters*, vol. 83, no. 4, pp. 644-646, 2003.

[19] C. Chen, J. Zhang, J. Yang, V. Adivarahan, S. Rai, S. Wu, H. Wang, W. Sun, M. Su, Z. Gong, E. Kuokstis, M. Gaevski, M. A. Khan, “A new selective area lateral epitaxy approach for depositing a-plane GaN over r-plane sapphire”, *Japanese Journal of Applied Physics*, vol. 42, no. 7B, pp. L818-820, 2003.

[20] T. J. Baker, B. A. Haskell, F. Wu, J. S. Speck, and S. Nakamura, “Characterization of planar semipolar gallium nitride films on sapphire substrates”, *Japanese Journal of Applied Physics*, vol. 45, no. 6, pp. L154-L157, 2006.

[21] B. A. Haskell, S. Nakamura, S. P. DenBaars, and J. S. Speck, “Progress in the growth of nonpolar gallium nitride”, *physica. status. solidi. (b)*, vol. 244, no. 8, pp. 2847-2858, 2007.

[22] A. Chakraborty, S. Keller, C. Meier, B. A. Haskell, S. Keller, P. Waltereit, S.P. Denbaars, S. Nakamura, J.S. Speck, U. K. Mishra, “Properties of nonpolar *a*-plane InGaN/GaN multiple quantum wells grown on lateral epitaxially overgrown *a*-plane GaN”, *Applied Physics Letters*, vol. 86, no. 3, pp. 031901, 2005.

[23] Y. J. Sun, O. Brandt, S. Cronenberg, S. Dhar, H. T. Grahn, and K. H. Ploog, “Nonpolar InGaN/GaN$(1\bar{1}00)$ multiple quantum wells grown on γ-LiAlO2(100) by plasma-assisted molecular-beam epitaxy”, *Physical Review B*, vol. 67, no. 04, pp. 041306, 2003.

---

[24] A. Chitnis, C. Chen, V. Adivarahan, M. Shatalov, E. Kuokstis, V. Mandavilli, J. Yang, M.A. Khan, “Visible light-emitting diodes using a-plane GaN-InGaN multiple quantum wells over r-plane sapphire”, *Applied Physics Letters*, vol. 84, no. 18, pp. 3663-3665, 2004.

[25] C. Chen, V. Adivarahan, J. Yang, M. Shatalov, E. Kuokstis, M.A. Khan, “Ultraviolet light emitting diodes using non-polar a-plane GaN-AlGaN multiple quantum wells”, *Japanese Journal of Applied Physics*, vol. 42, no. 9A/B, pp. L1039-1040, 2003.

[26] G. Christmann, PhD Thesis “III-Nitride based microcavities: towards polariton condensation at room termperature”, EPFL_TH4285, 2008.

[27] S. Christopoulos, G. Baldassarri Höger von Högersthal, A. J. D. Grundy, P. G. Lagoudakis, A. V. Kavokin, J. J. Baumberg, G. Christmann, R. Butté, E. Feltin, J.-F. Carlin, and N. Grandjean, “Room-temperature polariton lasing in semiconductor microcavities”, *Physical Review Letters*, vol. 98, no. 12, pp. 126405, 2007.

1. Overview of Basic Elements

There are two general aspects concerning the information provided in this chapter. First, from the crystal point of view, III-nitrides have some uncommon properties, compared to the classic III-Vs (*e.g.* GaAs and InP). Secondly, for epitaxy (either hetero- or homo-), GaN *a*- and *m*-planes do not behave exactly the same way as the conventional *c*-plane does, because the crystal structure is different between polar and non-polar orientations. In addition, the surfaces of *r*- and *m*-plane sapphire are different from that of *c*-plane.

Therefore, fundamental knowledge of III-nitrides is prerequisite. This chapter emphasizes the peculiarities of non-polar orientations. To have a better understanding of heteroepitaxy, the structural properties of sapphire will be briefly exposed. Further information can be found in the bibliography.

1.1 Structural properties of III-nitrides

III-nitride binary compound semiconductors (*e.g.* GaN, AlN, and InN) crystallize in either the wurtzite (2H) or the zincblende (3C) structures. The former – wurtzite, which possesses the hexagonal symmetry, is the stable phase. The nitrides discussed in this thesis are of wurtzite structure. Its space group is $P6_3mc$ in Hermann-Mauguin notation or C_{6v}^4 in Schoenflies notation. Its unit cell model is shown in figure 1.1.

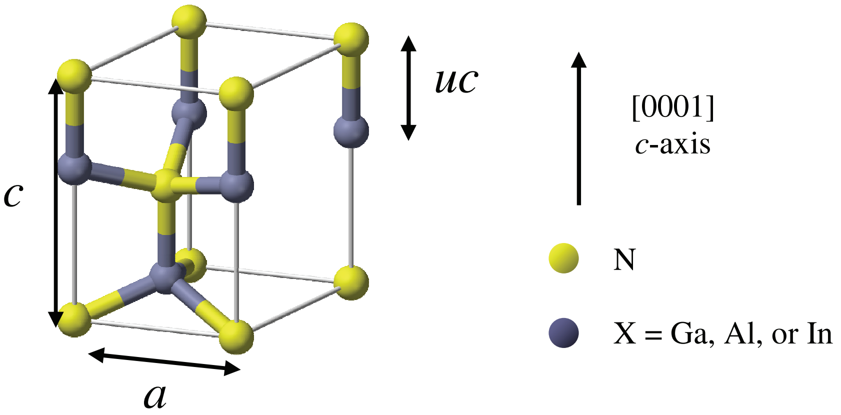

Figure 1.1 A 3D ball-stick model of the unit cell of wurtzite nitrides, with lattice parameters ***a***, ***c*** and internal displacement parameter ***u***. Yellow balls are nitrogen atoms, and grey ones are group III X atoms (X = Ga, Al, or In).

Wurtzite structure consists of two embedded hexagonal stacks ABABAB… along the [0001] direction "*c*-axis" (figure 1.1), also referred to as hexagonal close packed (*hcp*). It is different from the stack sequence ABCABC… of the zincblende (111) plane of cubic semiconductors like GaAs. In the hexagonal structure, the lattice parameter in (0001) plane – edge length ***a*** is distinct from the one along [0001] direction – prism height ***c***, indicating that nitrides are anisotropic crystals. Indeed, such anisotropy gives rise to some unique properties and will be referred to from time to time in this thesis. The internal displacement parameter ***u*** is defined as the anion-cation bond length along *c*-axis, in the unit of *c*. The values of ***a***, ***c*** and ***u*** for bulk GaN, AlN and InN at room temperature are listed in table 1.1.

In general, the lattice mismatches of III-nitrides are larger than those of the classic III-Vs. For instance, *c*-plane AlN thin films deposited on GaN layer are likely to be under biaxial tensile strain, which arises from the mismatch of lattice parameters of ~ 2.4%. In comparison, GaAs and AlAs are almost lattice-matched (~ 0.1%).

Normally, III-nitrides are grown at temperatures much higher than the room temperature. For example, epitaxy of GaN is usually conducted at T = 600 – 1000 °C for hydride vapor phase epitaxy (HVPE) and metalorganic vapor phase epitaxy (MOVPE), and T = 450 – 800 °C for molecular beam epitaxy (MBE). Thus, the thermal expansion in solids has to be taken into account. The thermal expansion coefficients (TECs) of III-nitrides are listed in table 1.1. There is always a mismatch of TECs between the epilayer and the substrate in the case of heteroepitaxy. This fact has to be considered together with the lattice mismatch.

Parameters (T = 300 K)	GaN	AlN	InN
a (Å) [1]	3.189	3.112	3.545
c (Å) [1]	5.185	4.982	5.703
u [2]	0.376 c	0.380 c	0.377 c
TEC (10^{-6} K^{-1}) [3]	a 5.59 / c 3.17	a 4.15 / c 5.27	–

Table 1.1 Lattice constants, internal displacement parameters, and TECs of the three wurtzite III-nitride binary compounds.

A close look at the unit cell reveals that the wurtzite structure is non-centrosymmetric, as there is an asymmetry along *c*-axis. It is referred to as *polarity* of the layer, defined by the direction of the III-N bonds parallel to *c*-axis. For example, *c*-plane GaN layer is called Ga-face or +*c* when N atom is on top of Ga; in reverse, it is N-face or –*c* (figure 1.2). The {0001} *c*-planes are usually referred to as "polar" ones. They are the most-extensively studied orientations for III-nitrides and often serve as reference in this thesis.

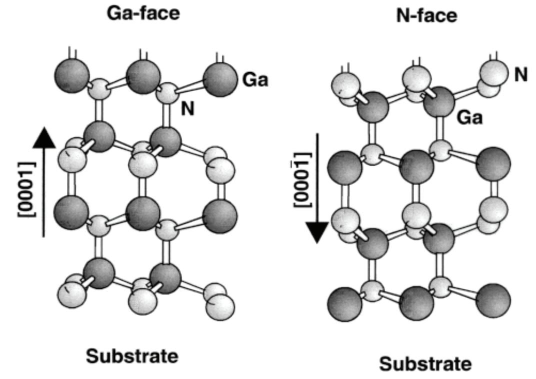

Figure 1.2 Ga- and N-face of wurtzite GaN crystal along *c*-axis, after O. Ambacher[3].

In addition to polar *c*-plane, there are two other important types of crystal planes: the non-polar and the semi-polar. The non-polar, the main objective of this thesis, corresponds to planes with $l = 0$ in the standard Miller-Bravais notation $\{hkil\}$, *i.e.* $\{11\bar{2}0\}$ *a*- and $\{10\bar{1}0\}$ *m*-planes. They are perpendicular to the polar *c*-plane, as shown in figure 1.3 (a). The angle between two neighboring crystal directions from the same set, say $[10\bar{1}0]$ and $[1\bar{1}00]$, is 60°; and the angle between the adjacent two directions, say $[10\bar{1}0]$ and $[11\bar{2}0]$, is 30° [figure 1.3 (b)]. The semi-polar are the planes with nonzero h or k and nonzero l, *e.g.* $(10\bar{1}\bar{3})$

and $(11\bar{2}2)$. They are out of the scope of this thesis, though sometimes they will be mentioned in later chapters.

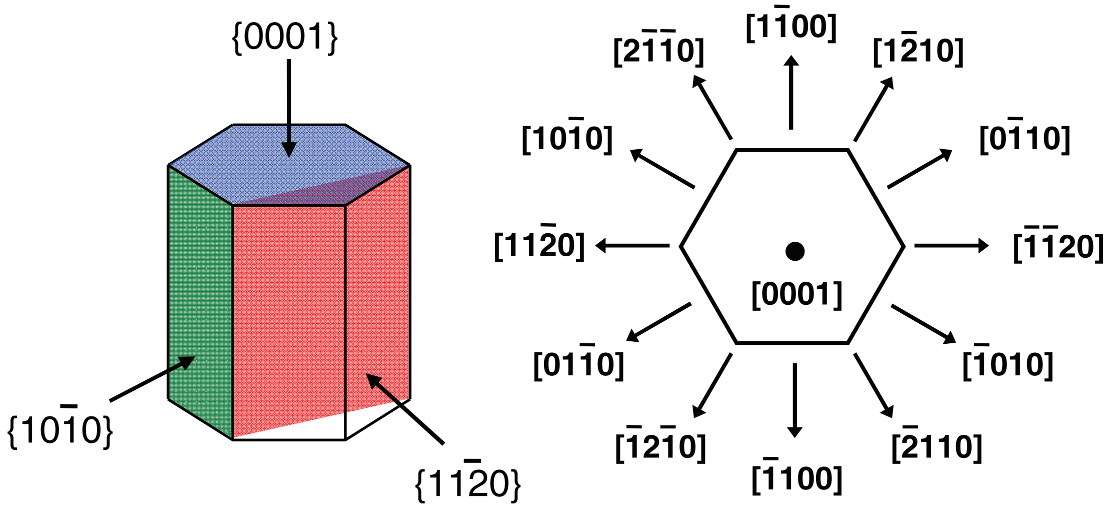

(a) (b)

Figure 1.3 (a) Diagram of the crystal planes of III-nitrides, and (b) top view of the wurtzite (0001) plane, where non-polar $<11\bar{2}0>$ and $<10\bar{1}0>$ directions are marked.

For *a*- and *m*-planes, each has equal numbers of threefold-coordinated III (*e.g.* Ga) and N in the surface layer, so that charge neutrality can be obtained without changing the stoichiometry (figure 1.4). For GaN, Ga and N atoms form a dimer structure (Ga-N), which is theoretically more stable than Ga-Ga or N-N dimers, especially under N-rich growth condition.[4]

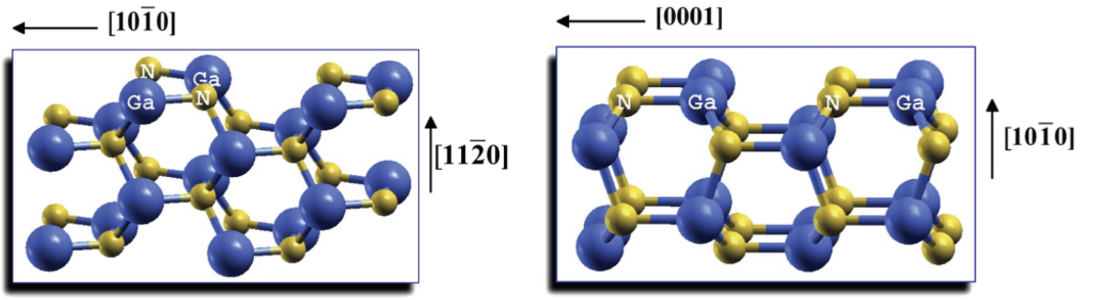

Figure 1.4 Side view of the ball-and-stick model of the nonpolar (a) *a*- and (b) *m*-plane surfaces. Large balls (blue) are Ga, and small balls (yellow) are N, after D. Segev *et al.*[5]

1.2 Typical defects in nitride epilayers

Defects in crystalline solids are imperfections of the regular arrangements of atoms. They are classified as point, linear, planar, and volume defects by the geometry. They have negative impacts on the material quality and reduce the performance of the devices. Compared to Si or GaAs wafers, the state-of-the-art nitride templates are characterized by high defect density. Two common types will be introduced here: basal-plane stacking faults and threading dislocations.

1.2.1 Basal-plane stacking faults

Basal-plane stacking faults (BSFs) are planar defects that interrupt the regular stacking sequence along *c*-axis by introducing one or more faulted planes to the stacking rules. In theory, there are four kinds of BSFs in wurtzite structure[6] – intrinsic type-I (I_1), type-II (I_2), type-III (I_3) and extrinsic (E), as shown in figure 1.5. I_1 contains only one violation of the stacking rule and is expected to have the lowest formation energy. Figure 1.5 (a) displays a BSF (…AaBbCcBb…) followed by a certain number of layers in the new stacking sequence, and then another I_1 BSF (…CcBbAaBb…) reverts the stacking sequence to the original order. I_2 contains two violations of the stacking rule (…AaBbCcAa…) and has the second lowest formation energy. I_3 can be treated as a special case of I_1, *i.e.* the new stacking plane number is reduced to one. However, I_3 is usually not reported in the literatures. Extrinsic BSFs have an additional Cc layer inserted into the normal stacking sequence …AaBbCcAaBb….

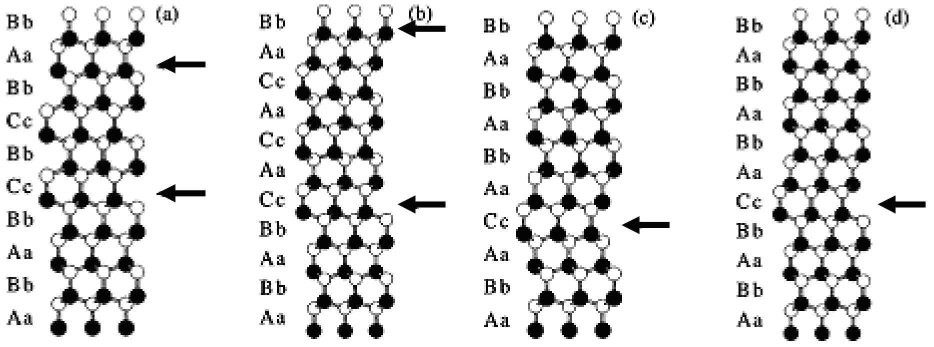

Figure 1.5 Four types of SFs (a) I_1, (b) I_2, (c) I_3, and (d) E. The arrows indicate the position of BSFs, after Ref. 6.

The "wrong" …AaBbCc… stacking sequences are equivalent to those of cubic GaN along [111] direction and can be viewed as a "zinc-blende region" surrounded by the hexagonal structure. It is calculated that BSFs are potential wells for electrons and potential barriers for holes, forming a shallow and thin type-II quantum well (QW).[7]

1.2.2 Threading dislocations

Threading dislocations (TDs) are linear defects. They are characterized by Burgers vector $\vec{b}$ and dislocation line $\vec{u}$. There are three types of dislocations normally associated with hexagonal materials, namely *a* type with Burgers vector $\vec{b} = \frac{1}{3} < 11\bar{2}0 >$, *c* type with $\vec{b}$ =

$< 0001 >$, and *a*+*c* type with $\vec{b} = \frac{1}{3} < 11\bar{2}3 >$. Since dislocations tend to follow the growth direction, for example, in the case of *a*-plane GaN, they are often referred to as edge (*c* type), screw (*a* type), and mixed (*a*+*c* type).

TDs can split into partial dislocations: Frank-Shockley, Shockley and Frank types, and BSFs are often bounded by them. When Burgers vector $\vec{b}$ is parallel to the plane of BSFs, the partial dislocations are of Shockley type; when $\vec{b}$ is perpendicular to the plane of SFs, they are called Frank type. A comprehensive introduction to dislocations can be found in the book of D. Hull and D. J. Bacon.[8] Besides, stair rods form where BSFs and prismatic SFs (PSFs) intersect. The dislocation types found in III-nitride layers are summarized in table 1.2.[9] The image on the right is a schematic drawing of Burgers vectors of TDs and partial dislocations.[10] More details about dislocations in GaN are available in the report of D. Cherns and M. E. Hawkridge.[11]

Dislocation	Burgers vector $\vec{b}$	Bounds
a type	$\frac{1}{3} < 11\bar{2}0 >$	None
c type	$< 0001 >$	None
a+*c* type	$\frac{1}{3} < 11\bar{2}3 >$	None
Frank-Shockley	$\frac{1}{6} < 2\bar{2}03 >$	I_1-type BSFs
Shockley	$\frac{1}{3} < 1\bar{1}00 >$	I_2-type BSFs
Frank	$\frac{1}{2} < 0001 >$	*E* BSFs
Stair rod	$\frac{1}{6} < 10\bar{1}0 >$ $/\frac{1}{6} < 3\bar{2}\bar{1}0 >$	BSFs/PSFs

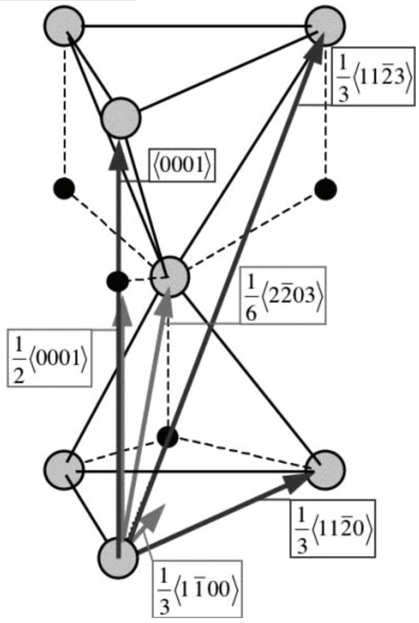

Table 1.2 Summary of dislocation types found in hexagonal nitrides, after Ref. 9. The image on the right is a schematic drawing of Burgers vectors in the wurtzite structure. Dark and grey arrows indicate those vectors of TDs and partial dislocations, respectively. The dash lines are the atomic bonds, after Ref.10.

Generally speaking, three types of GaN templates are available now, with various dislocation densities: (1) planar GaN grown on sapphire or silicon substrates by MOVPE or HVPE with density 10^8-10^9 cm^{-2}; ELO GaN with density ~ 10^7 cm^{-2}; and freestanding GaN with density < 5×10^6 cm^{-2}.

1.2.3 Defect reduction technique – epitaxial lateral overgrowth

Epitaxial lateral overgrowth (ELO) is a kind of selective vapor-phase deposition technique. It has been widely used in a variety of semiconductor materials like Si,[12] GaAs,[13] and GaN.[14] There are a few types of ELO: the standard single-step, the two-step, and the pendeo-epitaxy. In this thesis, only the first one is used. The process of single-step ELO is presented in figure 1.6: (a) first, part of the substrate is covered by a mask (*e.g.* dielectric materials such as SiO_2 or SiN_x); (b) then, the material is deposited selectively on the unmasked areas – the so called windows. The growth conditions (temperatures, pressures, and etc.) are optimized, *i.e.* the super-saturation of the growth species on the mask areas is low enough to avoid deposition on the mask, whereas the nucleation barrier on the window areas is overcome in order to facilitate the growth; (c) after the windows are filled, growth continues both laterally and vertically over the mask areas. A faster lateral growth rate can be achieved by taking advantage of the growth anisotropy, as the growth rates on different crystallographic planes are not the same. The growth anisotropy is affected by not only the growth conditions but also the ratio between the mask and window areas (fill factor), which locally determines the distribution of the growth species. The vertical fronts of the overgrown layer coalesce to form a smooth surface, suitable for device fabrication on top of it.

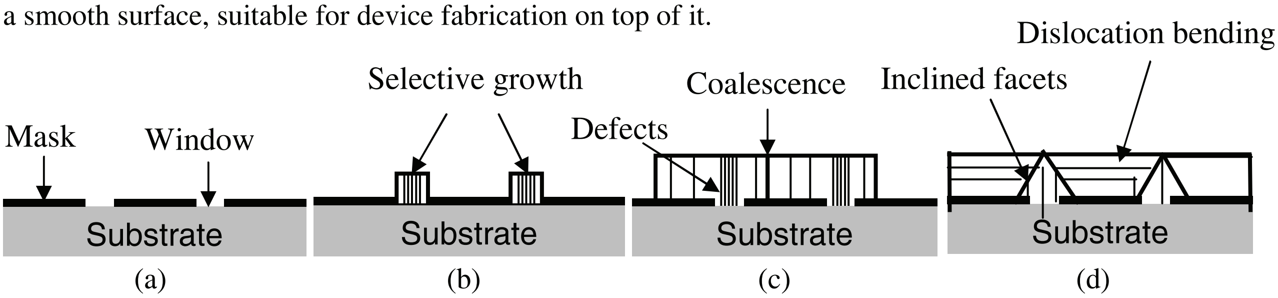

Figure 1.6 Schematic presentation of (a) – (c) the standard single-step ELO process and (d) the inclined-facet ELO process.

Single-step ELO is a conventional method to reduce defects in GaN layers, thanks to a simple defect filtering mechanism: the masks cover part of the substrate and thus the defects beneath cannot propagate vertically. Therefore, the laterally-grown GaN over the mask should be nearly free of defects, but the defect density of GaN in the windows is the same as that of the substrate.

In addition, there is another kind of ELO process used for *c*-plane GaN, which takes advantage of the dislocation-bending phenomenon, as shown in figure 1.6 (d).[15] It first develops an inclined facet and forms an apex. Then, coalescence and surface smoothing are achieved by increasing the temperature or introducing (MeCp)Mg in the vapor phase. The details can be found in the review by P. Gibart.[16] However, this process is not applicable to non-polar orientations, because the dislocations always bend to (0001) basal plane due to a free energy minimization, whereas this plane is parallel to the non-polar growth direction.[17]

1.3 Optical properties of III-Nitrides

1.3.1 Bandgap

All III-nitrides are direct-bandgap semiconductors, so they are suitable for fabricating photonic devices. At room temperature, the bandgaps of GaN and AlN are about ~ 3.4 eV and 6.2 eV, respectively.[1] For InN, it has been recently established that the bandgap is around 0.7 eV,[18] rather than the previously reported ~ 1.9 eV,[19] thanks to the improvement of material quality. A great potential advantage of the nitride system is that in theory it can cover an extraordinarily wide range of spectrum from ultra violet (UV) to infra-red (IR) using ternary alloys like $Al_xGa_{1-x}N$ and $In_xGa_{1-x}N$ with various Al or In fractions (x).

The band structure of III-nitrides has been investigated extensively. The representative features are presented in figure 1.7, where the band structure of GaN at T = 300 K is calculated based on the full-potential linearized augmented plane wave method within the local-density-functional approximation.[20] Note that the valence band is split into three excitonic sub-bands: heavy holes (usually referred to as A), light holes B, and split-off band C, with the crystal-field splitting and spin-orbit splitting taken into account.

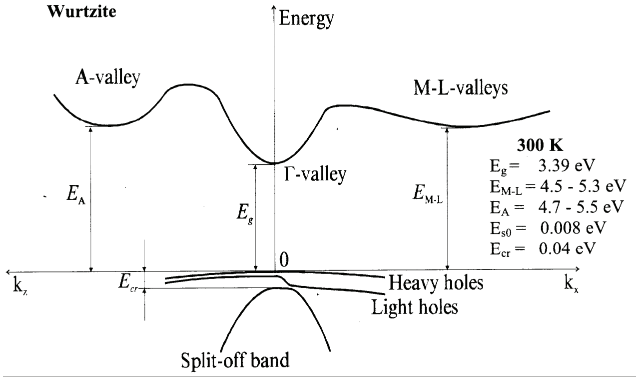

Figure 1.7 Calculated band structure of GaN near the Brillouin-zone (T = 300 K)

A practical issue for III-nitride bandgap is the influence of heteroepitaxy as the lattice mismatches among various alloys are not negligible. They induce biaxial strain, either compressive or tensile, which can be accommodated through the introduction of defects or elastic deformation of the lattice. The latter modifies the energy levels of the electronic band structure. The situation is quite complicated for wurtzite structures and is not within the scope of this thesis. In short, the bandgap increases when GaN is under compression and decreases under tensile stress. B. Gil *et al.*[21] have studied the dependence of the transition energies of A, B, and C excitons versus in-plane biaxial stress of *c*-plane GaN epilayers grown on *c*-plane sapphire (figure 1.8).

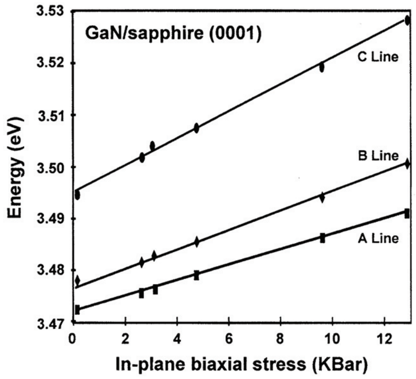

Figure 1.8 Dependence of the transition energies of A, B, and C excitons versus in-plane biaxial stress in *c*-plane GaN epilayers grown on *c*-plane sapphire. Dots are experimental data, after Ref. 21.

Another point worth mentioning is that the bandgap of semiconductors changes as a function of temperature, according to the empirical Varshni law[22]:

$$E_g(T) = E_g(0) - \frac{\alpha T^2}{T+\beta} \tag{1.1}$$

where *α* and *β* are empirical parameters, adjustable for various semiconductors. In the case of heteroepitaxy, the mismatch of TECs results in temperature dependence of stress in the epilayers. So the parameters have to be determined by a fit of the experimental data and *α*, *β* can be different from sample to sample. More information can be found in Ref. 1.

1.3.2 Refractive indices – linear birefringence

The refractive index for a certain medium is used to measure the propagation of light in that medium. If both the dispersion and absorption of light are taken into consideration, then it can be described by the complex refractive index:

$$\tilde{n} = n + i \cdot k \tag{1.2}$$

Here, n is the refractive index dispersion indicating the phase velocity, k is the extinction coefficient indicating the amount of absorption loss as real materials are not perfect insulators. Note that the notation plus in equation 1.2 corresponds to the time evolution of waves given by $e^{-i\omega t}$.

The refractive indices of $Al_xIn_yGa_{1-x-y}N$ ($0 \le x \le 1, 0 \le y \le 1, 0 \le x + y \le 1$) layers depend on factors such as wavelength, temperature, composition, and crystal orientation.[23, 24, 25, 26, 27] Especially, due to the anisotropy of the wurtzite structure, III-nitrides are natural optically-anisotropic uniaxial crystals, *i.e.* two independent nonzero matrix elements of the dielectric tensor – ε_o (ordinary) and ε_e (extraordinary), known as the dielectric constants – determine the propagation of linearly polarized light with electric field vector ***E*** perpendicular and parallel to *c*-axis, respectively. Both $\boldsymbol{E}\perp c$ and $\boldsymbol{E}//c$ configurations have been experimentally measured and theoretically calculated to verify the optical anisotropy in nitrides. Although the reported values vary primarily due to different growth conditions, it is consistently shown that there is a discrepancy between the ordinary ($n_o \perp c$) and the extraordinary ($n_e // c$) refractive indices. Indeed, GaN and AlN exhibit positive linear birefringence, *i.e.* $\Delta n = n_e - n_o > 0$. For example, according to Ciplys *et al.*,[26] n_o and n_e obtained from nominally undoped GaN epilayers at 632.8 nm wavelength were 2.351 ± 0.001 and 2.391 ± 0.001, respectively. A systematic study is presented in Ref. 27.

1.4 The effects of polarization fields – problem and solution

The anisotropy of wurtzite structure results in polarization-related properties:

(1) Spontaneous polarizations $\vec{P}_{sp}$

Due to the asymmetry along *c*-axis, the positive and negative charge centers do not coincide. This induces a bulk spontaneous polarization $\vec{P}_{sp}$ along *c*-axis in the equilibrium state, even without any external excitations (*e.g.* stress) – the so-called pyroelectric effects. As an intrinsic property, $\vec{P}_{sp}$ is determined by the material itself. The values of $\vec{P}_{sp}$ of III-nitrides calculated from *ab initio* theory are listed in table 1.3, where the sign minus means that spontaneous polarizations are always in $[000\bar{1}]$ direction. In fact, nitrides belong to the family of pyroelectric materials, distinguishing themselves from the conventional III-Vs.

Materials	GaN	AlN	InN
P_{sp} (C/m^2)	-0.034	-0.090	-0.042

Table 1.3 Calculated spontaneous polarizations for III-nitride binary compounds with *ab initio* theory (after F. Bernardini *et al.* [28])

(2) Piezoelectric polarization $\vec{P}_{pz}$

When crystals under an external strain undergo a deformation along a polar axis, there will be a modification of the whole polarization, known as the piezoelectric effect. For wurtzite III-nitrides, piezoelectric polarization $\vec{P}_{pz}$ along *c*-axis is induced by external deformation of the lattice constants (***a***, ***c***) as well as the change of internal displacement parameter ***u***. $\vec{P}_{pz}$ along *c*-axis is related to the strain $\vec{\varepsilon}$ in the film by the piezoelectric tensor. Due to the symmetry of the hexagonal unit cell, the relation can be simplified in Voigt notation as

$$P_{pz} = e_{33}\varepsilon_3 + e_{31}(\varepsilon_1 + \varepsilon_2) \tag{1.3}$$

Here, e_{31} and e_{33} are piezoelectric constants, out-of-plane strain $\varepsilon_3 = \frac{(c - c_0)}{c_0}$, and the in-plane strain $\varepsilon_1 = \varepsilon_2 = \frac{(a - a_0)}{a_0}$, where $\boldsymbol{c_0}$ and $\boldsymbol{a_0}$ are unstrained bulk lattice parameters reported in table 1.1, and ***c*** and ***a*** are the strained ones. The relation between ε_1 and ε_3 is

$$\varepsilon_3 = -2\frac{C_{13}}{C_{33}}\varepsilon_1 \tag{1.4}$$

C_{13} and C_{33} are the elastic stiffness constants of the crystals.

The values of those constants in equations 1.3 and 1.4 are reported in table 1.4.

	e_{31} (C/m^2)	e_{33} (C/m^2)	C_{13} (GPa)	C_{33} (GPa)
GaN	-0.37	0.67	68	354
AlN	-0.62	1.50	94	377
InN	-0.45	0.81	70	205

Table 1.4 piezoelectric constants e_{31}, e_{33} and elastic constants C_{13}, C_{33} for III-nitrides, after Ref. 28.

For III-nitride quantum heterostructures (*i.e.* one layer of small bandgap materials sandwiched between two layers of large bandgap materials) grown along *c*-axis, the total polarization $\vec{P}$ is a function of both spontaneous and piezoelectric components:

$$\vec{P} = \vec{P}_{sp} + \vec{P}_{pz} \tag{1.5}$$

Since $\vec{P}$ depends not only on the external stress but also on the material itself, its values in heterostructures are often discontinuous from layer to layer.

The electric displacement field $\vec{D}$ is defined as

$$\vec{D} = \varepsilon_0 \vec{E} + \vec{P} \tag{1.6}$$

Assuming the materials are undoped *i.e.* electrically-neutral, $\vec{D}$ is continuous throughout the heterostructure in the *c*-axis direction, and then the discontinuity of $\vec{P}$ gives rise to fixed space charges. The charges at the interface induce large built-in electric field $\vec{E}$ (usually in the scale of MV/cm). It leads to the quantum-confined Stark effect (QCSE),[29] as reported in heterostructures such as QWs (GaN/AlGaN[30] and InGaN/GaN[31]) and quantum dots (QDs)[32]. Actually, QCSE also occurs in conventional III-V systems like InGaAs/GaAs strained QWs grown along [111] direction, due to the piezoelectric field.[33] However, for III-nitrides, both strained[34] and unstrained[35] QWs are impacted by this effect, because its origin here is related to not only the piezoelectricity but also the spontaneous polarization. It is difficult to discriminate these two polarizations from an experimental point view.[36] That is why in some early work the QSCE was attributed to piezoelectric field alone.[34,37]

The impacts of QCSE in heterostructures can be easily explained in the case of a single QW (SQW). Assuming QCSE dominates over the confinement effects (in thin QWs with thickness ≤ 2 nm, the effect is relatively weak[38]), the polarization-induced electric field leads to a spatial separation – in other words, a reduced overlap – of the electron and hole wave functions, as illustrated in figure 1.9 (a).[39] It is responsible for the reduction of the interband oscillator strength, which is approximately proportional to the square of the overlap integral between electron and hole envelope wave functions.[37] The radiative recombination lifetime, which is approximately inversed to the oscillator strength, also increases due to the reduced overlap, enhancing the probability of nonradiative recombinations. Besides, it leads to the red-shift of the QW transition energy, which enlarges with the increase of the well thicknesses.[38, 40] For complex structures, the situation is slightly different. For example, in the case of multiple QWs (MQWs), the electric field reduces when the barrier thickness decreases. It may lead to a blueshift of the QW transition energy.[38] For wurtzite QDs grown by the Stranski-Krastanov mode, the analytical study on the electric field, considering the geometry of the dots, are available in the paper of D. P. Williams *et al.*[41] A comprehensive review of the polarization effects in optoelectronic quantum structures can be found in the literature by R. Butté and N. Grandjean.[42]

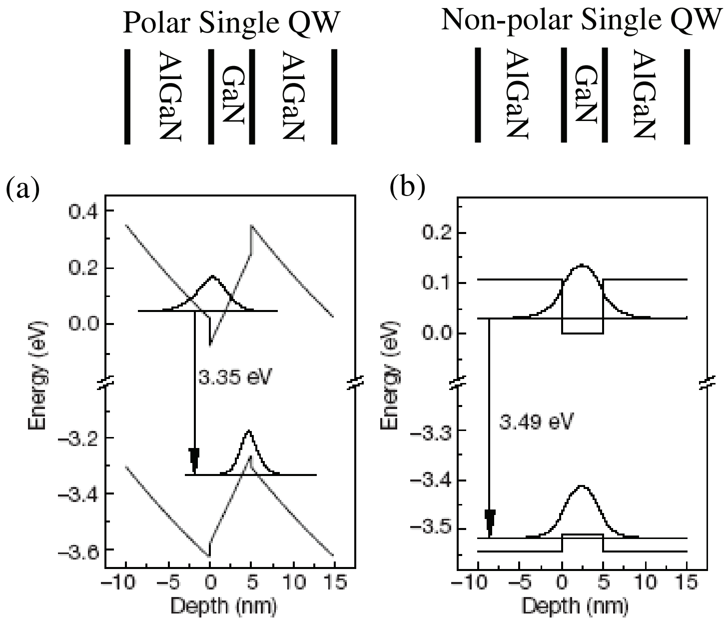

Figure 1.9 Calcualted band profiles and electron and hole envelope wave functions in GaN (5 nm)/$Al_{0.1}Ga_{0.9}N$ (10nm) QWs grown on (a) polar *c*-plane and (b) non-polar planes, after Ref. 39.

Although polarization is an advantage for two-dimensional electron gas formation in the application of electronic devices like transistors,[43] it does decrease the radiative efficiency of photonic devices grown on *c*-plane. Particularly, this problem limits the performance of GaN-based blue light emitters.[44] Also, it is responsible for the reduced efficiency of longer wavelength (green) InGaN/GaN LEDs, due to higher InN fraction and consequently larger polarization fields. This issue can be entirely eliminated by growing photonic devices on non-polar orientations *i.e.* $\{11\bar{2}0\}$ *a*-plane and $\{10\bar{1}0\}$ *m*-plane, where the polar *c*-axis is parallel to the plane. The heterostructures grown on non-polar planes have flat-band profile without spatial separation of wave functions, as depicted schematically in figure 1.9 (b).

1.5 Structural properties of sapphire

Recently, high-quality non-polar (*a*- and *m*-plane) GaN free-standing templates have been obtained by slicing from thick *c*-plane bulk GaN crystals grown by HVPE.[45] Good performance non-polar LEDs and LDs have been demonstrated on such templates.[46, 47] However, this kind of templates are not cost-effective and the size is usually small (~ 1 cm^2), so for the time being they are not yet suitable for commercial mass production. Thus, heteroepitaxy of non-polar GaN layers on foreign substrates is a quite interesting alternative. Among numerous substrates for GaN epitaxy such as SiC, Si, ZnO, and $LiAlO_2$, sapphire is the most-widely used. Also, it is the only substrate employed in this thesis. Thus, basic knowledge of sapphire is essential to understand GaN heteroepitaxy.

Sapphire (single crystal aluminum oxide α-Al_2O_3) can be described by either a rhombohedral or a larger hexagonal unit cell.[48] It has the space group of $R\bar{3}c$ (Hermann-Mauguin notation)

or D_{3d}^{6} (Schoenflies notation). For the hexagonal unit cell containing 12 Al and 18 O atoms, its lattice constants are a_0 = 4.759 Å and c_0= 12.991 Å (T = 300 K).
Its TECs (× 10^{-6} K^{-1}) along *a*- and *c*-axis are 7.3 and 8.5, respectively, larger than those of GaN (*a* 5.59, *c* 3.17) in both directions.[3] Assuming that the GaN epilayers (above a certain critical thickness) grown on sapphire substrates are fully-relaxed during high temperature (HT) growth at T ~ 1000 °C, they are then expected to be under compressive strain after cooling down to the room temperature (T ~ 20 °C). From a growth perspective, this is a technical advantage for sapphire compared to other substrates like 6H–SiC and Si, whose TECs (× 10^{-6} K^{-1}) (6H–SiC: //*a* 4.46, //*c* 4.16; Si 3.59) are smaller than those of GaN, often leading to tensile strain in GaN epilayers and sometimes inducing cracking during the post-growth cooling. Besides, sapphire substrates are cost-effective and commercially available in large scales (diameters of 2 – 6 inches).

Four sapphire orientations are commonly used for GaN epitaxy: (0001) *c*-, $(11\bar{2}0)$ *a*-, $(10\bar{1}0)$ *m*-, and $(1\bar{1}02)$ *r*-planes, as depicted in figure 1.10. Among them, sapphire *c*- and *a*-planes are overwhelmingly used for polar *c*-plane GaN, so they are not introduced here. Instead, this thesis focuses on the other two (*r*- and *m*-planes).

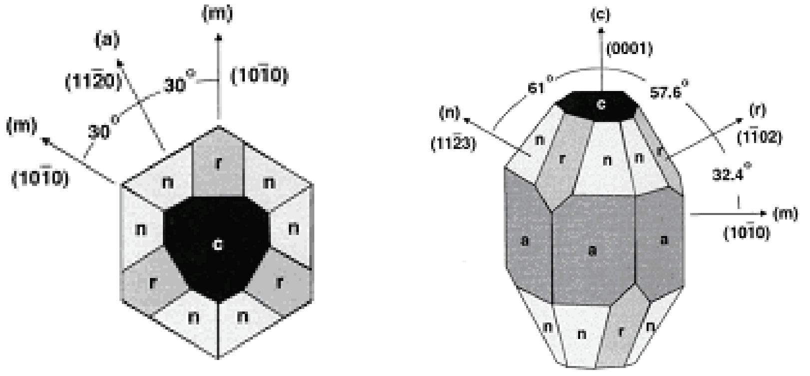

(a) (b)

Figure 1.10 Rhombohedral structure and various crystal planes of sapphire: (a) top view and (b) side view of *c*-plane, after Ref. 3.

R-plane sapphire has been used for epitaxy of *a*-plane GaN ever since 1970s.[49, 50] Its unit cell is defined as 4.759 × 5.128 Å^2, where 5.128 Å is the unit length for $(1\bar{1}01)$. Its structure is schematically shown in figure 1.11, where the atoms are organized in a repeating unit called the "surface building block" consisting of (O-Al-O-Al-O) layers along $[1\bar{1}02]$ direction.[51] Note that there are two types of bonds classified as the length between atoms: long (1.97 Å) and short (1.86 Å) Al-O bonds. The calculated cleavage surface energy is minimum when the crystal is cleaved at the boundary of the "surface building block".[51] The thickness of this block is about 2.6 Å.

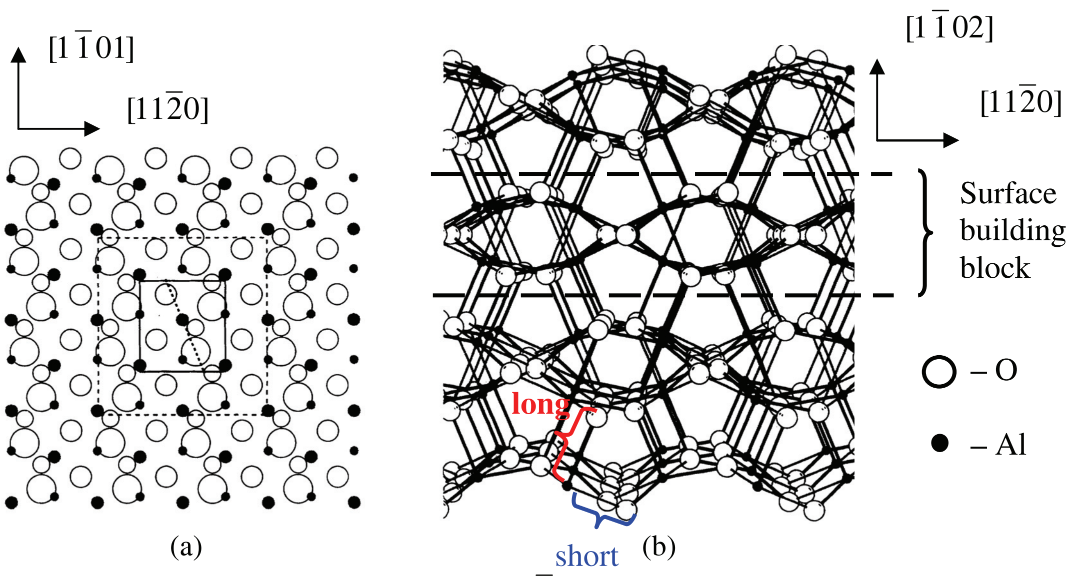

Figure 1.11 Ball-stick model of sapphire ($1\bar{1}02$) surface: (a) top view of one "surface building block" made up of five atomic layers (O-Al-O-Al-O), and (b) side view along [$1\bar{1}01$] direction, where the long (red) and short (blue) Al-O bonds are marked. Dash lines in (b) indicate the boundaries of the "surface building block", after Ref. 51.

The structure of *m*-plane sapphire is schematically presented in figure 1.12. There are both Al and O atoms at the surface. Within a unit cell (12.991 × 4.759 Å^2), the numbers of Al and O are equal (= 4) at the surface, producing a neutral charge density.

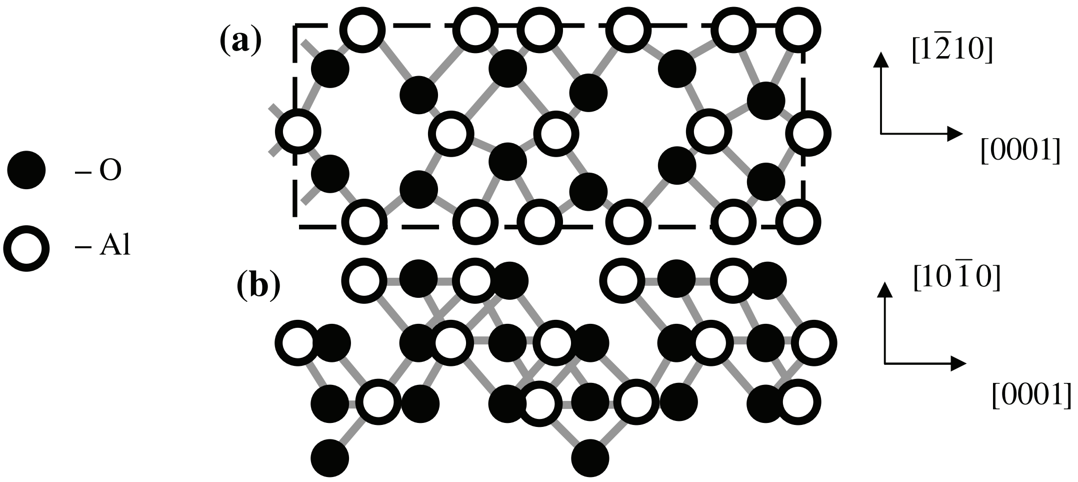

Figure 1.12 Ball-stick model of sapphire ($10\bar{1}0$) surface: (a) top view and (b) side view along [$1\bar{2}10$] direction. Dash line in (a) indicates the unit cell of sapphire.

Note that the sapphire surfaces described above are ideal, *i.e.* free from relaxation and reconstruction. In reality, however, as-received sapphire wafers are always chemically – mechanically polished and are exposed to air for some time, so the surface is likely to be modified (*e.g.* oxidized).

1.6 Summary

This chapter reviews some basic properties of III-nitrides and sapphire:

- Two polarities in GaN {0001} directions: Ga- and N-, due to the lack of symmetry.
- Common defects are dislocations and stacking faults. ELO helps to reduce defects density in the mask areas.
- In-plane strain and temperature impact the nitrides bandgap.
- Linear birefringence effect for the refractive indices.
- Spontaneous and piezoelectric polarization fields along the *c*-axis, which lead to QCSE in quantum heterostructures grown on *c*-plane. This problem can be overcome by growing heterostructures on non-polar planes.
- *R*- and *m*-plane sapphire wafers are used as substrates for the heteroepitaxy of *a*- and *m*-plane GaN layers, respectively.

Bibliography

---

[1] I. Vurgaftman and J. R. Meyer, "Band parameters for nitrogen-containing semiconductors", *Journal of Applied Physics*, vol. 94, no. 6, pp. 3675-3696, 2003

[2] F. Bernardini, V. Fiorentini, and D. Vanderbilt, "Spontaneous polarization and piezoelectric constants of III-V nitrides", *Physical Review B*, vol. 56, no. 16, pp. R10024 – R10027, 1997

[3] O. Ambacher, "Growth and applications of group III-nitrides", *Journal of Physics D: Applied Physics*, vol. 31, no. 20, pp. 2653-2710, 1998

[4] J. E. Northrup, and J. Neugebauer, "Theory of GaN $(10\bar{1}0)$ and $(11\bar{2}0)$ surfaces", *Physical Review B*, vol. 53, no. 16, pp. R10477 – R10480, 1996

[5] D. Segev and C. G. Van de Walle, "Electronic structure of nitride surfaces", *Journal of Crystal Growth*, vol. 300, no. 1, pp. 199-203, 2007

[6] C. Stampfl and C. G. Van de Walle, "Energetics and electronic structure of stacking faults in AlN, GaN, and InN", *Physical Review B*, vol. 57, no. 24, pp. R15052-15055, 1998.

[7] G. Salviati, M. Albrecht, C. Zanotti-Fregonara, N. Armani, M. Mayer, Y. Shreter, M. Guzzi, Yu. V. Melnik, K. Vassilev Ski, V. A. Dmitriev, and H. P. Strunk, "Cathodoluminescence and transmission electron microscopy study of the influence of crystal defects on optical transitions in GaN", *phys. stat. sol. (a)*, vol. 171, no. 325, pp. 325-339, 1999.

[8] D. Hull and D. J. Bacon, *Introduction to Dislocations*, fourth edition, Elsevier, 2001.

[9] M. A. Moram, C. F. Johnson, J. L. Hollander, M. J. Kappers, and C. J. Humphreys, "Understanding x-ray diffraction of nonpolar gallium nitride films", *Journal of Applied Physics*, vol. 105, no. 11, pp. 113501, 2009.

[10] R. Kröger, "Defects and interfacial structure of *a*-plane GaN on *r*-plane sapphire", *Nitrides with nonpolar surfaces*, Edited by T. Paskova, Wiley-VCH, 2008.

[11] D. Cherns and M. E. Hawkridge, "The structural and properties of dislocations in GaN", Journal of Materials Science, vol. 41, no. 9, pp. 2685-2690, 2006.

---

[12] L. Jastrzebski, “SOI by CVD: epitaxial lateral overgrowth (ELO) process-Review”, *Journal of Crystal Growth*, vol. 63, no. 3, pp. 493-526, 1983.

[13] J.-O. Carlsson, “Selective vapor-phase deposition on patterned substrates”, *Critical Reviews in Solid State and Materials Sciences*, vol. 16, no. 3, pp. 161-212, 1990.

[14] B. Beaumont, P. Vennégues, and P. Gibart, “Epitaxial lateral overgrowth of GaN”, *phys. stat. sol. (b)*, vol. 227, no.1, pp. 1-43, 2001.

[15] S. Haffouz, B. Beaumont, and P. Gibart, “Effect of magnesium and silicon on the lateral overgrowth of GaN patterned substrates by metal organic vapor phase epitaxy”, *MRS Internet Journal of Nitride Semiconductor Research*, vol. 3, pp. 20, 1998.

[16] P. Gibart, “Metal organic vapor phase epitaxy of GaN and lateral overgrowth”, *Reports on Progress in Physics*, vol. 67, no. 5, pp. 667-715, 2004.

[17] K. W. Schwarz, “Simulation of dislocations on the mesoscopic scale. I. methods and examples”, *Journal of Applied Physics*, vol. 85, no. 1, pp. 108-119, 1999.

[18] J. Wu, W. Walukiewicz, K. M. Yu, J. W. Ager III, E. E. Haller, H. Lu, W. J. Schaff, Y. Saito, Y. Nanishi, “Unusual properties of the fundamental band gap of InN”, *Applied Physics Letters*, vol. 80, no. 21, pp.3967-3969, 1993.

[19] K. Osamura, K. Nakajima, Y. Murakami, P. H. Shingu, and A. Ohtsuki, “Fundamental absorption edge in GaN, InN and their alloys”, *Solid State Communications*, vol. 11, no. 5, pp. 617-621, 1972.

[20] M. Suzuki, T. Uenoyama, and A. Yanase, “First-principles calculations of effective-mass parameters of AlN and GaN”, *Physical Review B*, vol. 52, no. 11, pp. 8132-8139, 1995.

[21] B. Gil, O. Briot, and R. –L. Aulombard, “Valence-band physics and the optical properties of GaN epilayers grown onto sapphire with wurtzite symmetry”, *Physical Review B*, vol. 52, pp. R17028-17031, 1995.

[22] V. P. Varshni, “Temperature dependence of the energy gap in semiconductors”, Physica, vol. 34, pp.149-154, 1967.

[23] Ümit Özgür, Grady Webb-Wood, Henry O. Everitt, F. Yun, and H. Morkoç, “Systematic measurement of $Al_xGa_{1-x}N$ refractive indices”, *Applied Physics Letters*, vol. 79, no. 25, pp. 4103-4105, 2001.

[24] U. Tisch, B. Meyler, O. Katz, E. Finkman, and J. Salzman, “Dependence of the refractive index of $Al_xGa_{1-x}N$ on temperature and composition at elevated temperatures”, *Journal of Applied Physics*, vol. 89, no. 5, pp. 2676-2685, 2001.

[25] M. J. Bergmann, Ü. Özgür, H. C. Casey Jr., H. O. Everitt, J. F. Muth, “Ordinary and extraordinary refractive indices for $Al_xGa_{1-x}N$ epitaxial layers”, *Applied Physics Letters*, vol. 75, no. 1, pp. 67-69, 1999.

[26] D. Ciplys, R. Gaska, M. S. Shur, R. Rimeika, J. W. Yang and M. Asif Khan, “Propagation of guided optical waves in thick GaN layers grown on (0001) sapphire”, *Applied Physics Letters*, vol. 76, no. 16, pp. 2232-2234, 2000.

---

[27] V. I. Gavrilenko, and R. Q. Wu, “Linear and nonlinear optical properties of group-III nitrides”, *Physical Review B*, vol. 61, no. 4, pp. 2632-3642, 2000.

[28] F. Bernardini, V. Fiorentini, and D. Vanderbilt, “Accurate calculation of polarization-related quantities in semiconductors”, *Physical Review B*, vol. 63, no. 19, pp. 193201, 2001.

[29] D. A. B. Miller, D. S. Chemla, T. C. Damen, A. C. Gossard, W. Wiegmann, T. H. Wood, and C. A. Burrus, “Band-edge electroabsorption in Quantum well structures: the quantum-confined Stark effect”, *Physical Review Letters*, vol. 53, no. 22, pp.2173-2176, 1984.

[30] T. Deguchi, K. Sekiguchi, A. Nakamura, T. Sota, R. Matsuo, S. Chichibu, and S. Nakamura, “Quantum-confined Stark effect in an AlGaN/GaN/AlGaN single quantum well structure”, *Japanese Journal of Applied Physics*, vol. 38, part 2, no. 8B, pp. L914- L916, 1999.

[31] T. Takeuchi, C. Wetzel, S. Yamaguchi, H. Sakai, H. Amano, and I. Akasaki, “Determination of piezoelectric fields in strained GaInN quantum wells using the quantum-confined Stark effect”, *Applied Physics Letters*, vol. 73, no. 12, pp. 1691-1693, 1998.

[32] F. Widmann, J. Simon, B. Daudin, G. Feuillet, J. L. Rouvière, N. Pelekanos, and G. Fishman, “Blue-light emission from GaN self-assembled quantum dots due to giant piezoelectric effect”, *Physical Review B*, vol. 58, no. 24, pp. R15989-R15992, 1998.

[33] R. L. Tober, and T. B. Bahder, “Determining the electric field in [111] strained-layer quantum wells”, *Applied Physics Letters*, vol. 63, no. 17, pp.2369-2371, 1993.

[34] T. Takeuchi, S. Sota, M. Katsuragawa, M. Komori, H. Takeuchi, H. Amano, and I. Akasaki, “Quantum-confined Stark effect due to piezoelectric fields in GaInN strained quantum wells”, *Japanese Journal of Applied Physics*, vol. 36, part 2, no. 4A, pp.L382-L385, 1997.

[35] R. Langer, J. Simon, V. Ortiz, N. T. Pelekanos, A. Barski, R. André, and M. Godlewski, “ Giant electric fields in unstrained GaN single quantum wells”, *Applied Physics Letters*, vol. 74, no. 25, pp.3827-3829, 1999.

[36] M. Leroux, N. Grandjean, M. Laügt, J. Massies, B. Gil, P. Lefebvre, and P. Bigenwald, , “Quantum confined Stark effect due to built-in internal polarization fields in (Al, Ga)N/GaN quantum wells”, *Physical Review B*, vol. 58, no. 20, pp. R13371, 1998.

[37] J. S. Im, H. Kollmer, J. Off, A. Sohmer, F. Scholz, and A. Hangleiter, “Reduction of oscillator strength due to piezoelectric fields in GaN/$Al_xGa_{1-x}N$ quantum wells”, *Physical Review B*, vol. 57, no. 16, pp. 9435-9438, 1998.

[38] N. Grandjean, B. Damilano, S. Dalmasso, M. Leroux, M. Laügt, and J. Massies, “Built-in electri-field effects in wurtzite AlGaN/GaN quantum wells”, *Journal of Applied Physics*, vol. 86, no. 7, pp. 3714-3720, 1999.

[39] P. Waltereit, O. Brandt, A. Trampert, H. T. Grahn, J. Menniger, M. Ramsteiner, M. Reiche, and K. H. Ploog, “Nitride semiconductors free of electrostatic fields for efficient white light-emitting diodes”, *Nature*, vol. 406, pp. 865-868, 2000.

[40] E. Berkowicz, D. Gershoni, G. Bahir, E. Lakin, D. Shilo, E. Zolotoyabko, A. C. Abare, S. P. Denbarrs, and L. A. Coldren, “Measured and calculated raidative lifetime and optical absorption of $In_xGa_{1-x}N$/GaN quantum structures”, *Physical Review B*, vol. 61, no. 16, pp. 10994-11008, 1999.

---

[41] D.P. Williams, A. D. Andreev, and E. P. O'Reilly, "Dependence of exciton energy on dot size in GaN/AlN quantum dots", *Physical Review B*, vol. 73, pp. 241301(R), 2006.

[42] R. Butté and N. Grandjean, "Effects of polarizations in optoelectronic quantum structures", *Polarization Effects in Semiconductors*, Edited by C. Wood and D. Jena, Springer 2008.

[43] O. Ambacher, J. Smart, J.R. Shealy, N.G. Weimann, K. Chu, M. Murphy, W.J. Schaff, L.F. Eastman, R. Dimitrov, L. Wittmer, M. Stutzmann, W. Rieger, and J. Hilsenbeck, "Two-dimensional electron gases induced by spontaneous and piezoelectric polarization charges in N- and Ga-face AlGaN/GaN heterostructures", *Journal of Applied Physics*, vol. 85, no. 6, pp. 3222-3233, 1999.

[44] H. Masui, J. Sonoda, N. Pfaff, I. Koslow, S. Nakamura, and S. P. DenBaars, "Quantum-confined Stark effect on photoluminescence and electroluminescence characteristics of InGaN-based light-emitting diodes", *Journal of Physics D: Applied Physics*, vol. 41, no. 16, pp. 165105, 2008.

[45] T. Paskova, R. Kroeger, D. Hommel, P. P. Paskov, B. Monemar, E. Preble, A. Hanser, N. M. Williams, and M. Tutor, "Nonpolar a- and m-plane bulk GaN sliced from boules: structural and optical characteristics", *phys. stat. sol. (c)*, vol. 4, no. 7, pp. 2536-2539, 2007.

[46] K. Iso, H. Yamada, H. Hirasawa, N. Fellows, M. Saito, K. Fujito, S. P. DenBaars, J. S. Speck, and S. Nakamura, "High brightness blue InGaN/GaN light emitting diode on nonpolar *m*-plane bulk GaN substrate", *Japanese Journal of Applied Physics*, vol. 46, no. 40, pp.L960-L962, 2007.

[47] K. Okamoto, H. Ohta, S. F. Chichibu, J. Ichihara, and H. Takasu, "Continuous-wave operation of m-plane InGaN multiple quantum well laser diodes", *Japanese Journal of Applied Physics*, vol. 46, no. 9, pp.L187-L189, 2007.

[48] W. E. Lee, and K. P. D. Lagerlof, "Structural and electron diffraction data for sapphire (α-Al_2O_3)", *Journal of Electron Microscopy Technique*, vol. 2, no. 3, pp. 247-258, 1985.

[49] H. P. Maruska, L. J. Anderson, and D. A. Stevenson, "Microstructural observations on gallium nitride light-emitting diodes", *J. Electronchem. Soc.: solid-state science and technology*, vol. 121, no. 9, pp. 1202-1207, 1974.

[50] M. Sano, and M. Aoki, "Epitaxial growth of undoped and Mg-doped GaN", *Japanese Journal of Applied Physics*, vol. 15, no. 10, pp. 1943-1950, 1976.

[51] J. Guo, D. E. Ellis, and D. J. Lam, "Electronic structure and energetics of sapphire (0001) and $(1\bar{1}02)$ surfaces", *Physical Review B*, vol. 45, no. 23, pp. 13647-13656, 1992.

2. Experimental Methods

This thesis is mainly about experimental studies. So it is worthwhile to explain the principles and practices of the experimental methods employed before rushing to the results. The methods are organized in two categories: epitaxial growth and characterization.

2.1 Epitaxy techniques

Two techniques that have been used all along this thesis are hydride vapor phase epitaxy (HVPE) and molecular beam epitaxy (MBE). HVPE was used for (a) the heteroepitaxy of *a*- and *m*-plane GaN epilayers on *r*- and *m*-plane sapphire, respectively, and (b) the growth of GaN epitaxial lateral overgrowth (ELO) layers on pattered templates. MBE was utilized for (a) preliminary study of GaN epitaxy on HVPE templates and (b) the deposition of (Al)GaN-based heterostructures like quantum wells (QWs) and AlN/GaN distributed Bragg reflectors (DBRs).

2.1.1 Hydride vapor phase epitaxy

HVPE is a conventional technique to produce III-V compound semiconductors, where the group-III gas sources (*e.g.* GaCl) are *in situ* synthesized by flowing HCl over liquid metals (Ga). That is why HVPE is also referred to as *halide* vapor phase epitaxy. As mentioned in *Introduction*, the first single crystal film of GaN was actually grown by HVPE on sapphire substrate in 1969.[1] Unfortunately, the material quality reported in the early work was quite poor. Nowadays, MOVPE is the leading technique for nitride epitaxy, since it can achieve high-quality QWs and high *p*-doping concentration. Even so, HVPE is still playing an important role thanks to its technical advantages:

First, its high growth rate (usually in the scale of $10 – 10^2$ μm per hour for GaN) is widely recognized, compared to MOVPE and MBE (1 – 4 μm per hour for GaN). It is often used to grow thick quasi-bulk crystal on low-dislocation-density templates prepared by ELO or high N_2 pressure solution growth[2]. HVPE free-standing GaN templates (defects density $10^5 – 10^6$ cm^{-2}) are now available.
Secondly, HVPE is also suitable for the heteroepitaxy of planar GaN layers on foreign substrates. For example, it was demonstrated in our laboratory that thin, high-quality *c*-plane GaN epilayers can be grown directly on sapphire substrates, using a conventional two-step growth procedure similar to that of MOVPE.[3]

Third, HVPE has a relatively simple configuration and the maintenance is cost- effective. Besides, the process gasses are readily available and inexpensive.

All these factors are improving the competitiveness of HVPE as a mass production platform, and more and more resources and efforts are being delivered towards its commercial applications in the manufacturing industry of solid-state lighting.[4]

Growth reactions for GaN

HVPE is a chemical process. To form GaN, GaCl and NH_3 serve as group-III and -V sources, respectively. Accordingly, there are two source reactions that supply the reactants. The Ga source is formed *in situ* through the conversion of Ga metal into GaCl:

$$xGa_{(l)} + HCl_{(g)} \rightarrow xGaCl_{(g)} + (1-x)HCl_{(g)} + \frac{x}{2}H_{2(g)} \qquad (2.1)$$

where x is the conversion efficiency. The temperature of this reaction is usually set at 800 – 950 °C in our experiment setup. Although the equilibrium conversion efficiency at such temperature is essentially unity, the exact conversion percentage depends on factors such as the residence time of HCl gas flow over liquid Ga source and Ga surface area.[5] In practice, x is impacted by two parameters: the temperature of the source zone and the HCl flow rate. Empirical data show that x increases with the increase of temperature and with the decrease of the flow rate.[6] The conversion efficiency in our experiments is assumed to be near unity. Besides, the synthesized GaCl molecules tend to condense on the walls of the reactor if they are cold, due to the low vapor pressure of the metal chlorides at room temperature. To avoid that, the reactor walls are always kept at high temperature during the experiments, so HVPE is called "hot-wall" reactor, in comparison to the "cold-wall" MOVPE reactor.
The other reaction is the decomposition of NH_3:

$$NH_{3(g)} \rightarrow (1-y)NH_{3(g)} + \frac{y}{2}N_{2(g)} + \frac{3}{2}yH_{2(g)} \qquad (2.2)$$

where y is the degree of dissociation, influenced mainly by the temperature, the partial pressure, and the residence time in the reaction zone.[5] Although thermodynamics predict that NH_3 can be completely decomposed into H_2 and N_2 at temperature as low as 200 °C, the decomposition rate is actually limited to only a few percents at temperature ≥ 800 °C due to a high kinetic barrier.[7] On one hand, such high kinetic barrier enables the effective transportation of reactive group-V source (NH_3) to the substrate, where the crystal growth occurs. On the other hand, since the low decomposition rate is also applicable to the surface of the substrate (either sapphire[8] or GaN[9]), the growth is usually under high V/III ratio (~ 100 in our HVPE system).

In analogy to GaAs, the process of GaN HVPE growth can be postulated as being governed by two thermodynamically feasible reactions[7]:

$$GaCl_{(g)} + NH_{3(g)} \rightarrow GaN_{(s)} + HCl_{(g)} + H_{2(g)} \qquad (2.3)$$

$$3GaCl_{(g)} + 2NH_{3(g)} \rightarrow 2GaN_{(s)} + GaCl_{3(g)} + 3H_{2(g)} \qquad (2.4)$$

However, the situation gets much more complicated when facing the reality. For example, the species involved (GaCl, NH_3, HCl, and H_2) are quite reactive at the growth temperature (T ~ 1000°C). In addition, GaN itself is thermally-unstable at T ~ 1000 °C and tends to decompose into Ga and N_2 well before reaching the melting point (≥ 2000 °C).

There have been intensive studies around simulations of GaN HVPE growth, mainly for the polar {0001} c-plane. The simulations include both the thermodynamics and kinetics.[10, 11, 12, 13, 14] Unfortunately, the accuracy of such models is largely weakened by the arbitrary assumptions on factors such as the reactor geometry, the streamlines of the various gas species within the chamber, and parasitic depositions. Note that *ab initio* calculations of GaN surface based on density function theory have been adopted to improve the simulations.[15, 16, [17, 18, 19] Even so, simulations of HVPE growth are still far from satisfactory, whereas empirical experience based on experimental investigation is the main source of knowledge.

HVPE equipment

The HVPE system in our laboratory, installed in 1997, is a prototype from Aixtron. It is a hot-wall, computer-controlled, horizontal quartz reactor (figure 2.1). The main quartz tube is of 15 cm in diameter and 1.2 m in length. The reactor is heated externally *via* five furnace zones (yellow), where no. 2 and 4 are the source and deposition zones, respectively. The temperature can reach at maximum about 1090 °C. On the right side is the entry of the reactor chamber for loading/unloading samples. It is connected to a pumping system that serves to control the growth pressure and to purge the reactor after loading the sample. The pressure of the chamber can be reduced to ~ 50 mbar. The substrate holder is a 3-inch (in diameter) rotating quartz disk using the gas foil rotation technique, where a single 2-inch wafer can be loaded in the center. The temperature of the substrate holder is detected by a thermocouple located beneath the holder (not shown here). There is a laser reflectometry (LR) unit installed right on top of the deposition zone, where the light probes near-normally to the center of the substrate holder. It is employed to *in situ* measure the growth process. The details of this LR setup will be introduced later.

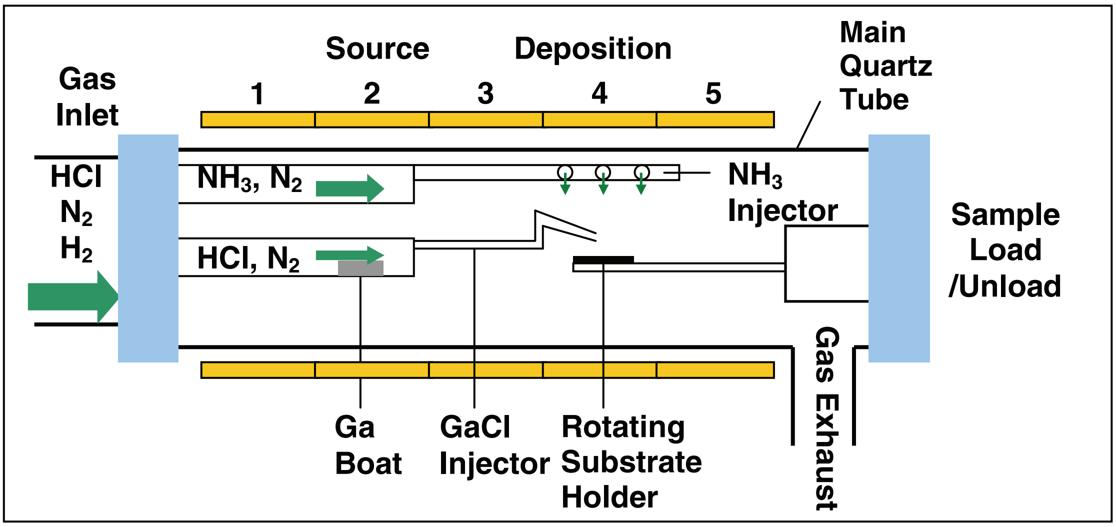

Figure 2.1 A schematic diagram (side view) of the HVPE reactor at our laboratory

On the left side is the gas inlet, where all the gas species involved in the growth are introduced *via* different source tubes. NH_3, the group-V source, is provided through two parallel injectors using holes as gas outlet. The group-III source GaCl, *in situ* synthesized through HCl flowing over the boat containing the liquid gallium (equation 2.1), is supplied through a specially-designed injector equipped with a nozzle at the outlet. H_2 and additional HCl (as etchant during cleaning) are provided through the main tube. N_2, the carrier gas, is provided through all the tubes. In our HVPE setup, the current tube configuration of group-III and -V sources have been adjusted in terms of the flow dynamics so as to mix the source gas (NH_3 and GaCl) close to the substrate holder where the growth reaction takes place, reducing the detrimental effects from source gases pre-reaction[10] and parasitic deposition[20] [figure 2.2 (a)]. As a result, the pre-reaction is largely prevented, and the parasitic deposition is limited on the substrate holder and the supporting rod nearby [figure 2.2 (b)]. The parasitic deposits of polycrystalline GaN are routinely removed by an etch run of the reaction chamber, consisting of HCl and H_2 gases at T ~ 1050°C.

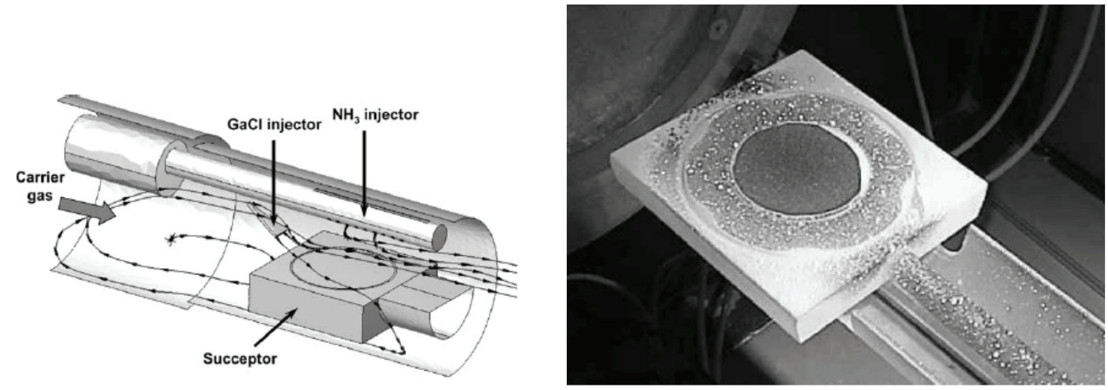

Figure 2.2 (a) Simulations of the gas streamlines in our HVPE reactor under the standard growth conditions, where only one NH_3 injector is visible. (b) Parasitic deposits on the substrate holder and supporting rod after the deposition of a thick ($d \geq 200$ μm) GaN layer, after Ref. 13.

2.1.2 NH_3 source molecular beam epitaxy

MBE is essentially a refined form of ultrahigh vacuum (UHV) evaporation: under UHV conditions, molecular beams of atoms or molecules are condensed onto a heated single crystal substrate where they react chemically, forming a crystalline layer.[21] MBE was invented in the late 1960s by Alfred Y. Cho and his colleagues at Bell Laboratories, USA. Authoritative reviews describing some critical turning points of the MBE development can be found in the literature of A. Y. Cho[22] and J. R. Arthur[23]. Although it was first applied to the growth of compound semiconductors, MBE can actually grow thin epitaxial films of a wide variety of materials, ranging from metals to semiconductors to insulators. Thanks to its UHV environment, MBE has the unique advantage of being compatible with a wide range of *in situ* surface analysis techniques so as to monitor surface structures and chemical compositions, *e.g.* reflection high-energy electron diffraction (RHEED)[24], scanning tunneling microscopy (STM)[25], secondary ion mass spectroscopy (SIMS)[26], quadrupole mass spectrometry (QMS)[27], and Auger electron spectrometry (AES)[28]. These analysis capabilities are crucial to control and to characterize in real time the epitaxial growth (*e.g.* layer thickness and composition) down to the atomic scale since it provides an instantaneous feedback on the influence of growth conditions. Besides, the growth rate employed is quite low, about 0.1–1 monolayer per second. Thus, MBE proves to be a very powerful tool to grow nanostructures of complex design with high accuracy and reproducibility.

Compared to MOVPE, the development of MBE as a growth technique for III-V nitrides is relatively slow, hindered mainly by the lack of an efficient source of atomic nitrogen and consequently the poorer material quality (especially for InGaN). Different nitrogen sources such as NH_3[9], dimethylhydrazine (DMHy)[29], reactive species of N_2 from electron cyclotron resonance (ECR) or radio-frequency (RF) plasmas[30], and non-plasma N_2 ions from Kaufman ion source[31] have been studied. Although each source has pros and cons, it seems that NH_3 stands out as a competitive candidate, as high-quality GaN epilayers using NH_3 source MBE have been reported with growth rate comparable to that of MOVPE.[32] In addition, for NH_3 source MBE, successful investigations on some fundamental issues, such as nitridation effects on sapphire surface[33], epitaxial relationship[34], and RHEED monitoring[35], have laid the foundation for further advancement. That is why NH_3 source is adopted for non-polar nitrides epitaxy in this thesis.

MBE equipment

The MBE installed in our laboratory is a Riber Compact 21 system, which consists of three chambers: growth (left), loading (center), and preparation (right), as outlined by dash-line squares in figure 2.3. Here is the standard operation process: first, the sample is loaded into the loading chamber, which connects to the growth and preparation chambers *via* gate valves. Then, it is transferred right to the preparation chamber *via* the transfer arm to be outgassed at T ~ 450 °C for ~ 1 hour, in order to release the absorbed species. After that, it is transferred left to the growth chamber, where the epitaxial growth takes place. The three chambers should always be under UHV condition during operations. The system is operated through PC-based software which controls all parameters such as temperature, pressure, and gas flux.

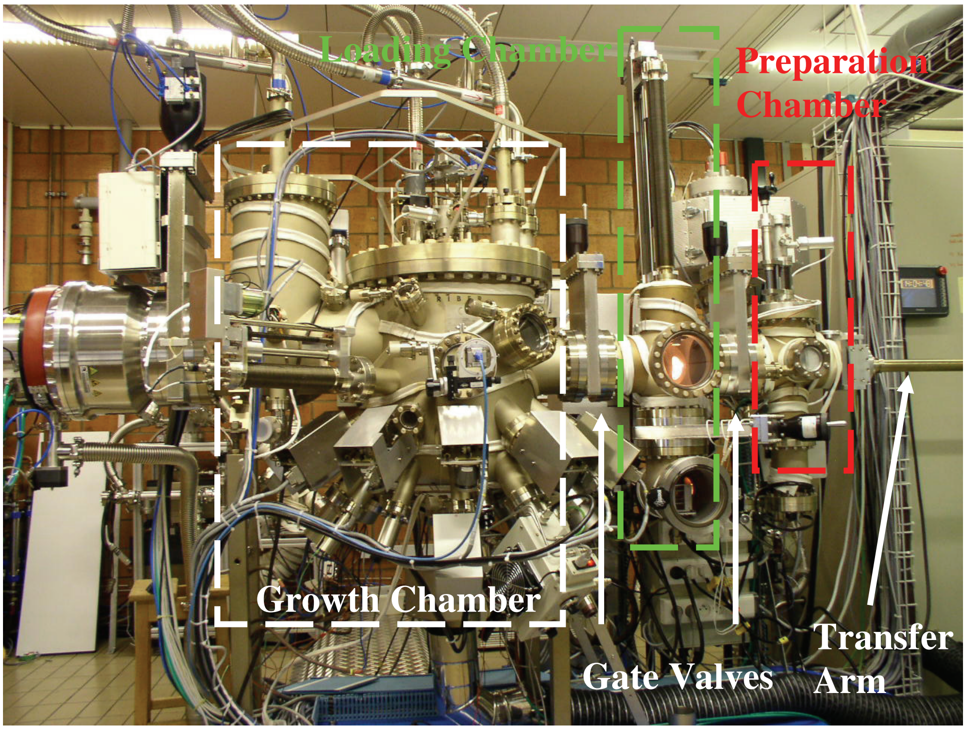

Figure 2.3 Side view of Riber compact 21 MBE system at our laboratory. The dash squares mark the configurations of the growth (white), loading (green), and preparation (red) chambers, respectively. The arrows indicate the positions of transfer arm and grate valves.

The growth chamber is schematically presented in figure 2.4. High-purity metals (Ga, Al, and In) are used as group-III sources, ammonia gas as the nitrogen precursor, and solid Si and Mg as *n*- and *p*-type dopants, respectively. All solid sources are stored in the effusion cells, where the flux can be controlled by tuning the temperatures of the cells. The effusion cells are capped by the shutters. The sample is laid upside-down in the center of the substrate holder, which allows continuous rotation during growth in order to improve the uniformity. A heater located right above the substrate holder heats the sample from the back. The growth temperature is monitored by a pyrometer. The main shutter beneath the substrate can block all incoming species whenever necessary. The whole surrounding of the chamber is cooled by cryopanels using liquid N_2. The growth process is *in situ* monitored by two apparatus: RHEED and laser reflectometry, which will be explained in the following sections.

Actually, this MBE system is also equipped with a N_2 plasma source. In theory, one can use either NH_3 or N_2 plasma or both, and it might be helpful to achieve N-rich condition for the growth of InGaN or InN at relatively low temperature (~ 450 °C). However, this component has not been employed in this thesis, since the growth temperature for (Al)GaN is quite high (~ 800 °C) and therefore the NH_3 cracking yield is sufficient.

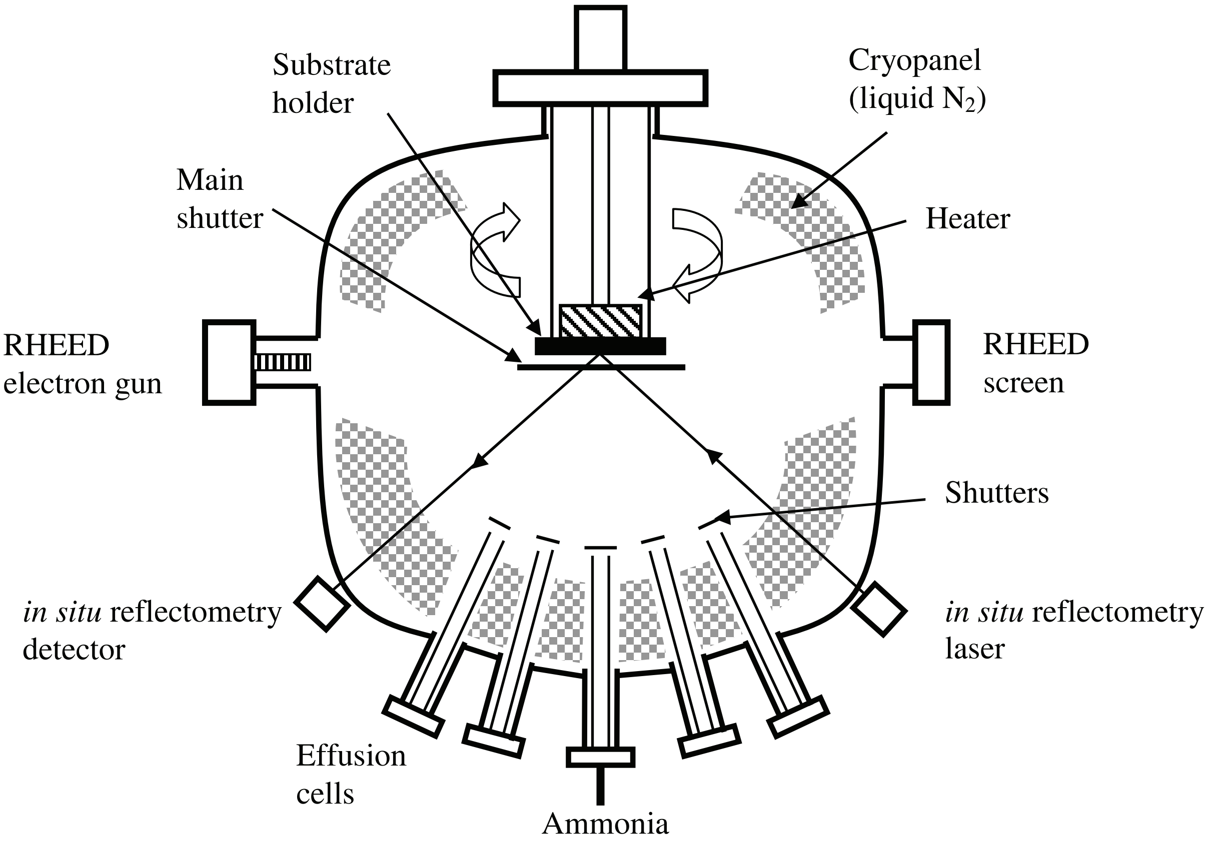

Figure 2.4 Schematic diagram (front view) of the MBE growth chamber.

2.2 Characterization methods

Samples can be characterized in two ways: either during the growth (*in situ*) or after the growth (*ex situ*). A comprehensive view can be obtained by combining the data from these two aspects.

2.2.1 Laser reflectometry

Due to the gaseous growth environment of HVPE and MOVPE, with pressure usually in the range of 10-10^3 mbar, it is impractical to apply some well-established *in situ* characterization techniques like reflection high-energy electron diffraction and mass spectrometry that require UHV work condition. The choice left is laser reflectometry (LR), an *in situ* tool for real-time diagnosis of the growth process including the growth rate, the surface roughness, and the absorption (*e.g.* $In_xGa_{1-x}N$ with large In fraction x).

Light reflection at the interfaces of multilayer structures can be predicted by the Fresnel equations. In short, LR provides information of the reflected light intensity following a periodic function. The period τ is given by

$$\tau = \frac{\lambda \cos\theta}{2nr_g} \tag{2.5}$$

where λ is the wavelength of the laser, n the refractive index of the layer, r_g the growth rate, and θ the angle of incidence.[36] The refractive indices of the nitrides, as introduced in section 1.3, are a function of wavelength, temperature, composition and crystal orientation.

The experimental LR set-ups for both the HVPE and MBE systems in our group are home-made. Each consists of a laser (diode) source, a photo-detector, and a commercial PC-based data acquisition system (figure 2.5). In the case of HVPE, the wavelength λ is 670 nm, θ is nearly zero (*i.e.* near-normal incidence); as for MBE, λ is 635 nm nm, θ is ~ 30°. Thus, one oscillation period ($n \approx 2.35$) refers to a layer thickness about 140 and 120 nm in the case of HVPE and MBE, respectively.

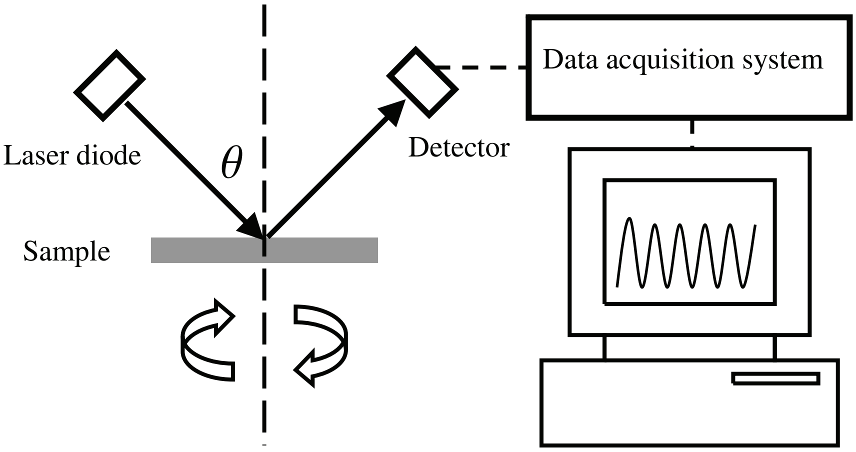

Figure 2.5 Schematic diagram of *in situ* LR set-up configuration.

When the light is either absorbed or scattered due to the roughening of the surface, the reflected light intensity damps. Since $Al_xGa_{1-x}N$ ($0 \le x \le 1$) investigated in this thesis is transparent at the wavelength region of 635-670 nm, absorption is excluded and any damping is attributed to surface roughening. The relation between surface roughness and the specular reflection at normal incidence can be simulated using simplified scattering theory[37] as

$$R = R_0 \exp[-(4\pi\sigma)^2 / \lambda^2] \qquad (2.6)$$

where R is the specular reflection of the sample surface and R_0 that of a perfectly smooth surface of the same material. σ is the root-mean-square (rms) surface roughness. This approximation for the reflectance damping is valid only for the so-called macroscopic roughness, that is, the length scale of the roughness is $> \lambda/2$ and $\sigma << \lambda$.[38] In other words, LR is not sensitive to the "microscopic roughness" for the features with size $<< \lambda$. Besides, margin of error has to be considered. For example, the normalized reflectance intensity for sapphire is ~ 6 % (room temperature), while the rotation of the substrate holder already induces an intensity fluctuation in the range of 0.5 %.

Figure 2.6 shows the reflectance signal recording a typical HVPE growth process of *c*-plane GaN on *c*-plane sapphire substrate, which consists of three parts: part A begins with the heating up to T ~ 600 °C and the following deposition of low temperature (LT) GaN nucleation layer (NL) at that temperature. The intensity, increasing when the NL thickens, is a reliable parameter to control the layer thickness. During the recrystallization step (part B), the intensity increases gradually due to the ramping of the growth temperature from 600 to 1000 °C and then it drops sharply as the NL gets etched and becomes rough when T > 1000 °C.[39] At this point, crystal islands are formed with the so-called Ostwald ripening phenomenon.[40] Part C covers the high temperature (HT) growth step, which initiates with a 3D growth mode as indicated by the low (close to zero) intensity. The intensity increases again when the islands start to coalesce. Once the coalescence process completes, the signal exhibits periodic oscillations due to the thickness variation of the GaN layer. Since the beam spot of the laser is about a few hundred micrometers in diameter, such oscillations indicate that the growth mode has transformed from 3D to 2D. The details can be found in Ref. 3. The inset provides an enlarged view of the oscillations in the part C, and the growth rate in this case is determined to be 10.6 µm/h.

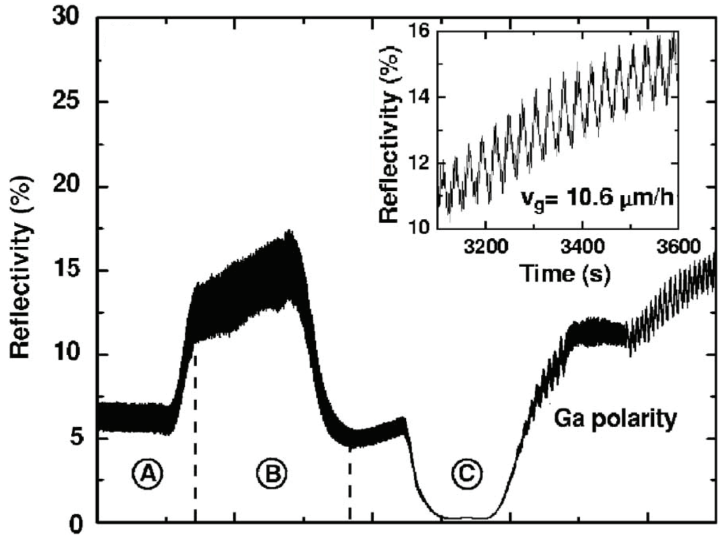

Figure 2.6 *In situ* LR signals monitoring the HVPE growth of *c*-plane GaN layer on *c*-plane sapphire, after Ref. 3. The inset shows the enlarged view of the oscillations in part (c) and the calculated growth rate.

2.2.2 Reflection high-energy electron diffraction

Ever since the late 1960s, the rapid development of MBE has been well connected to the increased understanding of reflection high-energy electron diffraction (RHEED). As an accurate *in situ* characterization technique, RHEED has high surface sensitivity with resolution on the atomic scale and is fully compatible with the crystal growth process, under the working condition of UHV. In the past decades, both experimental breakthroughs (*e.g.* the discovery of RHEED intensity oscillations[41]) and various relevant theoretical models have reached such an advanced degree that RHEED nowadays is an indispensable tool for MBE growth.

The RHEED system installed in the MBE reactor of our laboratory consists of an electron gun, a phosphor screen, a PC-based charge-coupled device (CCD) camera in front of the screen outside the growth chamber, and image-processing software. The acceleration voltage ranges from 10 to 15 kV.

RHEED diffraction patterns

The typical geometry of RHEED is schematically presented in figure 2.7. In kinematical scattering theory, the reflections are determined by a reciprocal lattice vector *G* defined by the Laue equation:

$$k' - k_0 = G \tag{2.7}$$

where wave vectors k_0 and k' are of the incident and diffracted beams. Assuming the scatterings are elastic only (*i.e.* $|k'| = |k_0|$), then this diffraction condition can be cast into the geometrical construction of the Ewald Sphere in reciprocal space, which is, in principle, the Fourier transform of the electron density distribution. The Ewald sphere is defined as the sphere around the origin of k_0 with radius $|k_0|$. Since the angle of incidence θ is small (usually in the range of 0.5-2.5°), RHEED is very surface-sensitive, as it only probes very few atomic layers beneath the surface. Thus, by approximating the sampled area to a 2D layer, the reciprocal lattice then degenerates into a set of one-dimensional rods along the z direction perpendicular to the surface. Each rod produces a reflection in the diffraction pattern, and the intersections of these reflections with Ewald sphere form circles (the so-called Laue circles) of radius L_n (n= 0, 1, 2…) centered at H, as shown in figure 2.7 (a). A detailed explanation of RHEED pattern can be found in the paper of Hernández-Calderón *et al.*[42]

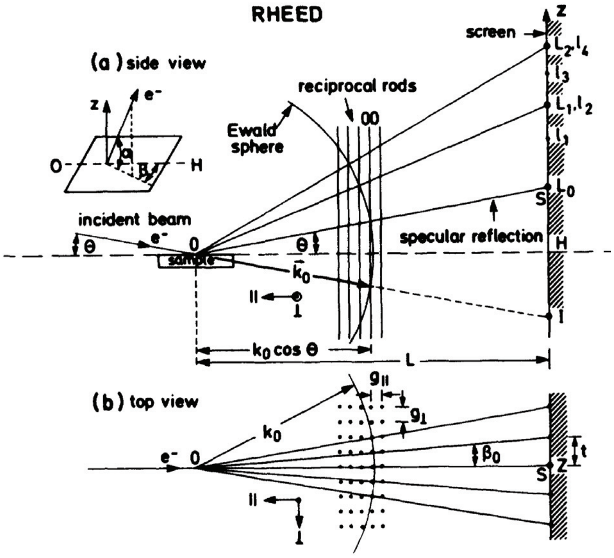

Figure 2.7 Ewald sphere construction and diffraction geometry of RHEED from both (a) side and (b) top view. Intensity maxima on the screen correspond to the projected intersections of the Ewald sphere with the reciprocal lattice, after Ref. 42.

The aforementioned kinematical scattering analysis is a simplified model. In fact, multiple elastic (also called "dynamical") scattering does occur when a diffracted beam, in turn, acts as a primary beam for subsequent diffraction. Furthermore, due to the strong electron-matter interaction, inelastic scattering induced by several different mechanisms (*e.g.* plasmon excitations) needs considering in the dynamical scattering analysis.[43] However, they are out of the scope of this thesis.

To give an example, RHEED patterns of *m*-plane GaN HVPE planar template are presented in figure 2.8. The azimuth angles are (a) [0001] and (b) $[11\bar{2}0]$ directions, respectively. The sample was heated at T ~ 700 °C, with NH_3 flux provided. Primary streaky patterns can be clearly observed, indicating the surface is 2D at a micro-scale. There is no sign of surface-reconstruction. Note the distance between adjacent streak patterns in the azimuth angle of [0001] is larger than that in $[11\bar{2}0]$, because the distance is inversely proportional to the lattice constants (a = 3.189 Å, c = 5.185 Å).

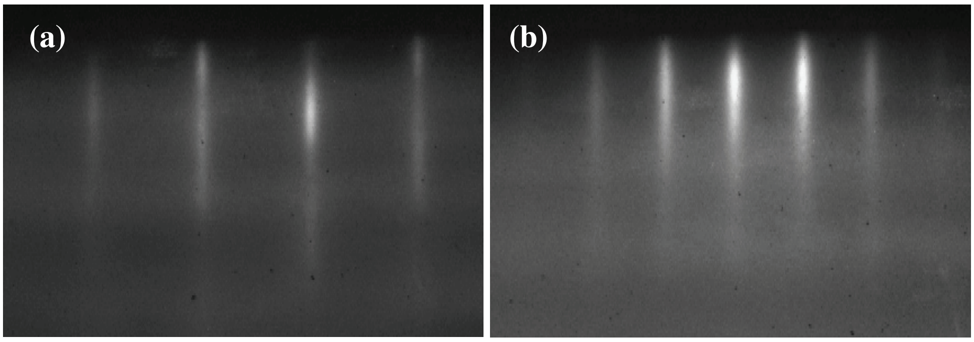

Figure 2.8 RHEED patterns of *m*-plane HVPE GaN planar template, in the azimuth angles of (a) [0001] and (b) $[11\bar{2}0]$.

RHEED oscillations

The RHEED specular beam intensity oscillations provide *in situ* and real-time information on the dynamics of MBE growth (*e.g.* growth rate and alloy composition). They are generally observed during layer-by-layer (Frank-van der Merwe) growth mode and 2D nucleation. The intensity of the specular spot is usually plotted as a function of time, where the period of an oscillation corresponds to the growth of one crystal monolayer (ML).

For NH_3 source MBE, the RHEED oscillations damp rapidly at the standard growth temperature of GaN (T ~ 800 °C), due to the transition from 2D nucleation to step flow growth mode.[35] Thus, the suitable temperature for the observation of the specular beam intensity variations should be lower, around 600 °C. Figure 2.9 is the RHEED oscillations recorded during the homoepitaxy of *m*-plane GaN on HVPE planar template at T = 580 °C in the azimuth angle of GaN $[11\bar{2}0]$. The growth rate can be precisely determined to be 0.63 ML/s.

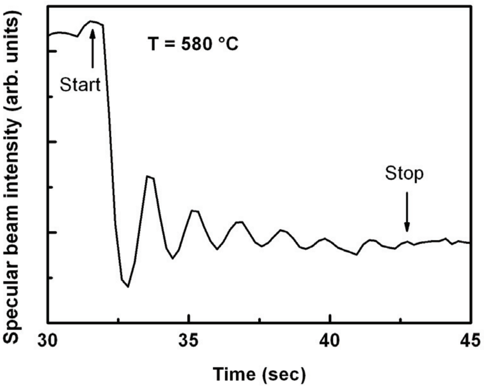

Figure 2.9 RHEED specular beam intensity oscillations for *m*-plane GaN growth as a function of the time.

2.2.3 High resolution X-ray diffraction

X-ray diffraction (XRD), a non-destructive *ex situ* analytical technique, studies the diffraction patterns when X-rays interact with a crystalline substance. It is able to reveal both qualitative and quantitative information about the crystallographic structure, chemical composition, and physical properties of the crystal.

The fundamental of XRD lies in the Bragg's law:

$$n\lambda = 2d \cdot \sin\theta \tag{2.8}$$

where n is an integer determined by the order; λ the wavelength of X-ray; d the spacing between the atomic planes; and θ the angle between the incident rays and the scattering planes. Here, the term $n\lambda$ indicates that it measures the number of wavelengths fitting between two rows of atoms, *i.e.* the distances in the reciprocal space, instead of the atomic distance in real space.

According to the kinematical scattering theory mentioned in section 2.2.2 (RHEED), when the reciprocal lattice vector G is equal to the change in the wave vectors, *i.e.*, $G = k' - k_0$ (the Laue equation), where k_0 and k' are the wave vectors of the incident and the diffracted X-ray beams, the constructive interference occurs (the so-called Ewald construction). The radius of the Ewald sphere is $1/\lambda$. Once λ and the lattice d are fixed, all the wave vectors can be defined through ω and 2θ (ω is the angle between the incident beam and the sample surface and θ is the angle between the incident beam and a crystal plane. They will be different when the crystal plane is not parallel to the sample surface). In addition, for hexagonal unit cell, the relation of *d* to the lattice parameters *a* and *c* is given by the *hkl* Miller indices:

$$\left(\frac{1}{d}\right)^2 = \frac{4}{3}\cdot\frac{h^2+k^2+h\cdot k}{a^2}+\frac{l^2}{c^2} \tag{2.9}$$

The diffracted intensity is proportional to the square of the Fourier transform of the charge density. Ideally, for perfect and infinite crystal, the diffraction peaks are as sharp as delta function. In practice, however, the diffraction peaks are broadened, due to extrinsic factors like strains, wafer curvatures, defects, finite size of the crystal, and the resolution of the instrument.

XRD scans have been performed in a four-circle diffractometer as schematically depicted in figure 2.10. In addition to the aforementioned ω and 2θ, there are two more angles involved: ϕ and χ. ϕ is the angle of rotation around the axis normal to the sample plane. χ reveals how much the sample is tilted off the vertical plane.

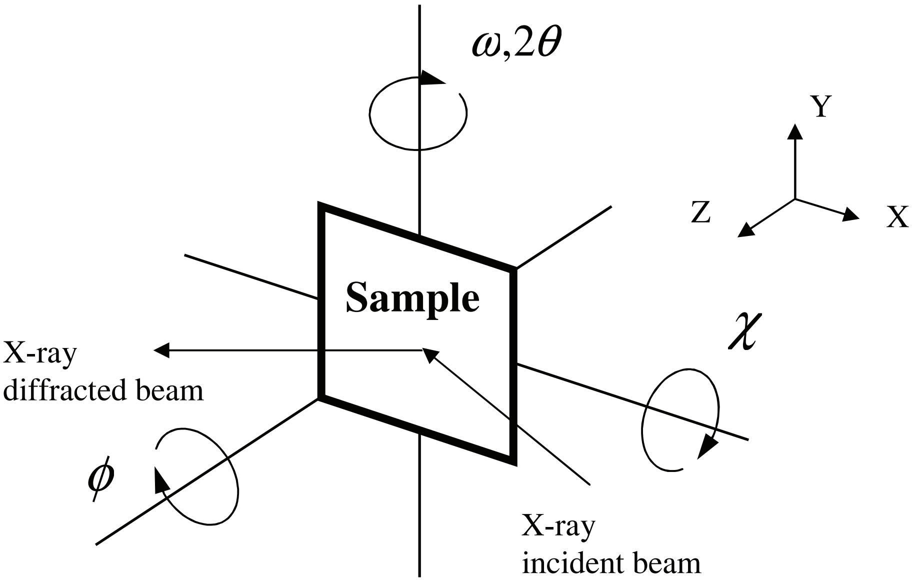

Figure 2.10 Schematic drawing of a four-circle diffractometer. The crystal plane under test is perpendicular to the horizontal level (*i.e.* $\chi = 0$).

In this thesis, some scan modes have been carried out to characterize the samples:

(a) $\omega - 2\theta$ scan: it is used to determine the crystal orientations of the substrate, since the lattice constant along the *z*-axis is equal to $d = \frac{n\lambda}{2\sin\theta}$, according to equation 2.8, where θ is angle of the rocking curve peak. Here, $\chi = 0$, that is, the sample plane is always aligned perpendicular to the horizontal level.

(b) ω scan: $\chi = 0$, and 2θ is fixed at the angle of peak measured in (a). The scan is used to indirectly assess defect densities through the mosaic model, a simplified model of real crystals, where the twist and tilt of the mosaic crystal give rise to the broadening of ω rocking curve and are linked to the edge and screw threading dislocations (TDs), respectively.[44, 45] Besides, the TD densities can be obtained from the Williamson-Hall analysis.[46] Furthermore, for non-polar GaN epilayers, a striking feature of the microstructure of the epilayer is the high density of basal-plane stacking faults (BSFs), which is reported to be responsible for the anisotropy in X-ray ω rocking curve widths and could be estimated by a modified Williamson-Hall analysis, under a quite strong assumption that BSFs are the only source for broadening.[47]

(c) off-axis ϕ scan. This scan is used to reveal the in-plane epitaxial relationship between the GaN epilayer and the sapphire substrate. The sample is tilted at a certain angle $\chi \neq 0$, and then rotates (ϕ: 0 - 360°) during the scan.

More details about XRD of III-nitrides can be found in the review by M. A. Moram and M. E. Vickers.[48]

2.2.4 Atomic force microscope

Atomic force microscope (AFM), or scanning force microscope, is a high resolution tool for imaging, measuring and manipulating matters at micro- or nano-scale. In this thesis, the application of AFM is limited to surface morphology investigation.

The standard configuration of AFM is shown in figure 2.11. A cantilever in the size of a few millimeters, with a sharp tip (radius of curvature in the order of a few tens of nanometer) at its apex, is used to scan the sample surface line by line. The deflection of the cantilever resulting from atomic force interaction is measured by a pair of laser and photo-detector. Here, AFM always works in the contact mode, where the force between the tip and the surface is kept constant during scanning by maintaining a constant deflection. More details can be found in the literature of D. Sarid.[49]

The typical surface morphology of *c*-plane GaN epilayer grown by HVPE is presented in the inset of figure 2.11. The image size is 20×20 μm^2, with a root-mean-square (rms) roughness of ~ 0.8 nm and an average height of ~ 3.7 nm. One unique feature is the “step” morphology, in agreement with the step-flow growth mode of GaN at usual growth temperatures. The average height of the terrace is ~ 0.2 nm, roughly equal to one ML (0.26 nm), and the average distance of neighboring terraces is ~ 100 nm. Actually, this morphology is quite similar to that of MOVPE-grown *c*-GaN layer, with surface depressions correlated to the surface terminations of dislocations.[50] The dark spots marked by the arrows correspond to threading dislocations (TDs), among which screw and mixed dislocations can be observed since they have a Burgers vector component perpendicular to the surface. However, pure edge dislocations are hardly visible. The estimated screw and mixed TD density is ~ 10^8 cm^{-2}, a state-of-the-art level for GaN epilayers grown on sapphire.

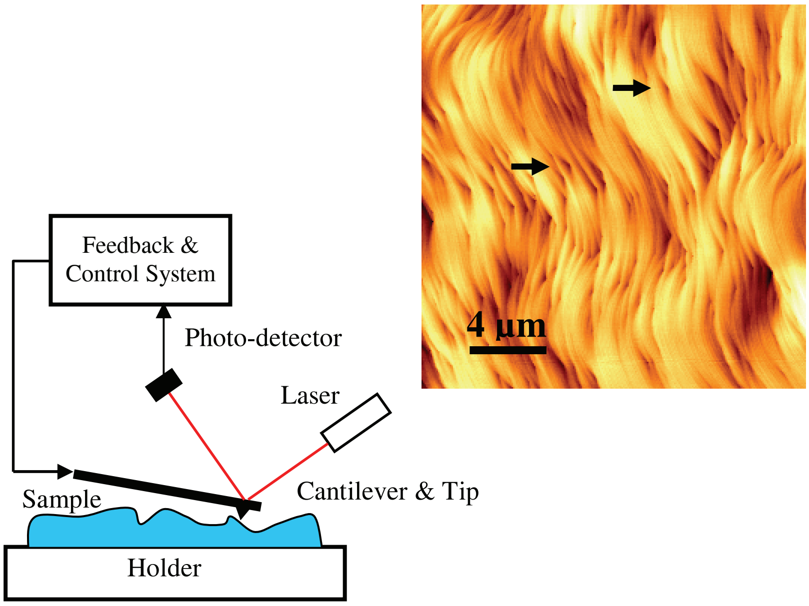

Figure 2.11 Diagram of AFM configuration (left) and a representative AFM image of *c*-plane HVPE GaN surface in the size of 20×20 µm^2 (right).

2.2.5 Photoluminescence and reflectance spectroscopy

Spectroscopy is to analyze the light spectrum either emitted or reflected from the material. The former is called photoluminescence (PL) and the latter reflectance or reflectivity (RL). Both are nondestructive methods to characterize the optical properties of III-nitrides. Further details can be found in the literature of M. O. Manasreh and H. X. Jiang.[51]

There are two spectroscopy setups installed in our laboratory. One is a standard PL setup equipped with two lasers: a Nd: YAG pulsed laser (λ = 266 nm) and a He-Cd continuous wave (cw) laser (λ = 325 nm). The other is a home-made "combined" setup which can provide PL, µ-PL, and RL, equipped with a frequency-doubled cw Ar$^+$ laser (λ = 244 nm). The details of this setup are an important part of Dobri Simeonov (a former PhD student of our group)'s thesis, and readers are kindly requested to refer to that for more information.[52]

Figure 2.12 displays low temperature (T = 8 K) PL and RL spectra of a *c*-plane HVPE GaN epilayer (d ~ 8 µm) grown on *c*-plane sapphire. X_A free-exciton at 3.4837 eV and X_B at 3.4910 eV correspond to A and B valence bands, respectively, as mentioned in section 1.3. They are confirmed by the RL curve. These values are larger than those of homoepitaxial layers,[53] indicating a slight compressive strain, something usual for thin film GaN deposited on sapphire due to the mismatch of TECs. X_C is hardly resolved in the spectra. Besides, there are two PL emission lines related to bound excitons: the neutral donor bound exciton (D^0, X_A) and the neutral acceptor bound exciton (A^0, X_A). The FWHM of the D^0, X_A and X_A is 3.0 and 3.4 meV, respectively, suggesting that the material quality is quite good.

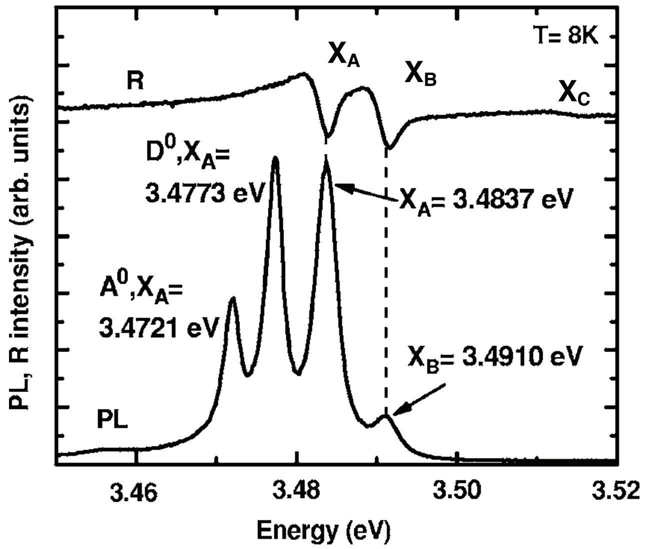

Figure 2.12 Low temperature (T = 8 K) PL and RL spectra of *c*-plane GaN heteroepitaxial layer grown on sapphire by HVPE, after Ref. 3.

2.3 Summary

This chapter introduces the experimental equipments and tools utilized in this thesis:

(1) Epitaxial growth: HVPE and NH_3 source MBE.

(2) In addition to those aforementioned characterization tools, cathodoluminescence (CL), transmission electron microscopy (TEM), scanning electron microscopy (SEM), and Nomarski optical microscope have also been used to analyze samples. They are critical methods and this thesis would not be complete without their results. However, since the CL and TEM measurements were conducted by other research groups (TEM: CIME EPFL and CRHEA–CNRS, CL: LOEQ EPFL), they are not elaborated in this chapter. Besides, SEM and Nomarski microscopy are conventional imaging tools, so their introductions are skipped, too. All the tools used in this thesis is summarized below:

Characterization tools
- Surface morphology: LR, RHEED, SEM, Nomarski optical microscopy, and AFM
- Structure properties: XRD and TEM
- Optical properties: CL, PL (including μ-PL) and RL

Bibliography

---

[1] H. P. Maruska and J. J. Tietjen, “The preparation and properties of vapor-deposited single-crystalline GaN”, *Applied Physics Letters*, vol. 15, no. 10, pp. 327-329, 1969.

[2] B. Lucznik, B. Pastuszka, I. Grzegory, M. Bockowski, G. Kamler, E. Litwin-Staszewska, and S. Porowski, “Deposition of thick GaN layers by HVPE on the pressure grown GaN substrates”, *Journal of Crystal Growth*, vol. 281, no. 1, pp. 38-46, 2005.

[3] D. Martin, J. Napierala, M. Ilegems, R. Butté, and N. Grandjean, “High quality thin GaN templates grown by hydride vapor phase epitaxy on sapphire substrates”, *Applied Physics Letters*, vol. 88, no. 24, pp. 241914, 2006.

[4] Hydride Vapour Phase Epitaxy, Oxford Instruments PLC, http://www.oxford-instruments.com/products/etching-deposition-growth/processes-techniques/hvpe/Pages/hydride-vapour-phase-epitaxy.aspx

[5] S. S. Liu and D. A. Stevenson, “Growth kinetics and catalytic effects in the vapor phase epitaxy of gallium nitride”, *Journal of Electrochemical Society*, vol. 125, no. 7, pp. 1161-1169, 1978.

[6] V. S. Ban, “Mass spectrometric studies of vapor phase crystal growth I. $GaAs_xP_{1-x}$ system ($0 \leq x \leq 1$)”, *Journal of Electrochemical Society*, vol. 118, no. 9, pp. 1473-1478, 1971.

[7] V. S. Ban, “Mass spectrometric studies of vapor phase crystal growth II. GaN”, *Journal of Electrochemical Society*, vol. 119, no. 6, pp. 761-765, 1972.

[8] V. K. Gupta, K. L. Averett, M. W. Koch, B. L. Mcintyre, and G. W. Wicks, “Selective Area growth of GaN using Gas Source Molecular Beam Epitaxy”, Journal of Electronic Materials, vol. 29, no. 3, pp. 322-324, 2000.

[9] M. Mesrine, N. Grandjean, and J. Massies, “Efficiency of NH_3 as nitrogen source for GaN molecular beam epitaxy”, *Applied Physics Letters*, vol. 72, no. 3, pp.350-352, 1997.

[10] R. Cadoret, “Growth mechanisms of (00.1) GaN substrates in the hydride vapour-phase method: surface diffusion, spiral growth, H_2 and $GaCl_3$ mechanisms”, *Journal of Crystal Growth*, vol. 205, no. 1-2, pp. 123-135, 1999.

[11] Y. Kumagai, K. Takemoto, T. Hasegawa, A. Koukitu, and H. Seki, “Thermodynamics on tri-halide vapor-phase epitaxy of GaN and $In_xGa_{1-x}N$ using $GaCl_3$ and $InCl_3$”, *Journal of Crystal Growth*, vol. 231, no. 1-2, pp. 57-67, 2001.

[12] A. Trassoudaine, R. Cadoret, and E. Gil-Lafon, “ Temperature influence on the growth of gallium nitride by HVPE in a mixed H2/N2 carrier gas”, *Journal of Crystal Growth*, vol. 260, no. 1-2, pp. 7-12, 2004.

[13] A. S. Segal, A. V. Kondratyev, S. Y. Karpov, D. Martin, V. Wagner, and M. Ilegems, “Surface chemistry and transport effect in GaN hydride vapor phase epitaxy”, *Journal of Crystal Growth*, vol. 270, no. 3-4, pp. 384-395, 2004.

[14] C. E. C. Dam, A. P. Grzegorczyk, P. R. Hageman, R. Dorsman, C. R. Kleijn, and P. K. Larsen, “The effect of HVPE reactor geometry on GaN growth rate – experiments versus simulations”, *Journal of Crystal Growth*, vol. 271, no. 1-2, pp. 192-199, 2004.

---

[15] J. Fritsch, O. F. Sankey, K. E. Schmidt, and J. B. Page, “*Ab initio* calculation of the stoichiometry and structure of the (0001) surfaces of GaN and AlN”, *Physical Review B*, vol. 57, no. 24, pp. 15360 -15371, 1998.

[16] C. A. Pignedoli, R. D. Felice, and C. M. Bertoni, “Dissociative chemisorption of NH_3 molecules on GaN (0001) surfaces”, *Physical Review B*, vol. 64, no. 11, pp. 113301, 2001.

[17] A. L. Rosa and J. Neugebauer, “First-principles calculations of the structural and electronic properties of clean GaN (0001) surfaces”, *Physical Review B*, vol. 73, no. 20, pp. 205346, 2006.

[18] P. Kempisty and S. Krukowski, “Crystal growth of GaN on (0001) face by HVPE: Ab initio simulations”, *Journal of Crystal Growth*, vol. 310, no. 5, pp. 900-905, 2008.

[19] S. Krukowski, P. Kempisty, and P. Strak, “Role of chlorine in the dynamics of GaN (0001) surface during HVPE GaN growth – Ab initio study”, *Journal of Crystal Growth*, vol. 310, no. 5, pp. 900-905, 2008, vol. 310, no. 7-9, pp. 1391-1397, 2008.

[20] A. Trassoudaine, E. Aujol, P. Disseix, D. Castelluci, and R. Cadoret, “Experimental and theoretical study of the growth of GaN on sapphire by HVPE”, *physica. status. solidi. (a)*, vol. 176, no. 1, pp. 425-428, 1999.

[21] M. Henini, “Molecular beam epitaxy from research to mass-production – Part 1”, *III-Vs Review*, vol. 9, no. 3, pp. 32-34, 1996.

[22] A. Y. Cho, “How molecular beam epitaxy (MBE) began and its projection into the future”, *Journal of Crystal Growth*, vol. 201/202, pp. 1-7, 1999.

[23] J. R. Arthur, “Molecular beam epitaxy”, *Surface Science*, vol. 500, no. 1-3, pp. 189-217, 2002.

[24] A. Y. Cho, “Epitaxial growth of gallium phosphide on cleaved and polished (111) calcium fluoride”, *Journal of Applied Physics*, vol. 41, no. 2, pp. 782-786, 1970.

[25] B. Voigtländer, “Scanning tunneling microscopy studies during semiconductor growth”, Micron, vol. 30, no. 1, pp. 33-39, 1999.

[26] K. Ploog and A. Fischer, “Surface segregation of Sn during MBE of *n*-type GaAs established by SIMS and AES”, *Journal of Vacuum Science & Technology*, vol. 15, no. 2, pp. 255-259, 1978.

[27] F. G. Celii, Y.-C. Kao, and H.-Y. Liu, “*In situ* composition monitoring of InGaAs/InP using quadrupole mass spectrometry”, *Journal of Vacuum Science & Technology A*, vol. 14, no. 6, pp. 3202-3207, 1996.

[28] A. Y. Cho and M. B. Panish, “Magnesium-doped GaAs and AlxGa1-xAs by molecular beam epitaxy”, *Journal of Applied Physics*, vol. 43, no. 12, pp. 5118-5123, 1972.

[29] H. Okumura, S. Misawa, and S. Yoshida, “Epitaxial growth of cubic and hexagonal GaN on GaAs by gas-source molecular-beam epitaxy”, *Applied Physics Letters*, vol. 59, no. 9, pp. 1058-1060, 1991.

[30] T. D. Moustakas, T. Lei, and R. J. Molnar, “Growth of GaN by ECR-assisted MBE”, *Physica B*, vol. 185, no. 1-4, pp. 36-49, 1993.

---

[31] R. C. Powell, N.-E. Lee, Y.-W. Kim, and J. E. Greene, “Heteroepitaxial wurtzite and zinc-blende structure GaN grown by reactive-ion molecular-beam epitaxy: growth kinetics, microstructure, and properties”, *Journal of Applied Physics*, vol. 73, no. 1, pp. 189-204, 1993.

[32] N. Grandjean, M. Leroux, M. Laugt, and J. Massies, “Gas source molecular beam epitaxy of wurtzite GaN on sapphire substrates using GaN buffer layers”, *Applied Physics Letters*, vol. 71, no. 2, pp. 240-242, 1997.

[33] N. Grandjean, J. Massies, and M. Leroux, “Nitridation of sapphire. Effect on the optical properties of GaN epitaxial overlayers”, *Applied Physics Letters*, vol. 69, no. 14, pp. 2071-2073, 1996.

[34] N. Grandjean, J. Massies, P. Vennéguès, M. Laügt, and M. Leroux, “Epitaxial relationship between GaN and Al_2O_3(0001) substrates”, *Applied Physics Letters*, vol. 70, no. 5, pp. 643-645, 1997.

[35] N. Grandjean and J. Massies, “GaN and AlxGa1-xN molecular beam epitaxy monitored by reflection high-energy electron diffraction”, *Applied Physics Letters*, vol. 7, no. 13, pp. 1816-1818, 1997.

[36] B. Beaumont, M. Vaille, T. Boufaden, B. el Jani, and P. Gibart, “High quality GaN grown by MOVPE”, *Journal of Crystal Growth*, vol. 170, no. 1-4, pp. 316-320, 1997.

[37] H. E. Bennett and J. O. Porteus, “Relation between surface roughness and specular reflectance at normal incidence”, *Journal of Optical Society of America*, vol. 51, no. 2, pp.123-129, 1961.

[38] R. S. Balmer, C. Pickering, A. J. Pidduck, and T. Martin, “Modelling of high temperature optical constants and surface roughness evolution during MOVPE growth of GaN using in-situ spectral reflectometry”, *Journal of Crystal Growth*, vol. 245, no. 3-4, pp. 198-206, 2002.

[39] D. D. Koleske, M. E. Coltrin, K. C. Cross, C. C. Mitchell, and A. A. Allerman, “Understanding GaN nucleation layer evolution on sapphire”, *Journal of Crystal Growth*, vol. 273, no. 1-2, pp. 86-99, 2004.

[40] S. A. Kukushkin, V. N. Bessolov, A.V. Osipov, and A. V. Luk’yanov, “Mechanism and kinetics of early growth stages of a GaN film”, *Physics of the Solid State*, vol. 44, no. 7, 1399-1405, 2002.

[41] J. J. Harris, B. A. Joyce, and P. J. Dobson, “Oscillations in the surface structure of Sn-doped GaAs during growth by MBE”, *Surface Science Letters*, vol. 103, no. 1, pp. L90-L96, 1981.

[42] I. Hernández-Calderón and H. Höchst, “New method for the analysis of reflection high-energy electron diffraction: α-Sn(001) and InSb(001) surfaces”, *Physical Review B*, vol. 27, no. 8, pp. 4961-4965, 1983.

[43] Z. L. Wang, “Dynamical calculations for RHEED and REM including the plasmon inelastic scattering: I. Total elastic plus inelastic scattering”, *Surface Science*, vol. 215, no. 1-2, pp. 201-216, 1989.

[44] C. G. Darwin, “Röntgen-ray reflection”, *Philosophical Magazine*, vol. 27, pp. 315-333, 1914.

---

[45] C.G. Darwin, “Reflection of X-rays from imperfect crystals”, *Philosophical Magazine*, vol. 43, pp. 800-829, 1922.

[46] G. K. Williamson and W. H. Hall, “X-ray line broadening from filed aluminum and wolfram”, *Acta Metallurgica*, vol. 1, no. 1, pp. 22-31, 1953.

[47] M. B. McLaurin, A. Hirai, E. Young, F. Wu, and J. S. Speck, “Basal plane stacking-fault related anisotropy in X-ray rocking curve widths of *m*-plane GaN”, *Japanese Journal of Applied Physics*, vol. 47, no. 7, pp. 5429-5431, 2008.

[48] M. A. Moram and M. E. Vickers, “X-ray diffraction of III-nitrides”, Reports on Progress in Physics, vol. 72, no. 3, pp.036502, 2009.

[49] D. Sarid, *Scanning Force Microscopy, Oxford Series in Optical and Imaging Sciences*, Oxford University Press, New York, 1991.

[50] B. Heying, E. J. Tarsa, C. R. Elsass, P. Fini, S. P. DenBaars, and J. S. Speck, “Dislocation mediated surface morphology of GaN”, *Journal of Applied Physics*, vol. 85, no. 9, pp. 6470-6476, 1999.

[51] M. O. Manasreh and H. X. Jiang, *III-nitride semiconductors: optical properties I (Optoelectronic properties of semiconductors and superlattices, vol. 13)*, Taylor & Francis Books, 2002.

[52] D. Simeonov, *Synthesis and optical investigation of single polar GaN/AlN quantum dots*, PhD thesis, Ecole polytechnique fédérale de Lausanne, 2008.

[53] K. Kornitzer, T. Ebner, K. Thonke, R. Sauer, C. Kirchner, V. Schwegler, M. Kamp, M. Leszczynski, I. Grzegory, and S. Porowski, “Photoluminescence and reflectance spectroscopy of excitonic transitions in high-quality homoepitaxial GaN films”, *Physical Review B*, vol. 60, no. 3, pp. 1471-1473, 1999.

3. HVPE growth of non-polar GaN epilayers

3.1 Planar *a*-plane GaN grown on *r*-plane sapphire

In this section, three different growth procedures of *a*-plane GaN on *r*-plane sapphire are described: (3.1.1) one-step, (3.1.2) two-step and (3.1.3) pressure-variation. Characterization results of structural and optical properties are summarized in 3.1.4. Before the discussion of growth, a brief study of sapphire surface is presented below.

Surface treatment of *r*-plane sapphire

As we know, before the growth takes place, sapphire surface is often thermally treated in order to optimize the growth nucleation. The treatments include annealing in an ambient of certain gases such as N_2, H_2, and NH_3. N_2 gas is inert, while H_2 and NH_3 are active, so their impact on sapphire surface could be different.

First, the effect of N_2 is studied. Figure 3.1.1 is a set of AFM images of equal size (2×2 μm^2) measured on three wafers: (a) represents as-received wafer from the supplier without any treatment. The surface is featured by terraces, though they can hardly be observed as their edges are quite blurred (marked by the dash guidelines). The average distance between neighboring terraces are ~ 1.2 μm and the height of the terrace is ~ 0.25 nm, roughly equal to the thickness of the "surface building block" mentioned in section 1.5. (b) displays the surface after being treated in N_2 at T ~ 1050 °C for 20 min. The terrace edge is better resolved and the distance is about the same as in (a). When the treatment time is prolonged to 1 hour, the surface turns out to be much better ordered as the terrace edges are sharp and well aligned, as shown in (c). The average terrace distance is ~ 0.5 μm.

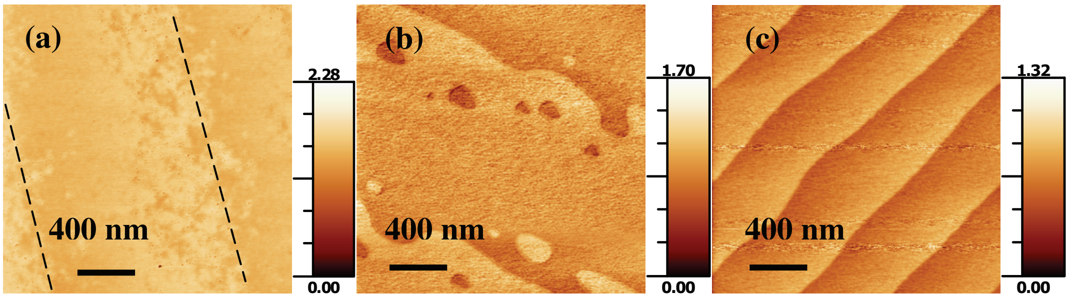

Figure 3.1.1 AFM images of different sapphire surfaces: (a) as-received from supplier, (b) and (c) are those treated for 20 min and 1 hour in N_2 at T ~ 1050 °C, respectively. The rms roughness for these three is less than 0.1 nm.

The presence of terraces is related to the tiny tilt of surface orientation, since as-received substrates have an orientation error margin of ±0.1°. Calculations show that the tilt angle of figure 3.1 (a) and (b) is ~ 0.01°, and ~ 0.03° for figure 3.1 (c). The direction of the terrace edge seems random and local-dependent, probably due to chemical-mechanical polishing.

Next, the sapphire surface annealed in active H_2/NH_3 gases is also studied. For one-step growth, it usually takes ~ 10 min for the growth temperature to increase from T ~ 1000 °C to the growth temperature T ~ 1080 °C. During that time period, the sapphire surface is nitridated. AFM image shows that the surface gets rough after nitridation, with a rms roughness of 0.9 nm on a scale of 2×2 μm^2 (figure 3.1.2). This is attributed to stress-induced protrusions of amorphous AlO_xN_{1-x} layer under nitridation.[1]

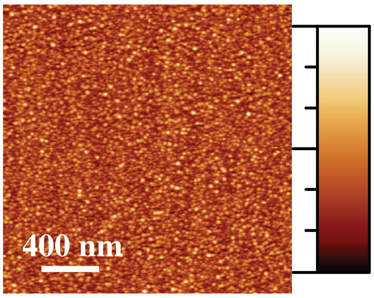

Figure 3.1.2 AFM image (2×2 μm^2) shows the sapphire surface after being treated in H_2 and NH_3 at T > 1000 °C for ~ 10 min.

To sum up, when annealed in N_2, *r*-plane sapphire surface remains atomic flat and no micro facet or step bunching has been observed. This indicates that *r*-plane is quite stable. As I will discuss in section 3.3, in comparison, micro-facets sometimes will appear in *m*-plane sapphire during HT annealing, due to the minimization of surface energy.[2] Besides, HT nitridation prior to the growth helps form an AlO_xN_{1-x} thin layer on *r*-plane sapphire surface. It is expected to promote nucleation, though it introduces a side effect: a modest degradation in surface smoothness. Therefore, in the subsequent experiments, prior to the growth, the sapphire surface is thermally annealed in N_2 (T up to 1000 °C) and then gets nitridated in H_2/NH_3 ambient (T from 1000 to 1080 °C).

3.1.1 One-step growth procedure

"One-step" refers to direct HT growth of GaN on sapphire without low temperature buffer layer. The influences of several growth parameters are discussed below.

The influence of the growth pressures (P_g)

To illustrate this point, various pressures (P_g = 800, 400, 200, 150, 100, and 75 mbar) have been tested, with other parameters kept constant: nominal V/III ratio 80, T ~ 1080 °C, carrier gas H_2 and N_2, growth time 10 min, and the layer thickness ~ 3 μm.

Among these samples, there are three representative ones: A (P_g = 400 mbar), B (P_g = 200 mbar) and C (P_g = 100 mbar). Their *in situ* laser reflectometry (LR) records and the Nomarski optical micrographs are presented in figure 3.1.3.

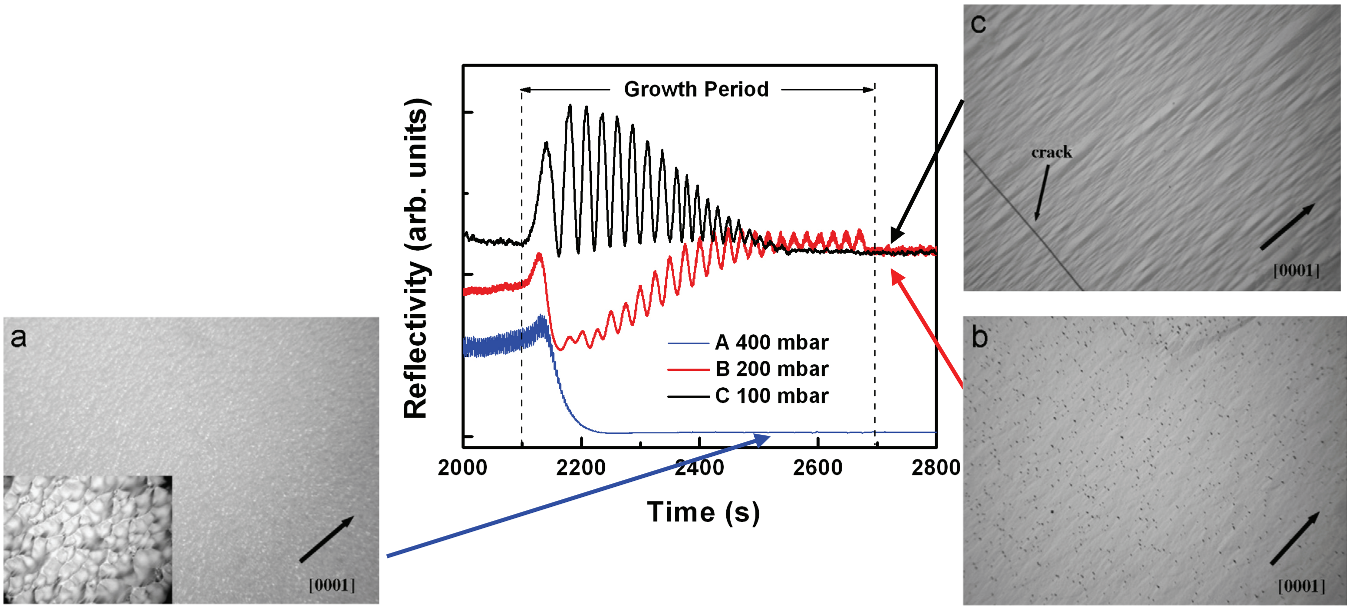

Figure 3.1.3 *In situ* LR record signals for three samples A (blue), B (red), and C (black). Their surface morphologies are presented in Nomarski optical micrographs (a) – (c), respectively, with identical scale of 700 × 525 µm^2. The inset in (a) is also an optical micrograph with scale of 140 × 105 µm^2. It provides an enlarged view of sample A.

For sample A (P_g = 400 mbar), LR signals (blue) dropped soon after the growth began and stayed near zero, indicating 3D growth mode. The inset of figure 3.1.3 (a) reveals that the surface is covered by large crystal islands (diameter ~ 10 µm). Such surface is too rough for AFM scans. However, for a much shorter growth time, AFM analysis can be performed, as presented in figure 3.1.4 (a). It exhibits the surface after 2 min growth, where islands of various sizes are randomly distributed on the surface. There is a strong growth anisotropy as the islands are well aligned along GaN *c*-axis. The sample grown at P_g = 800 mbar shares the similar surface morphology of sample A.

For sample B (P_g = 200 mbar), the growth mode began with 3D, as LR signals dropped (red) first, and then transformed into 2D, indicated by the gradual increase of the signal intensity and occurrence of LR oscillations. The surface is relatively smooth but decorated with pits, *i.e.* black dots, as shown in figure 3.1.3 (b). AFM image reveals that such micrometer-scale pits are of triangular shape [figure 3.1.4 (b)].[3] In areas without pits, the rms roughness on 5×5 µm^2 scale is ~ 7 nm.

For sample C (P_g = 100 mbar), the amplitude of the reflectivity oscillations damps shortly after the first two periods (black) and the growth mode is 2D. The surface is characterized by anisotropic-ellipsoidal features along *c*-axis [figure 3.1.3 (c)]. Besides, there are cracks aligned perpendicular to *c*-axis. The growth anisotropy is confirmed by AFM image with a rms roughness ~ 5 nm (5×5 µm^2 scan) [figure 3.1.4 (c)]. The samples grown at P_g = 75 and 150 mbar have similar surface morphology.

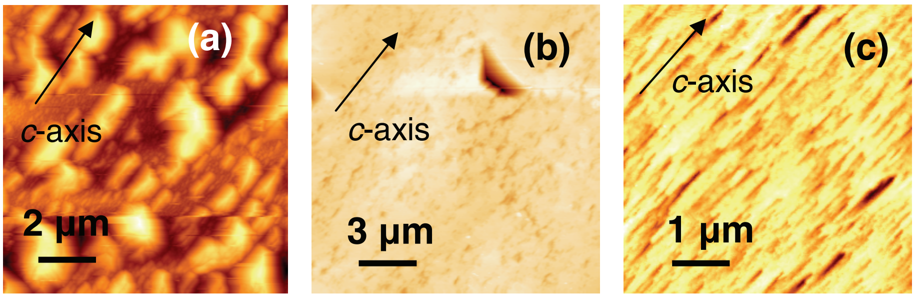

Figure 3.1.4 AFM images of surface morphology of *a*-plane GaN grown on *r*-plane sapphire: (a) sample A (10×10 µm^2) after 2 min growth, (b) B (15×15 µm^2), and (c) C (5×5 µm^2) after 10 min growth.

This set of experiments clearly illustrates that the reactor pressure has a strong impact on the growth mode and consequently the surface morphology. As a result, the growth window of *a*-plane seems quite narrow since flat *a*-plane layer cannot be achieved at $P_g > 200$ mbar. The crystal habits of GaN determine that the stable planes are $\{0001\}$, $\{11\bar{2}2\}$ and $\{1\bar{1}0l\}$ (l = 0, 1, 2).[4, 5, 6] Indeed, a closer look at figure 3.1.4 (a) reveals that the crystal islands are composed of inclined facets. They may be of $\{1\bar{1}01\}$ orientation, which is quite stable under N-rich condition.[6] By reducing the pressure, the surface N atoms are not stabilized and then *a*-plane, with its lower dangling bonds per unit area (14.0 nm^{-2}), becomes more energetically favorable.[6] This explains why planar *a*-plane can only be grown when $P_g \leq 200$ mbar. Particularly, $P_g = 200$ mbar is somehow within a critical region, in the sense that some other stable and slow growing planes, *e.g.* $(000\bar{1})$ and $\{10\bar{1}1\}$, still appear and form the triangular pits observed in figure 3.1.4 (b).[7] Based on *in situ* LR, these pits probably form during the coalescence of crystal islands. Even though *a*-plane prevails when $P_g < 200$ mbar, the surface roughening occurs, as indicated by the oscillation-intensity damping with the increase of the layer thickness.

Another uncommon phenomenon is the strong growth anisotropy along GaN [0001] direction. For example, the crystal islands of sample A are aligned along *c*-axis [figure 3.1.4 (a)] and the stripe-feature of sample C is also along *c*-axis [figure 3.1.4 (c)]. Such anisotropy has been widely reported on *a*-plane GaN epilayers grown on substrates like sapphire,[8, 9, 10, 11] ZnO,[12] and SiC[13], using various growth methods. H. Wang *et al.* argue that the bond configuration on *a*-plane GaN favors growth along [0001] direction.[10] Theoretical calculations based on density-functional theory suggest that this phenomenon is related to a strong in-plane anisotropy of the diffusion barriers for Ga surface adatom.[14]

Besides, cracks are observed in sample C, resulting from the plastic relief of the tensile strain. The unit cells for *a*-plane GaN and *r*-plane sapphire are 5.185 × 5.524 Å^2 and 5.128 × 4.759 Å^2, respectively. Hence, assuming pseudomorphic growth, the biaxial strain in *a*-plane GaN thin layers should be compressive[*]: -1.1% in GaN [0001] direction and -14.8 % in GaN $[1\bar{1}00]$ direction, respectively.[15] Besides, sapphire has larger TECs than GaN. Therefore, neither the lattice mismatch nor the post-growth cooling is responsible for the formation of

---

[*] The in-plane epitaxial relationship is GaN [0001]// sapphire $[1\bar{1}01]$, and GaN $[1\bar{1}00]$// sapphire $[11\bar{2}0]$. Its detail will be presented in section 3.1.4.

tensile strain in *a*-plane GaN layer. Instead, it is induced by the grain/island coalescence that occurs in the beginning of HT growth and the intrinsic tensile strain generated is inversely proportional to the island diameter.[16] In the case of sample C, the 2D growth mode suggests that the average grain diameter is smaller than that of 3D growth mode (sample B). Consequently, sample C is under larger in-plane tensile strain and is more likely to have cracks.[17] In contrary, samples A and B have no cracks, thanks to lower island density as a result of 3D growth mode.[18] More information about the island coalescence model can be found in the paper of B. W. Sheldon *et al.*[19]

Furthermore, the cracks are aligned perpendicular to GaN [0001] direction, which has also been reported by Haskell *et al.*[8] It may have something to do with the in-plane anisotropy: for example, in the case of epitaxial lateral overgrowth (ELO) of *a*-plane GaN, cracks are often formed at the meeting fronts of +*c* and –*c* planes.[20] For sample C, grain coalescence may occur sooner in *c*-axis due to faster growth rate in that direction, which increases the likelihood of cracking formation perpendicular to [0001] direction. Besides, compressive strain in GaN [0001] direction (-1.1%) is much smaller than that in $[1\bar{1}00]$ direction (-14.8%). As a result, tensile strain accumulated during grain coalescence in [0001] direction may not be partially compensated as much as that in $[1\bar{1}00]$ direction, which also makes cracking perpendicular to [0001] direction more likely to happen.

The influence of the carrier gas composition

During HT growth, it is found that large amount of H_2 is required to obtain smooth surface. Moreover, H_2 is needed even after the growth stops and before cooling down to ~ 950 °C. Otherwise, the original flat surface will soon get rough as inclined facets appear, indicated by the sharp drop of LR signals.

The effects of H_2 as carrier gas for *c*-plane GaN growth have been studied intensively.[21, 22, 23, 24] Their results indicate that the presence of H_2 increases the diffusion length of Ga species by reducing the stability of surface N-atoms, the same effect of using low growth pressure P_g. In other words, without H_2, certain inclined facets are more stable under common growth conditions with high V/III ratio. Actually, *a*-plane has such a narrow growth window that its formation requires both high H_2 flux and low P_g. If H_2 is cut off once the growth stops, the temperature is still high enough that the decomposed Ga species may form other more stable planes under N-rich condition. To prevent that, the supply of H_2 should continue until temperature gets lower.

The influence of V/III ratio

The V/III ratios we mentioned are nominal numbers calculated from the fluxes. The local distributions of V/III ratio depend on the reactor geometry and gas flow rate. For HVPE environment, empirical experience shows that the increase of III-species leads to faster growth rate, but that has no significant impact on GaN surface morphology.

3.1.2 Two-step growth procedure

Two-step growth procedure is widely used for *c*-plane GaN. It begins with the deposition of low temperature (LT) nucleation layer (NL), followed by thermal annealing in H_2 and NH_3 ambient (also called recrystallization period) and then HT growth. *C*-plane GaN grown by two-step procedure exhibits much better material quality than that of single-step, largely due to the thermal annealing of LT NL. It leads to the formation of large 3D hexagonal islands that are well oriented and allow the filtering of dislocations.[25,26] The coalescence of islands at the initial stage of HT growth introduces dislocation bending mechanism since the basal plane is most energetically stable.[27]

This procedure has also been tested for *a*-plane GaN. A LT GaN NL with thickness ~ 30 nm was deposited at T ~ 600 °C and atmospheric pressure, followed by thermal annealing and then HT growth at T ~ 1080 °C and P_g = 100 mbar. To compare with the previous samples A-C, this sample (named as D) has similar layer thickness (~ 3 µm). The entire growth process was recorded by LR and the corresponding spectrum is presented in figure 3.1.5. In addition, AFM scans were performed on samples at different stages: after the NL deposition, the thermal annealing, and HT growth, respectively.

The LT GaN NL has a rms roughness of ~ 1.6 nm on 1×1 μm^2 area, as shown in figure 3.1.5 (a). The average grain size is small, about 50 nm in diameter. For comparison, in the case of *c*-plane, Ga species recombine with N species to form large GaN nuclei (size ~ 500 nm) on NL during the recrystallization period (*i.e.* Ostwald ripening effect). Accordingly, the reflectivity signal drops significantly.[28] However, the formation of 3D islands does not happen when *a*-plane GaN NL is annealed, since the LR signal stays constant. Furthermore, AFM scan reveals that the grain size of post-annealing NL increases to ~ 150 nm and the rms roughness reduces to ~ 1 nm [figure 3.1.5 (b)]. In other words, the NL evolution, which is well suited for high quality *c*-plane GaN, is somehow missing for *a*-plane, as its grain size is much smaller than that of *c*-plane. A possible explanation is that *a*-plane has a higher dangling bond density (*a:* 14.0 nm^{-2} vs *c:* 11.4 nm^{-2}) and demands higher temperature to decompose and reorganize. However, 1080 °C is approximately the upper limit of our HVPE system. The main consequence is that HT growth starts in 2D mode. The signal amplitude dampens after seven oscillation periods (d ~ 1 µm), indicating the occurrence of surface roughening. Normaski optical micrograph shows that the surface morphology looks like sample C: smooth surface with the anisotropy feature along [0001] direction and cracks perpendicular to [0001] direction [figure 3.1.5 (c)]. AFM scan confirms this kind of anisotropy. Some pits are found to decorate the dislocation terminations at the surface [figure 3.1.5 (d)].[9] The rms roughness is about 5 nm for a 5×5 μm^2 area.

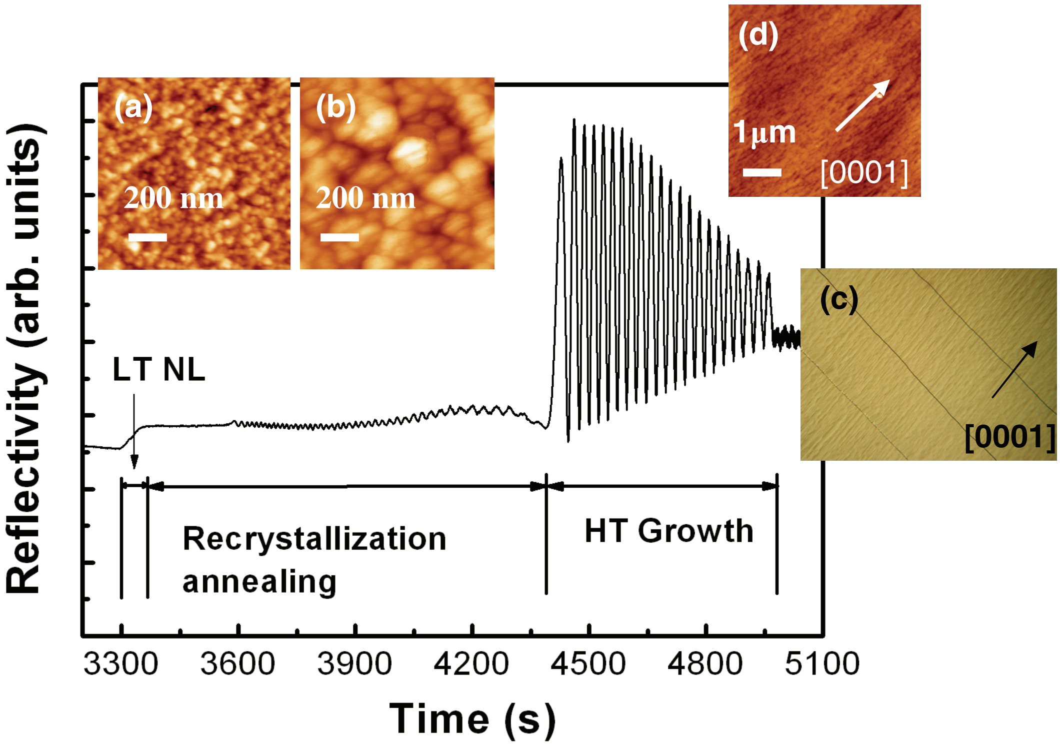

Figure 3.1.5 *in situ* LR signal for *a*-plane GaN using two-step growth method. The insets are AFM images taken after (a) the deposition of NL, (b) the recrystallization annealing, and (c) HT growth, respectively. Their sizes are 1 × 1, 1 × 1, and 5 × 5 μm^2, respectively. The inset (c) is a Normaski optical micrograph (700 × 525 μm^2), which displays the surface morphology of as-grown epilayer.

3.1.3 Pressure-variation growth procedure

From the previous two sections, it is known that high P_g results in 3D growth (rough surface), whereas low P_g leads to 2D (relatively smooth surface) and often induces cracks. Besides, the introduction of a LT GaN NL fails to markedly improve the material quality, because there is a lack of effective NL evolution, which serves as an efficient defect reduction mechanism on *c*-plane. To intentionally introduce such process, a so-called pressure-variation (P-V) procedure has been developed, based on the fact that the growth mode is sensitive to pressure.

P-V growth resembles the one-step, except that P_g changes. The process flow chart is depicted in figure 3.1.6. After a nitridation of sapphire surface for ~ 10 min with T > 1000 °C, the growth starts at P_g = 400 mbar for a short period t_1 in 3D growth mode. Then, P_g is decreased to ~ 100 mbar to promote lateral growth and island coalescence. Other growth parameters are the same as those of single- and two-step procedures. The layer thickness is ~ 3 μm. Three different time periods (0.5/1/2 min) were applied to optimize t_1, because the size of crystal islands increases with time.

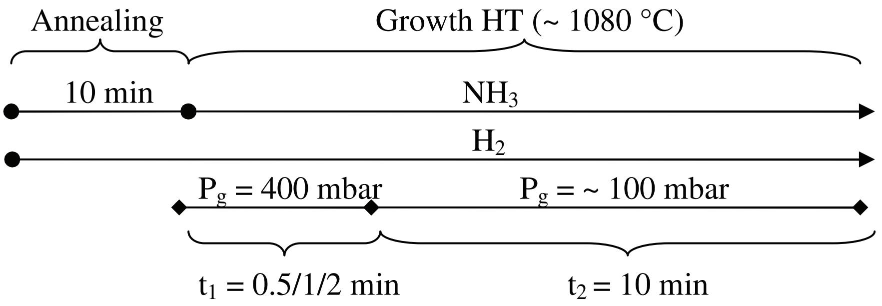

Figure 3.1.6 Schematic flow chart of the P-V growth

The corresponding *in situ* LR signals are presented in figure 3.1.7. For samples with t_l = 1 (blue) and 2 (red) minutes, the signal intensities dropped sharply right after the growth began and stabilized at near-zero for a few minutes, indicating the initial 3D growth mode. For sample with t_l = 0.5 min (black), the signal only dropped slightly. Then, it took about 1 min for P_g to decrease from 400 to 100 mbar. The reflectivity signals bounced back accordingly and oscillations were clearly observed from samples with t_l = 0.5 and 1 min, as a results of 2D growth mode. This is not the case for the sample with t_l = 2 min. The oscillations damped with the increase of the layer thickness, due to surface roughening. Judged from the oscillation envelopes, the surface is less rough for the sample of t_l = 0.5 min than that of t_l = 1 min, since the LR signal of the latter is lower.

The Nomarski optical micrograph insets reveal the surface anisotropy along *c*-axis direction. It seems that shorter t_l results in smoother surface. This observation is confirmed by AFM scan (5 × 5 μm^2), where the rms roughnesses are 4.4, 3.2, and 2.8 nm for t_l= 2, 1, and 0.5 min, respectively. Besides, sometimes there are cracks in the sample of t_l = 0.5 min, though not shown here. The cracks are also aligned perpendicular to [0001] direction. Hence, a compromise between the surface smoothness and the suppression of cracks leads to the optimized t_l = 1 min.

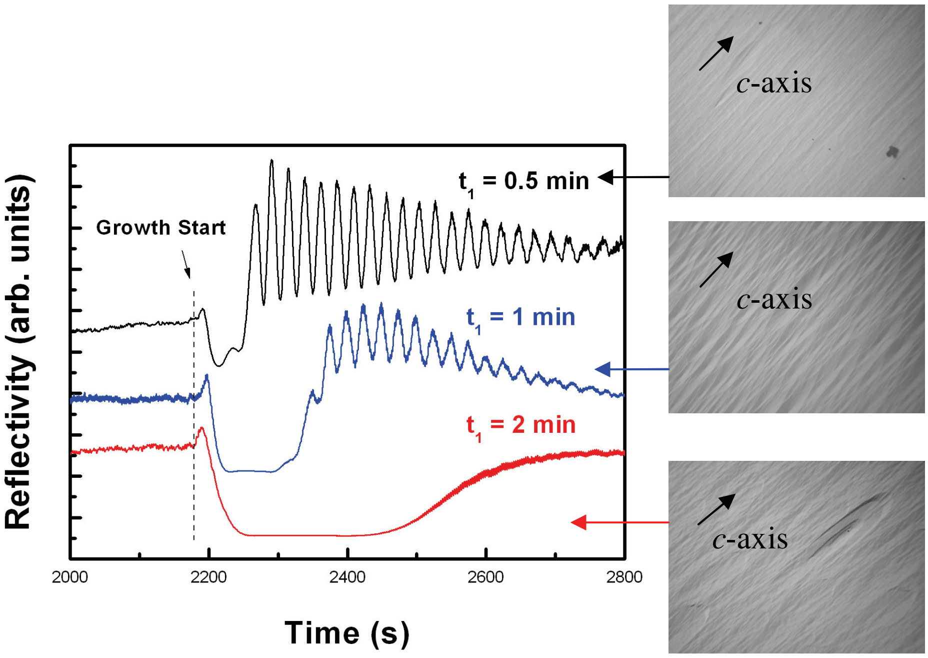

Figure 3.1.7 *in situ* LR signals recorded for P-V growth procedures with $t_1 = 2$ (red), 1 (blue), and 0.5 min (black). The optical micrographs (700 × 525 μm^2) reveal the surface morphology of the as-grown samples.

3.1.4 Structural and Optical properties

X-ray diffraction (XRD)

The crystal orientation of the as-grown GaN epilayers is measured by on-axis $\omega-2\theta$ scan [figure 3.1.8 (a)]. Only GaN $(11\bar{2}0)$ and sapphire $(2\bar{2}04)$ planes are observed. Thus, the GaN epilayer is of single orientation. The in-plane epitaxial relationship is measured by off-axis ϕ scans. Peaks of GaN $(10\bar{1}0)$, GaN $(10\bar{1}1)$ and sapphire $(2\bar{1}\bar{1}0)$ are found [figure 3.1.8 (b)]. The correlations between the ϕ positions of these peaks determine the following relationship: GaN [0001]// sapphire $[\bar{1}101]$, and GaN $[1\bar{1}00]$ // sapphire $[11\bar{2}0]$. This is consistent with other reports using various growth techniques.[8, 9]

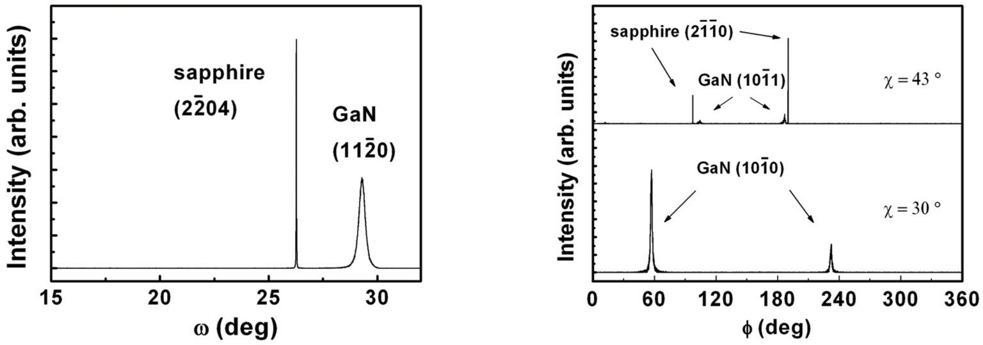

Figure 3.1.8 For GaN epilayers grown on *r*-sapphire, XRD (a) on-axis $\omega-2\theta$ scan and (b) off-axis ϕ scans have been performed to identify the crystal orientation and in-plane epitaxial relationship, respectively.

The FWHMs of symmetric ω scan rocking curves were measured to assess the structural quality. Figure 3.1.9 (a) is a diagram where the FWHM values are a function of the azimuth angles for samples A-D. Here, the azimuth 0° is defined as the projection of the incident X-ray beam parallel to [0001] direction, and azimuth ± 90° are parallel to $[1\bar{1}00]$ direction. It appears that the growth pressure has an effect on the anisotropy behavior of the FWHMs values, which exhibit a "V" or "Λ" shape. For example, sample A (P_g = 400 mbar) reaches a maximum value of 0.65° in the [0001] direction, where sample C (P_g = 100 mbar) reaches a minimum of 0.25°. On the other hand, in the $[1\bar{1}00]$ direction, sample A reaches a minimum of 0.22°, and sample C reaches a maximum of 0.56°. Sample D (two-step) follows the same trend as sample C, as they were grown at the same low pressure (100 mbar). Namely, its FWHM minimum is 0.28° in the [0001] direction and its maximum is 0.69° in the $[1\bar{1}00]$ direction. Interestingly, this kind of anisotropy is much less pronounced for sample B (P_g = 200 mbar), as its FWHM roughly holds around 0.37°.

Such measurement has also been applied to P-V sample with t_1 = 1 min [figure 3.1.9 (b)]. Sample A and C are presented together as references. In comparison, the FWHM values of P-V sample also exhibit a "V" trend. The trend follows that of sample C: its FWHM reaches the minimum of 0.20° in the [0001] direction, and a maximum of 0.35° in the $[1\bar{1}00]$ direction. Even though these numbers are much larger than those of planar *c*-plane GaN, they are smaller than those of sample C by 20 – 50 %, depending on the azimuth angles. This indicates certain moderate improvement.

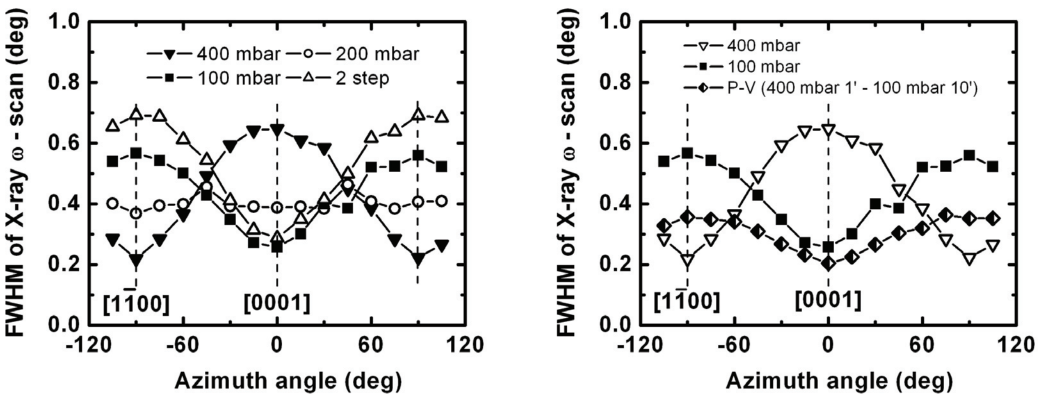

Figure 3.1.9 FWHM of X-ray ω scans for (a) sample A (solid triangle), B (void circle), C (solid square) and D (void triangle) as a function of azimuth angle. Azimuth angle 0° is defined as X-ray parallel to the [0001] direction; (b) P-V sample with t_1 = 1 min (spade) as a function of azimuth angles. Sample A (triangle) and C (square) are references.

Such "V" or "Λ" shape for FWHMs of heteroepitaxial *a*-plane GaN layers has been reported by other groups using HVPE and MOVPE.[10, 29, 30] It has nothing to do with GaN crystal structure at all, since T. Paskova *et al.* have reported that high-quality bulk *a*-plane GaN layers sliced from boules do not have such features.[31] Instead, it is due to the heteroepitaxy procedure.

This problem has been investigated by some groups. For example, Roder *et al.* have ascribed this phenomenon to the wafer-bending factor.[32] However, it is not applicable to thin epilayers described here.[†] Another possibility is that heteroepitaxial growth anisotropy leads to anisotropic distribution of defects. It is known that the specific defect geometries in the epilayer only distort certain crystallographic planes.[33] H. Wang *et al.*[10] and T. Paskova *et al.*[31] have reported rocking curves of thin *a*-plane GaN layers with “V” shape, just like those of sample C and D. They ascribe it to the anisotropic mosaic broadening, based on reciprocal lattice maps. Even so, that explanation cannot account for the trends of sample A (“Λ” shape) and B (nearly flat), which have only been reported for much thicker epilayers ($d > 15$ μm).[32] Very recently, Moram *et al.* has reported a systematic investigation. They argue that the anisotropic broadening arises from a complicated superposition of several factors, including defects (both SFs and TDs), surface roughness, and wafer bending.[30] Particularly, they report that two samples with very similar dislocation and SF densities but quite different surface morphologies in terms of rms roughness have different ω-scan peak widths patterns. They suggest that surface-related anisotropic ω-scan broadening could potentially arise due to the relief of in-plane strain associated with surface roughness.[30] In our case, the effect of wafer bending is negligible, as discussed in the following. Instead, a complex interplay between surface roughness and defects may be invoked.

Discussion of wafer bending and its effect on X-ray rocking curve broadening

Heteroepitaxial systems consisting of a stressed thin layer on a foreign substrate reduce the total strain energy by wafer bending, which is an effective elastic strain relaxation mechanism. During the post-growth cooling step, the wafer bends because the TECs of GaN are smaller than those of sapphire. As a result, GaN thin layer at room temperature is usually under compressive stress, as shown in figure 3.1.10. Here, h_F and h_S are the thicknesses of the film and the substrate, respectively. t is the distance between the neutral axis (center) to the interface of GaN/sapphire.

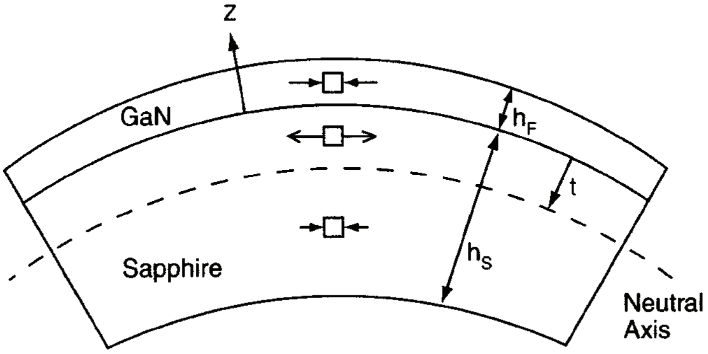

Figure 3.1.10 Schematic diagram of the wafer bending induced by the cooling, after E. V. Etzkorn *et al.*[34]

According to the model developed by E. V. Etzkorn et al.,[34] the radius of curvature ***R*** is defined as

$$R = \frac{1}{\Delta\alpha\Delta T}\left[\frac{h_S^2}{6(h_S - 2t)} + \frac{h_F^2}{6(h_F + 2t)} + \frac{1}{2}(h_S + h_F)\right] \tag{3.1}$$

$\Delta\alpha$ is the difference of TECs between GaN and sapphire, t the distance from the interface to the neutral axis, and ΔT the difference between growth and room temperature. The TEC data are taken from Roder *et al.*[32]

[†] The reason will be discussed in the next page.

A few *a*-plane GaN samples without cracks have been characterized to study the curvature (1/***R***) (figure 3.1.11). The curvatures were measured in [0001] and $[1\bar{1}00]$ directions, respectively, by recording X-ray rocking curves of the $(11\bar{2}0)$ reflections and evaluating the peak shifts. The growth temperatures vary from 1060 to 1080 °C and the sapphire substrate thicknesses also change from sample to sample.

The curvature in both directions increases steadily with the GaN layer thickness, and it is larger in [0001] direction than in $[1\bar{1}00]$ direction. The calculated and measured data roughly match, though the discrepancies enlarge with the increase of the layer thickness. It can be contributed to the fact that the model is designed for *c*-GaN with isotropic in-plane stress, whereas in *a*-plane GaN the stress is anisotropic. Besides, the distribution of defects, which partially release the stress, is also anisotropic.

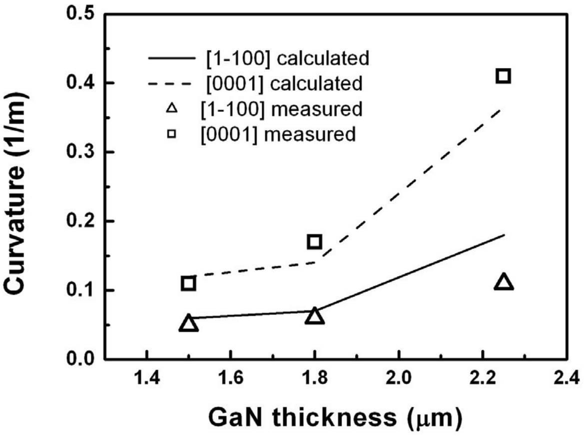

Figure 3.1.11 Wafer curvature in GaN [0001] and $[1\bar{1}00]$ directions as a function of the GaN layer thickness.

It is well known that wafer bending broadens the X-ray rocking curve. According to Roder *et al.*,[32] the broadening $\Delta\omega_b$ of a symmetric reflection due to the bending is given by

$$\Delta\omega_b = \frac{bk}{\sin\omega} \tag{3.2}$$

Here, *b* is the width of incident beam, *ω* is the incidence angle relative to the sample surface, and *k* is the curvature. Using *b* = 1 mm, *ω* = 28.9°, and *k* = 0.4 for a layer with *d* ~ 2.2 µm, the calculated $\Delta\omega_b = 0.048°$ (~ 172 arcsec).

The total width $\Delta\omega$ of the rocking curve is given by a convolution of the broadening $\Delta\omega_b$ from bending and the broadening $\Delta\omega_d$ from crystal defects such as dislocations:

$$\Delta\omega = \sqrt{\Delta\omega_b^2 + \Delta\omega_d^2} \tag{3.3}$$

For *a*-plane GaN grown at low pressure, the measured $\Delta\omega$ is ~ 0.25° and ~ 0.6° in [0001] and $[1\bar{1}00]$ directions, respectively. Thus, it is reasonable to say that the broadening induced by the wafer bending contributes a negligible part (< 2 %) to the total width of the rocking curve. Thus, my argument is that wafer bending does not account for the anisotropy of FWHM X-ray rocking curve. Instead, it is due to a complex interplay of defects and surface roughness, as described in the previous section. This conclusion is not in agreement with that of Roder *et al.*[32] In their case, the *a*-plane GaN layers are much thicker (7-65 µm) and consequently the wafer-bending-induced broadening is much more significant (*e.g.* $\Delta\omega_b =$ 0.6° for layer of 65-µm-thick).

Transmission electron microscopy (TEM)[‡]

A-plane GaN samples with growth procedure similar to that of sample C have been characterized by TEM. The selected area electron diffraction (SAED) patterns of the *a*-plane GaN/*r*-plane sapphire interface reveal the in-plane epitaxial relationship, as shown in figure 3.1.12 (a). GaN $[1\bar{1}00]$ direction (red circles) is parallel to sapphire $[11\bar{2}0]$ direction (grey circles). This is in agreement with XRD results.

Besides, there is a local misorientation in the SAED patterns, as *a*-plane GaN was tilted 6 ± 0.5° off *r*-plane sapphire in the growth direction. The high resolution TEM image of the interface confirms this observation [figure 3.1.12 (b)], which was taken in sapphire $[11\bar{2}0]$ zone axis. This is probably induced by the sapphire surface which becomes rough after nitridation at HT (1000 – 1080 °C), as shown in figure 3.1.2.

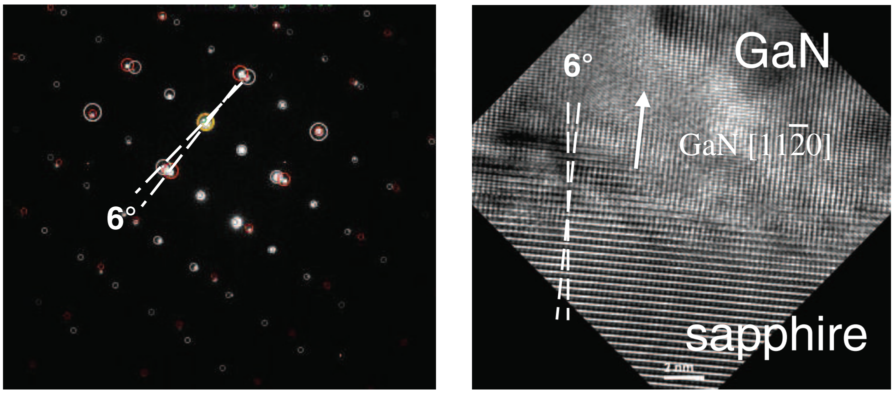

(a) (b)

Figure 3.1.12 (a) The SAED patterns of *a*-plane GaN and *r*-plane sapphire, where the red circles represent GaN $[1\bar{1}00]$ zone axis, and the grey ones sapphire $[11\bar{2}0]$ zone axis; (b) TEM picture of *a*-plane GaN/*r*-plane sapphire interface along sapphire $[11\bar{2}0]$ zone axis. Dash lines show that GaN is tilted about 6° from sapphire in the growth direction. (By courtesy of Yadira Arroyo at CIME EPFL)

In theory, crystal misorientation as large as 6° should be easily detected by XRD rocking curve measurement. However, it has not been found in our case. One tentative explanation could be that the rocking curve FWHM is too broad (~ 600 arcsec) to discriminate misorientation from other broadening factors like defects. However, we believe this is not the main reason. Recall that the average grain size of GaN is usually in the range of micrometers.[17] Coincidentally, the probe area for SAED in figure 3.1.12 is also about a few micrometers. Therefore, a possible explanation is that the observation in figure 3.1.12 is related to local grain misorientation, *i.e.* mosaic tilt. It does not reproduce the XRD trends because of the lack of averaging effect.

[‡] The TEM characterizations were performed by Yadira Arroyo at CIME, EPFL.

TEM characterizations have also revealed that BSFs with density of 1×10^6 cm^{-1} are formed at the interface and propagate vertically up to the top surface (figure 3.1.13). Two types of intrinsic BSFs have been identified: (a) I_1 BSFs, terminated by the Frank-Shockley partial dislocations, have the Burgers vector $\vec{b} = \frac{1}{6} < 2\bar{2}03 >$; and (b) I_2 BSFs, terminated by the Shockley partial dislocations, have the Burgers vector $\vec{b} = \frac{1}{3} < 1\bar{1}00 >$. Both BSFs are aligned parallel to GaN $[1\bar{1}00]$ direction.

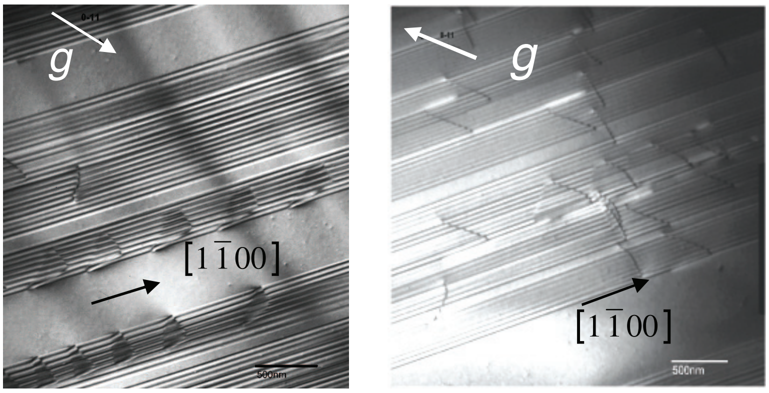

(a) (b)

Figure 3.1.13 TEM images of BSFs in *a*-plane GaN films (a) dark field image ($g = 0\bar{1}11$) of type I_1 and (b) bright field image ($g = 0\bar{1}11$) of type I_2. (By courtesy of Yadira Arroyo at CIME EPFL)

Prismatic stacking faults (PSFs) have been observed as well [figure 3.1.14 (a)]. They are located in between two adjacent I_1 BSFs [figure 3.1.14 (b)], tilted 60° off the growth plane.[35]

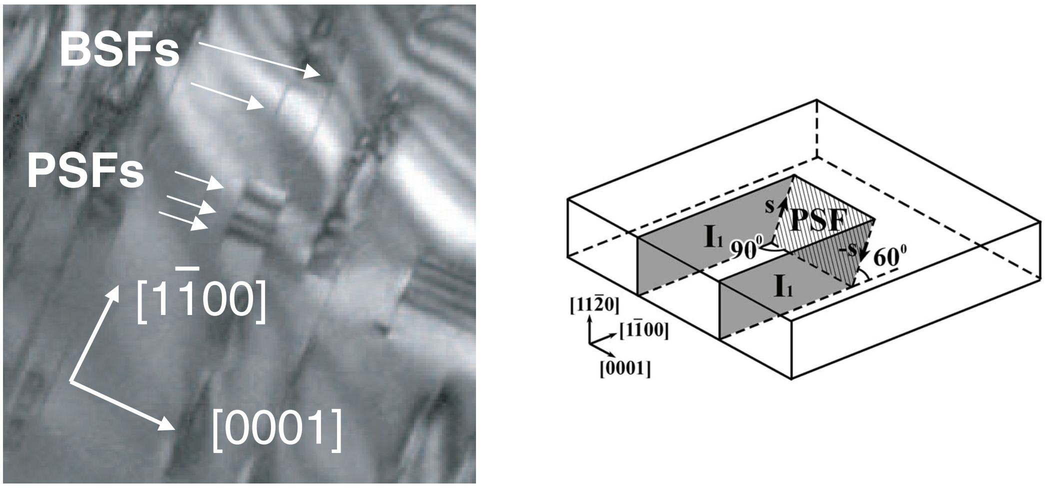

(a) (b)

Figure 3.1.14 (a) TEM image of the top view, where the BSFs and PSFs are aligned to $[1\bar{1}00]$ and [0001] directions, respectively. (By courtesy of Yadira Arroyo at CIME EPFL) (b) Schematic representation of the termination of two BSFs by one PSF, s and –s represent $\frac{1}{6}[10\bar{1}0]$ and $\frac{1}{6}[\bar{1}010]$ stair-rod dislocations, after Ref.35.

The presence of BSFs is a characteristic feature of non-polar GaN heteroepitaxy on various substrates, since their formation energies are small (in the order of 10 meV/unit cell area)[36]. Although high-density BSFs have also been reported in polar *c*-plane near the layer/substrate interface,[37] they can be effectively suppressed by growing a thicker layer, since they are aligned perpendicular to the growth direction (*c*-axis) and do not penetrate upwards. In the case of non-polar layers, however, the BSFs are parallel to the growth direction and propagate to the top surface, so unfortunately the density does not decrease with the increase of epilayer thickness.

In addition to SFs, threading dislocations (TDs) are also common defects in *a*-plane GaN epilayers. They are of edge, screw, and mixed types with Burgers vector $\vec{b}$ = <0001>, $\frac{1}{3}<11\bar{2}0>$, and $\frac{1}{3}<11\bar{2}3>$, respectively. The TD density is high, about 10^{10} cm^{-2}. More details will be presented in the section 3.2.2.

Photoluminescence (PL)

LT (T = 8K) PL spectra, measured on samples B–D at an excitation power density of 40 W/cm^2, are displayed in figure 3.1.15 (a). PL spectrum measured on sample A exhibits only a yellow luminescence peak and is consequently not presented here. The emission peak at 3.42 eV (labeled D1 as in the paper of P. P. Paskov *et al.*[38]) observed on samples B – D is related to excitons bound to type-I_1 BSFs, [38] while the emission peak at 3.485 (sample B), 3.483 (sample C) and 3.479 eV (sample D) is related to near band-edge (NBE) recombination. For sample B, the NBE emission appears as a shoulder of the BSF-related emission peak with a FWHM of about 25 meV. For samples C and D, the NBE emission is clearly separated from the BSF emission peak with a FWHM of about 20 meV. In the latter case, the NBE emission line is still too broad to reveal the separate contributions of free excitons and that of excitons bound to a shallow donor. The larger FWHM of the NBE emission of sample B could be ascribed to a higher residual doping. This is supported by the observation of an intense emission peak at 3.277 eV in the spectrum of sample B, a transition energy close to the donor–acceptor pair (DAP) transitions usually observed for *c*-plane GaN. Note that the contribution of the D2 peak (samples C and D) usually centered at 3.29–3.32 eV is much less pronounced than for MOVPE-grown *a*-plane GaN[38]. In accordance with the surface morphology, it appears that GaN samples grown at lower pressure, namely samples C and D, exhibit a better quality than sample B. This is supported by a strong suppression of the DAP emission peak as well as a narrower FWHM of the NBE emission.

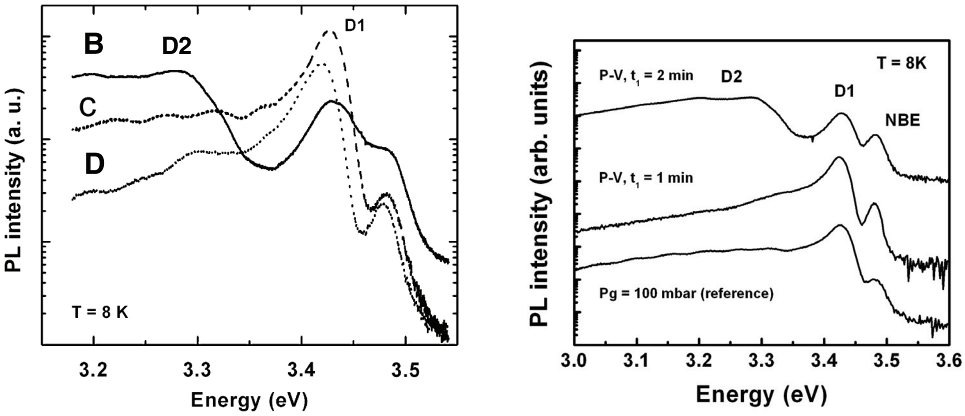

Figure 3.1.15 Low-temperature PL spectra measured on (a) samples B (solid line), C (dashed line), and D (dotted line); (b) P-V samples with t_l = 1 and 2 min, respectively. Sample C is used as a reference.

LT (T = 8K) PL spectra were also measured on the P-V samples with t_l = 1 and 2 min, plus the sample C (P_g = 100 mbar) as a reference [figure 3.1.15 (b)]. The emission peak at 3.42 eV as D1 in Ref.38, related to excitons bound to BSFs, still dominates the spectra for all the three samples. NBE emission peaks also appear at ~ 3.48 eV. P-V samples demonstrate a higher PL intensity ratio between D1 and NBE than the reference sample C. P-V (t_l = 2 min) is characterized by a high D2 peak, probably due to a higher residual doping since it was grown at high pressure for a longer time. The reduction of DAP emission peak in P-V (t_l = 1 min) sample is observed. Its NBE peak has a FWHM of 17 meV.

Judged from the PL and XRD data, P-V sample with t_l = 1 min exhibits moderate improvement in structural and optical properties, probably because large 3D crystal islands are promoted in the initial stage of HT growth. Unfortunately, such improvement is over-counteracted by the fact that dislocations fail to bend due to energy preference and BSFs propagate parallel to the growth direction.

3.1.5 Summary

Three growth recipes have been developed for heteroepitaxy of *a*-plane GaN on *r*-plane sapphire by HVPE: one-step, two-step and P-V. By comparing the characterization results, it seems that P-V samples have slightly better material quality than the other two.

Here are some characteristic features for *a*-plane GaN epilayers grown on *a*-sapphire:
(1) Strong in-plane growth anisotropy in GaN [0001] direction;

(2) pressure-dependence in terms of surface morphology;
(3) H_2 gas is required during and even after the growth;
(4) High-density BSFs are aligned parallel to GaN $[1\bar{1}00]$ direction and they propagate to the top surface;
(5) The standard two-step growth procedure does not significantly improve the material quality, due to the lack of suitable NL evolution (*e.g.* the formation of 3D crystal islands);
(6) Compared to the other two procedures, P-V growth improves the material quality moderately.

Overall, the material quality (*i.e.* surface roughness, defect density, and optical properties) of planar *a*-plane GaN epilayers grown by HVPE is significantly inferior to that of planar *c*-plane, since the defect filter mechanism that works for *c*-plane does not apply for *a*-plane. To improve the quality, epitaxial lateral overgrowth technique appears to be an attractive solution.

3.2 Epitaxy lateral overgrowth of *a*-plane GaN

ELO technique had not been applied to non-polar orientations in our group before this work, so an initial study of mask patterns and growth parameters were conducted in order to optimize the growth procedure, as discussed in section 3.2.1. After that, fully-coalesced ELO templates were prepared and characterized, as described in section 3.2.2.

3.2.1 Preliminary investigations

The influence of mask patterns

In this preliminary study, ELO GaN layers were directly grown on patterned *r*-plane sapphire substrates. To understand the relationship between the window pattern orientations and the growth anisotropy, 'wagon-wheel' pattern and hexagonal pattern were used. The 'wagon-wheel' pattern consists of nonparallel stripes aligned 5° shift from each other, with size of width 10 μm and length 500 μm. The diagonal of the hexagonal pattern is about 9 μm. SEM top-view images (figure 3.2.1) show the ELO morphology after 10 min growth at $P_g = 100$ mbar and T ~ 1080 °C.

On the 'wagon-pattern', the ELO morphologies are not uniform and change with the stripe orientations. The layer thickness is about 3.5 μm. Two regions are of interest. The first one is around GaN *c*-axis [figure 3.2.1 (a)], where lateral overgrowth rate is relatively small. Particularly, for the stripe aligned along *c*-axis, its lateral overgrowth is negligible, meaning that *m*-plane grows slowly. Besides, its top plane is not flat, formed by inclined facets $\{10\bar{1}0\}$. The second region is around the GaN *m*-axis [figure 3.2.1 (b)], where the stripe aligned along *m*-axis has a large lateral overgrowth, indicating faster growth for *c*-plane. Besides, the top surface is flat. In general, fast lateral growth rate or larger ELO ratio (defined as lateral width/layer thickness) is preferred to expedite the overgrowth coalescence. The maximum lateral growth rate is achieved in the stripes aligned ~ ±30° off *m*-axis, or equivalently ~ ±60° off *c*-axis. However, their lateral growth fronts consist of inclined sidewalls that could be problematic for ELO coalescence. Furthermore, TEM characterizations in section 3.1.4 reveal that BSFs are aligned perpendicular to *c*-axis, so the stripe patterns should be aligned perpendicular to *c*-axis, *i.e.* along *m*-axis, in order to avoid BSFs propagating into the mask areas.

GaN crystals grown on hexagonal patterns are of trapezium structure, as shown in the figure 3.2.1 (c). They are bounded by planes of $(000\bar{1})$ and $\{1\bar{1}01\}$. Both experimental results[5] and theoretical predictions[39] have demonstrated that crystal planes such as $\{11\bar{2}2\}$, $\{1\bar{1}01\}$ and $(000\bar{1})$ are the slow-growing ones for GaN.

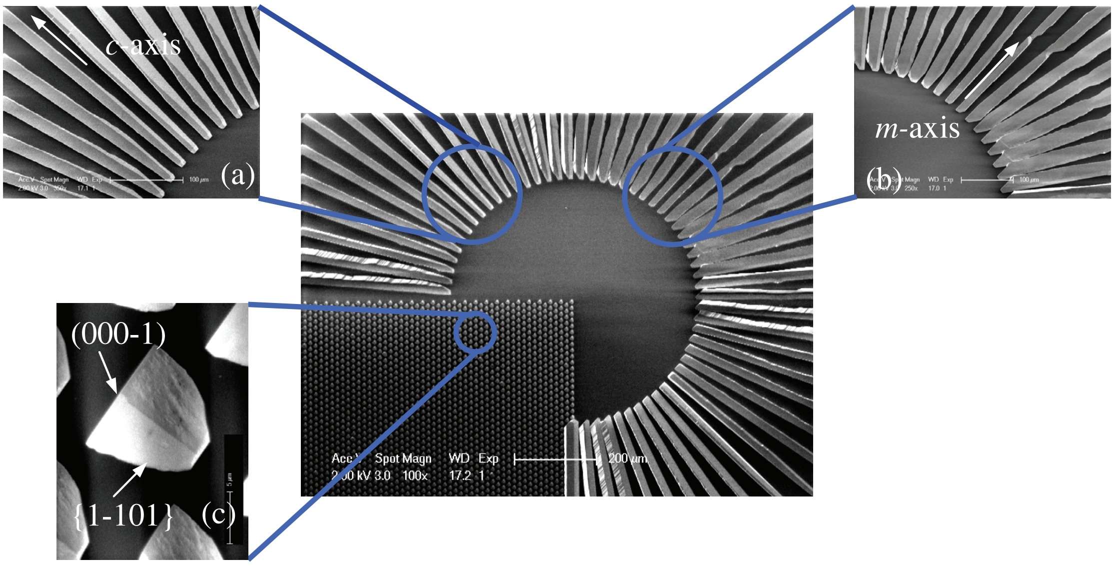

Figure 3.2.1 SEM top-view images of HVPE *a*-plane GaN ELO on “wagon-wheel” and hexagonal patterns. Insets (a) and (b) are enlarged views where stripes are aligned near GaN *c*- and *m*-axis, respectively. Inset (c) is an enlarged view of the hexagonal pattern.

The influence of growth parameters

A series of samples has been grown under different conditions, as listed in table 3.2.1. The masks are long stripes with windows (width 5 µm) and masks (width 10 µm). The stripes are aligned along GaN *m*-axis, and the mask is SiO_2 (d ~ 200 nm) deposited by PECVD. The patterns were prepared by conventional photolithography. Note that ELO samples A – E are not fully coalesced.

ELO Samples No.	A (reference)	B	C	D	E
Temperature (°C)	1090	1060	1030	1090	1090
H_2 (sccm)	3000	3000	3000	1500	3000
P_g (mbar)	100	100	100	100	200

Table 3.2.1 Various growth conditions applied to *a*-plane GaN ELO samples. Underlined parameters are different from those of reference sample A.

The SEM cross-section images of all these five samples are shown in figure 3.2.2. Their vertical facets are (0001) and (000$\bar{1}$) planes, also referred to as Ga- and N- faces, respectively. The lateral growth rate of Ga- face is much higher than that of N- face.[40] In average, growth rate of Ga-face is about 5 times that of N-face. The top surfaces are horizontal *a*-plane and/or inclined {$11\bar{2}2$} planes.

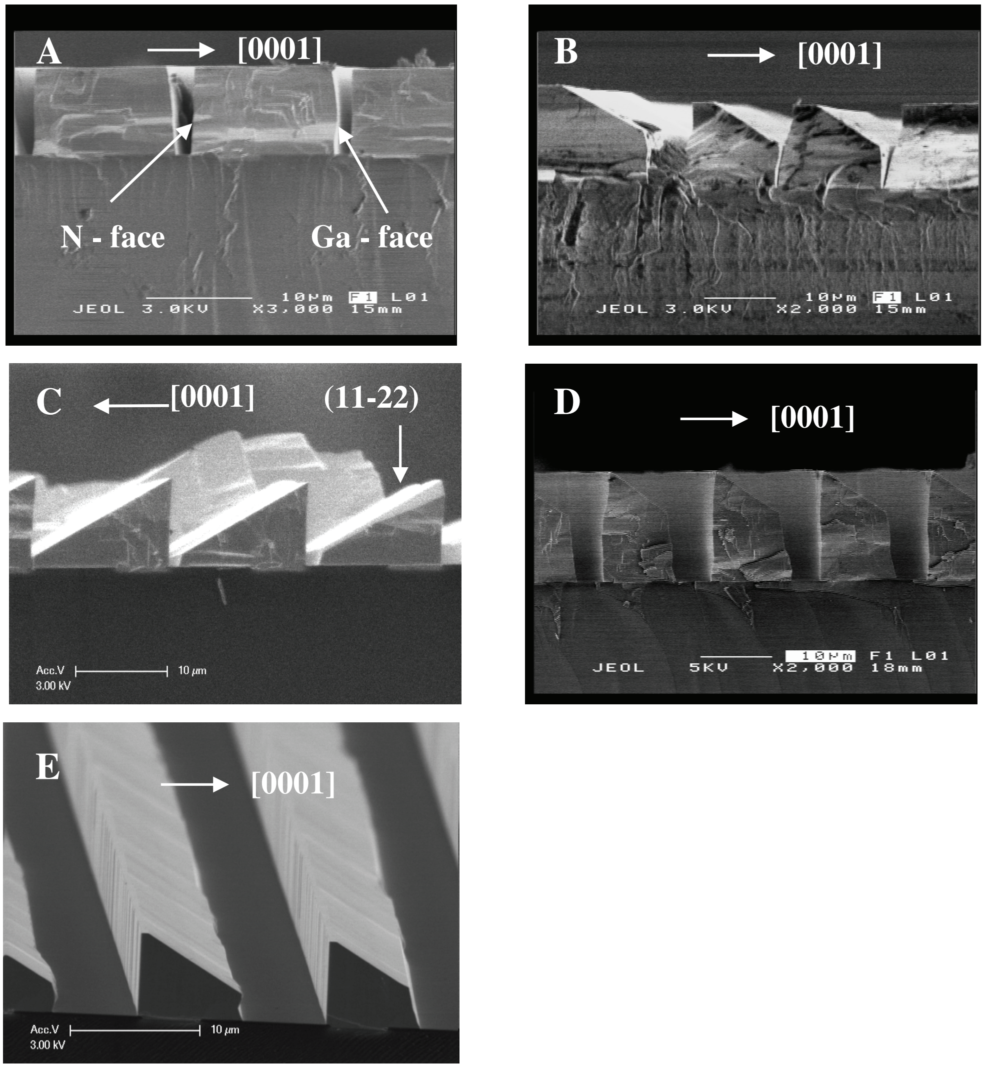

Figure 3.2.2 SEM cross-section images of samples A-E as listed in table 3.2.1. (By courtesy of Yadira Arroyo CIME EPFL for samples A, B, and D)

Sample A serves as a reference and its growth conditions are similar to those applicable to the planar templates: high temperature, high H_2 flux and low pressure. Its top surface is of $(11\bar{2}0)$ *a*-plane. A comparison of these five samples reveals that the top surface (*i.e. a*-plane) is quite sensitive to the growth parameters, as schematically depicted in figure 3.2.3:

(a) When the substrate temperature is reduced to 1060 °C (sample B), the top is made of both flat $(11\bar{2}0)$ and inclined $\{11\bar{2}2\}$ planes. Further decrease to T = 1030 °C (sample C) results in the disappearance of *a*-plane.

(b) When H_2 flux is reduced by half to 1500 sccm (sample D), the top is $\{11\bar{2}2\}$ plane instead of *a*-plane.

(c) When P_g doubles to 200 mbar (sample E), the top is $\{11\bar{2}2\}$ plane.

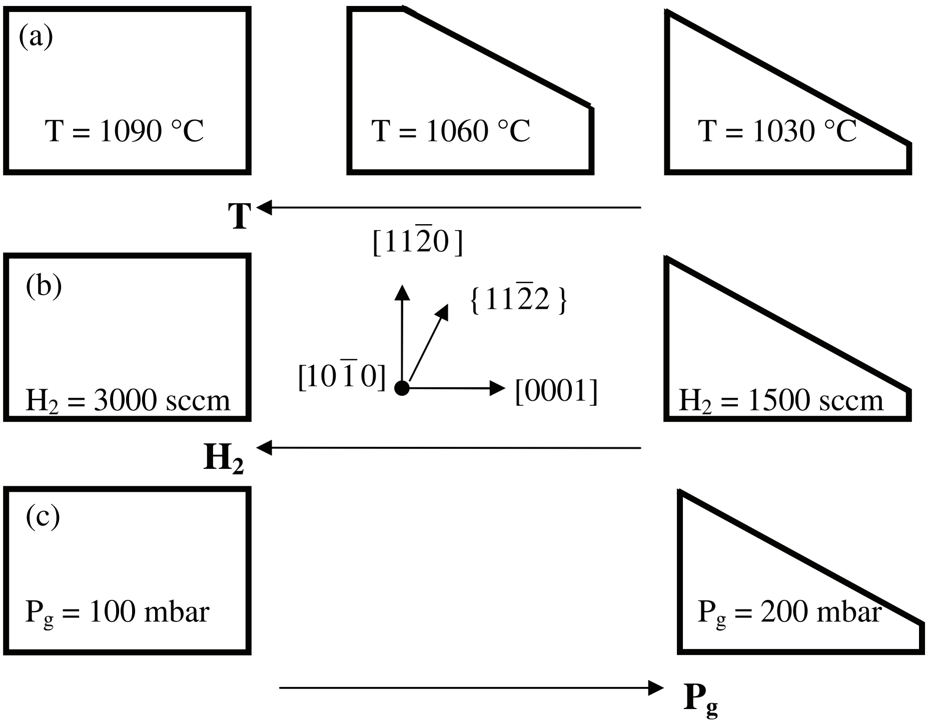

Figure 3.2.3 Schematic diagram of ELO *a*-plane layers under different growth parameters: (a) temperature, (b) H_2 flux, and (c) pressure.

These observations are compatible to those found in section 3.1, *i.e.* high temperature, high H_2 flow rate, and low pressure are required to obtain *a*-plane. More comprehensive investigations of GaN ELO growth including things like fill factor (ratio between mask and window) and mask materials have not been pursued in this thesis, due to the lack of time.

Structural characterization by cathodoluminescence (CL)[§]

An ELO sample has been characterized by low temperature (T = 8K) CL. Its morphology is similar to that of sample B, in the sense that the top is made of two planes: $(11\bar{2}0)$ and $\{11\bar{2}2\}$.

The top-view monochromatic CL maps show that there are two high energy lines at 3.471 and 3.417 eV (figure 3.2.4). The former is related to the recombination of donor-bound excitons; the latter arises from the recombination of excitons bound to the type I_1 BSFs. Details can be found in the paper of P. Corfdir *et al.*[41] Here are some highlights:

(1) There are more intense emission related to BSFs in the –*c* mask wing than in the +*c* side, confirming the observation of higher BSF density in the –*c* direction.[42]

(2) Bright lines in figure 3.2.4 (a) are BSFs in the +*c* wing. They accumulate in bundles, marked by the white arrows. Dark lines in figure 3.2.4 (b) are the anti-correlation of those bright lines.

(3) PSFs appear as dark lines in both maps. They are 60 ° off the growth plane. They intersect with the inclined $\{11\bar{2}2\}$ planes, leaving traces marked by the black arrows.

[§] The CL measurements have been performed by P. Corfdir at IOEQ EPFL.

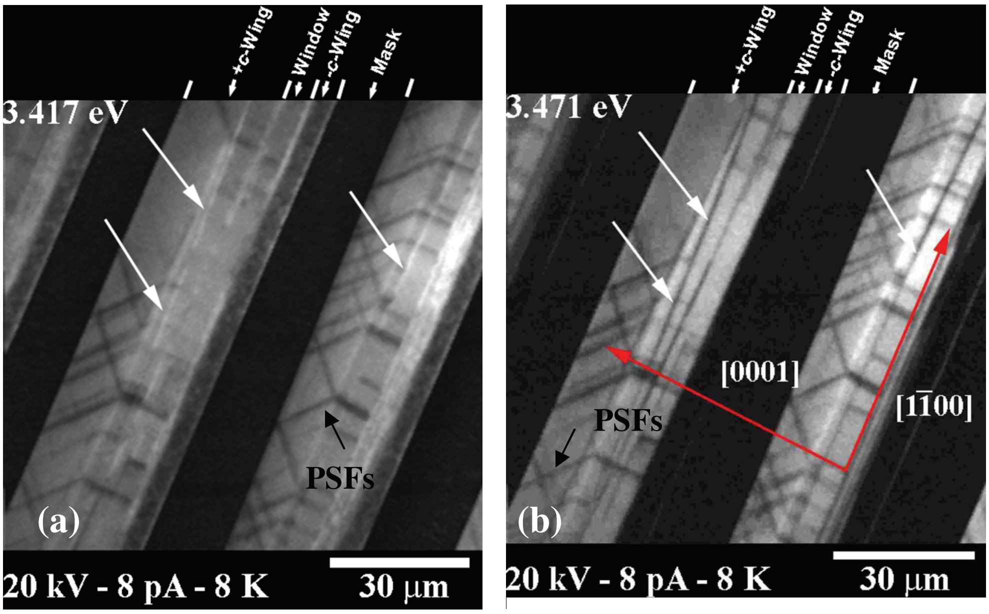

Figure 3.2.4 (a) and (b) are top-view CL maps of ELO *a*-plane GaN taken at the recombination energy of type I_1 BSF-bound excitons (3.417 eV) and neutral donor-bound excitons (3.471 eV), respectively. White arrows point out BSFs and illustrate the anti-correlation between the emissions at 3.417 and 3.471 eV. Dark arrows are nonradiative traps related to the PSFs, after Ref.41. (By courtesy of P. Corfdir at LOEQ EPFL)

Overall, CL data indicate that the material quality in +*c* wing is much improved compared to the window and –*c* wing, though there are still some BSFs and PSFs in +*c* wing.

3.2.2 Coalesced ELO layer – results and discussions

Surface morphology

A fully-coalesced ELO layer has been grown under the same conditions as sample A. The cross-section SEM image is presented in figure 3.2.5 (a). The mask pattern is window of 5 µm + mask of 10 µm. The layer thickness is about 18 µm. Some voids, marked by the circle, are observed at the interface where the lateral +*c* and -*c* fronts meet.[43]

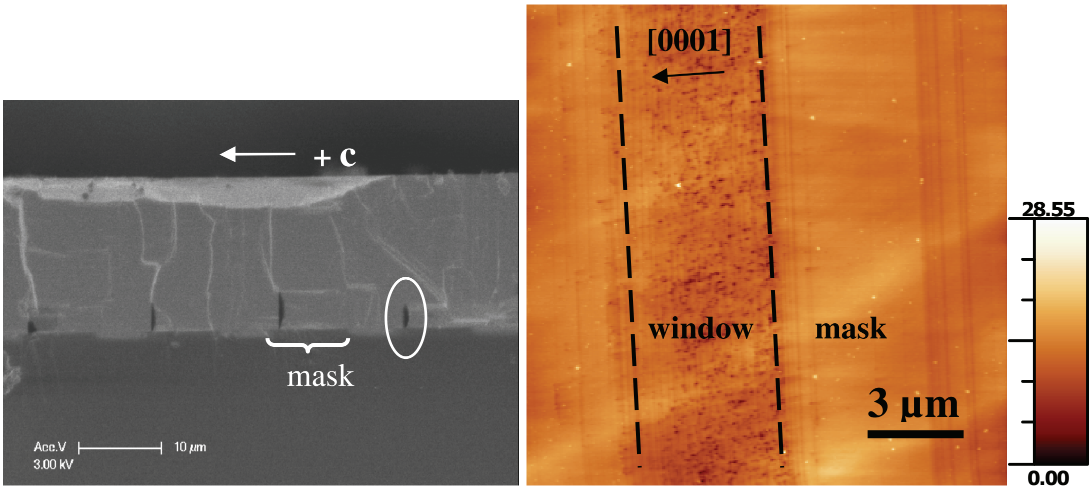

Figure 3.2.5 A fully-coalesced ELO sample (a) SEM cross-section image and (b) AFM of 15×15 µm^2 scan on the top surface. The circle in (a) indicates the position of voids. The dash guide lines in (b) discriminate between the mask and window areas.

The top surface is characterized by AFM on a 15×15 μm^2 area [figure 3.2.5 (b)]. The surface of the window area is decorated with pits of high density, where rms roughness is ~ 1.2 nm on a 5×5 μm^2 scan area. This number is comparable with that of thick HVPE layer reported by B. A. Haskell *et al.*[8] On the mask areas, rms roughness turns out to be much lower (0.4 nm on a 5×5 μm^2 scan area), indicating improvement of surface smoothness. Compared to the "step" morphology of *c*- and *m*-plane, overgrown *a*-plane GaN surface is basically featureless, which has also been reported by other groups.[8, 44, 45]

XRD

Two XRD ω-scans have been performed with X-ray parallel to *c*- and *m*-axis, respectively. The FWHMs of rocking curves are 0.30° (//*c*) and 0.22° (//m). The FWHM along *c*-axis is larger than that along *m*-axis, in reverse to the case of planar template grown with similar conditions (sample C measured in section 3.1.4). This is possibly related to the wing tilt, as discussed by H. Wang *et al.*[10] Wing tilt is commonly observed in HVPE ELO growth and its formation is theoretically explained by A. E. Romanov et al.[46]

Low temperature (LT) μ-photoluminescence (PL)

LT (T = 7K) μ-PL measurements were performed on the mask and window areas of the fully-coalesced ELO sample, in order to have access to the local optical properties of GaN layer. The spectra are presented in figure 3.2.6.

The spectrum of window area is still dominated by BSF-related emission peak near 3.42 eV. The emission peak at 3.47 eV is related to the NBE. For the mask area, the NBE emission peak dominates the spectrum. This indicates a strong reduction of the defects density, though the BSF-related peak does not extinct. The FWHMs of NBE peak for both window and mask areas are ~ 15 meV. The DAP-related emission peak at 3.28 eV is quite intense, maybe due to mask impurity contamination. Overall, μ-PL scans demonstrate an improvement of optical properties in the mask area.

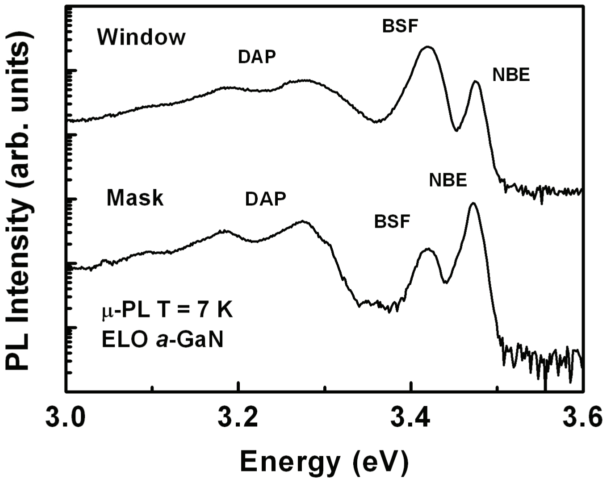

Figure 3.2.6 LT (T = 4K) μ-PL spectra of ELO GaN template on both window and mask areas.

Transmission electron microscopy (TEM)[**]

From a TEM cross-section view [figure 3.2.7 (a)], both edge and screw type threading dislocations (TDs) can be observed in the mask area. The edge TDs are aligned along [0001] directions, with a Burgers vector $\vec{b} = <0001>$. They are mostly located near SiO_2 mask and do not propagate toward the top surface. The screw TDs are parallel to the growth direction and thus propagate to the top. They have a Burgers vector $\vec{b} = \frac{1}{3} < 11\bar{2}0 >$. In the window area, the dislocation density is so high that it is difficult to discriminate different types.

Figure 3.2.7 (b) is a top-view image. According to the invariability criterion for electron channeling contrast imaging, screw TDs cannot be observed under the diffraction condition **g** = (0002). Instead, there are small dots, the traces where they intercept the surface, marked by the black arrows. In the window area, mixed TDs with $\vec{b} = \frac{1}{3} < 11\bar{2}3 >$ has been observed. Their density is ~ 1× 10^9 cm^{-2}. Mixed type TDs seem rare in the mask area.

Figure 3.2.7 (c) is the cross-section view of the coalescence front where Ga- and N- faces meet, leaving a void near the mask. A grain boundary forms at the front. Dislocations are found near the void and boundary.

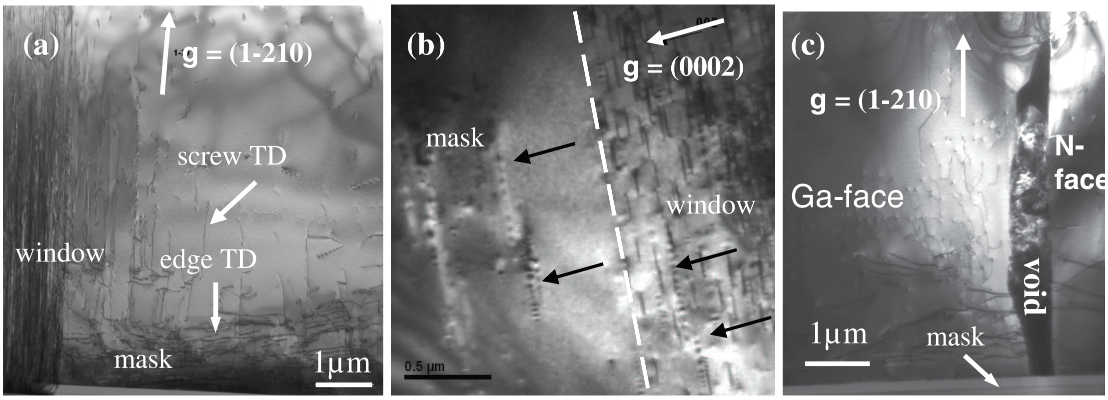

Figure 3.2.7 TEM micrograph of the dislocation distributions in the coalesced ELO sample: (a) bright field cross-section image under g = (1-210) and (b) top-view dark filed image under g = (0002). Black arrows in (b) mark the traces where the screw TDs with intercept the surface. (c) cross-section bright field image under g = (1-210) diffraction condition, which shows the region around a void originating from the coalesce of the +*c* and –*c* faces. (By courtesy of Yadira Arroyo at CIME EPFL)

The total TD density is high: ~ 1× 10^{10} cm^{-2}. It is reduced to 10^8-10^9 cm^{-2} in the mask areas, depending on the location. For example, the density is ~ 10^9 cm^{-2} near windows and voids, whereas it is in the low 10^8 cm^{-2} elsewhere.

Discussion on the presence of BSFs in the +*c* wing of mask areas

Ideally, +*c* wing should be almost free of BSFs, since mask stripes are aligned parallel to $[1\bar{1}00]$ direction so that those BSFs in window areas are not supposed to penetrate into the

---

[**] The TEM characterizations were performed by Yadira Arroyo at CIME, EPFL.

mask areas. However, BSFs with a density of ~ 2×10^4 cm^{-1} have been found in +*c* wing by both CL and TEM. T. Gühne *et al.*[42] have listed two possible reasons:

(1) Substrate misorientation: they attribute the presence of BSFs to the miscut of sapphire substrates. However, this reason is probably not valid in our case since the substrates used are on-axis with small error margin (< ±0.1°).

(2) Mask misorientation: the stripes are not perfectly parallel to GaN $[1\bar{1}00]$ direction since there are inevitable errors of the pattern alignment during the photo-lithography process. In result, BSFs may shift from the windows and penetrate into the overgrown mask areas.

In addition, there is another factor worth mentioning:
(3) Recall the observation from CL (figure 3.2.4) that BSFs in +*c* wing accumulate in bundles. Actually, this has also been found by TEM, as figure 3.2.8 (a) shows a cross-section image, where a bundle of BSFs originate from the interface of Ga-face overgrown layer and SiO_2 mask. They propagate to the top surface without any interruption. High resolution TEM image shows that SiO_2 mask surface is not flat [figure 3.2.8 (b)] and the mask imperfection may account for the formation of BSFs. Another possible reason is that the elastic stress generated during ELO may be partially relieved by BSFs, since their formation energy is quite low for GaN (*e.g.* 18.1 erg/cm^2 for I_1 BSF).[36]

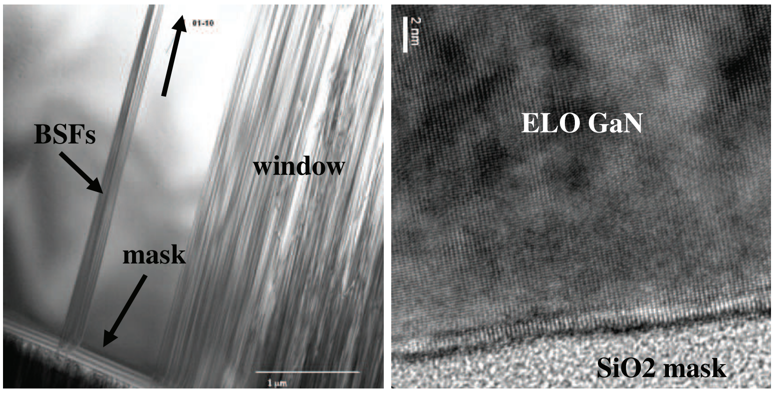

Figure 3.2.8 (a) TEM image of cross-section view on ELO *a*-plane GaN template; and (b) high resolution TEM image at the interface between GaN and SiO_2. (By courtesy of Yadira Arroyo at CIME EPFL)

3.2.3 Summary

A-plane GaN ELO templates have been grown by HVPE. The impacts from the stripe patterns and the growth parameters have been investigated. Stripe patterns should be aligned parallel to *m*-axis and the growth conditions should be similar to those applicable for planar templates.

In the mask area, the material quality is much improved. For example, TD density is reduced to ~ 10^8 cm^{-2}, compared to ~ 10^{10} cm^{-2} in the window areas. BSF density is also reduced by one order of magnitude in the mask area to ~ 10^4 cm^{-1}. Besides, the surface is smoother with rms roughness ~ 0.4 nm, similar to that of planar *c*-plane. As collateral evidence, the PL spectrum in the mask area is no longer dominated by the emission peak related to BSFs.

Instead, it is dominated by NBE peak. Overall, the material quality in the mask area is qualified for the fabrication of nanostructures.

3.3 Planar *m*-plane GaN grown on *m*-plane sapphire

This section is about the other non-polar orientation: *m*-plane $(10\bar{1}0)$. *M*-plane GaN layers have been heteroepitaxially grown on substrates such as (100) γ-$LiAlO_2$,[47, 48] *m*-plane ZnO,[49] *m*-plane 4*H*-[50] and 6*H*-SiC[51]. Compared with sapphire, these substrates have some disadvantages: first, at least for the time being they are much more expensive (~ 10 times the price). Secondly, ZnO and $LiAlO_2$ are not thermal-stable in the conventional growth condition of GaN (high temperature, H_2 and NH_3 environment) and may decompose and induce impurity incorporation into GaN epilayers. Third, the thermal expansion coefficient of SiC is smaller than GaN in GaN $[11\bar{2}0]$ direction (GaN $5.59 \times 10^{-6}\,K^{-1}$ vs 6*H*-SiC $4.46 \times 10^{-6}\,K^{-1}$), so it may induce cracks during the post-growth cooling stage.

Sapphire could be a good candidate, but there had been no reference until 2008, when R. Armitage and H. Hirayama reported *m*-plane GaN grown on *m*-sapphire by MOVPE, using a LT AlN NL.[52] In the case of HVPE, GaN directly grown on *m*-sapphire usually resulted in the formation of semi-polar orientations such as $(10\bar{1}3)$ and $(11\bar{2}2)$.[53] In fact, our investigations will show that GaN epilayers of three different crystal orientations can be achieved on *m*-sapphire: two semi-polar $(10\bar{1}3)$ and $(11\bar{2}2)$, and one non-polar $(10\bar{1}0)$.

This section will first discuss how these three different GaN orientations can be grown on *m*-plane sapphire (section 3.3.1) and then it will focus on *m*-plane GaN epilayers (section 3.3.2).

3.3.1 Three different GaN orientations

Different sapphire surface treatments and growth procedures have been carried out on *m*-sapphire and the orientations of as-grown GaN epilayers are summarized in table 3.3.1.

Samples	*in situ* Surface treatments	Growth procedures	GaN layer orientations
A	10' H_2 cleaning (900°C) + 5' NH_3 nitridation (600°C)	LT NL (600 °C) +HT growth (1040 °C)	Non-polar $(10\bar{1}0)$
B	10' H_2 cleaning (900°C) + 5' NH_3 nitridation (900°C)	LT NL (600 °C) +HT growth (1040 °C)	Semi-polar $(10\bar{1}\bar{3})$
C	H_2 and NH_3 provided during temperature ramping	HT growth (1040 °C)	Semi-polar $(11\bar{2}2)$

Table 3.3.1 Three different sapphire surface treatments and growth procedures and the corresponding GaN orientations.

In this table, samples A and B use identical growth procedure: the conventional two-step one that is widely practiced for *c*-plane GaN. What makes the difference is the sapphire surface treatment prior to the growth, which will be discussed in detail in the following. The growth condition for sample C is similar to that of *a*-plane GaN on *r*-plane sapphire, *i.e.* direct HT growth at low pressure (P_g ~ 100 mbar).

The XRD symmetric $\omega - 2\theta$ scans for samples A-C are presented in figure 3.3.1 (a) –(c), respectively. For sample A, only GaN $(10\bar{1}0)$, $(20\bar{2}0)$, and $(30\bar{3}0)$ peaks, along with sapphire $(30\bar{3}0)$ peak, are observed. The FWHMs of GaN $(10\bar{1}0)$, $(20\bar{2}0)$, and $(30\bar{3}0)$ peaks are 0.30°, 0.23°, and 0.16°, respectively. The enlarged inset shows that no semi-polar GaN orientation is found in the vicinity of sapphire $(30\bar{3}0)$ peak, within the detection limits of our XRD system. Sample B is of semi-polar GaN $(10\bar{1}\bar{3})$ orientation.[53] The FWHM of GaN $(10\bar{1}\bar{3})$ peak is 0.14°. Sample C is of semi-polar GaN $(11\bar{2}2)$ orientation, and the peak FWHM is ~ 0.4°.[53] Note that *c*-plane GaN peaks have not been found in any of these samples.

Nomarski optical microscopy reveals that planar templates of these three orientations have distinctive surface morphology: $(10\bar{1}0)$ plane is smooth and mirror-like, with anisotropic features aligned along $[11\bar{2}0]$ direction [figure 3.3.1 (d)]; $(10\bar{1}\bar{3})$ plane is covered by terraces, and the terraces exhibit triangle-structure [figure 3.3.1 (e)]; and $(11\bar{2}2)$ plane is smooth, with slate-like feature along $[11\bar{2}1]$ direction [figure 3.3.1 (f)].

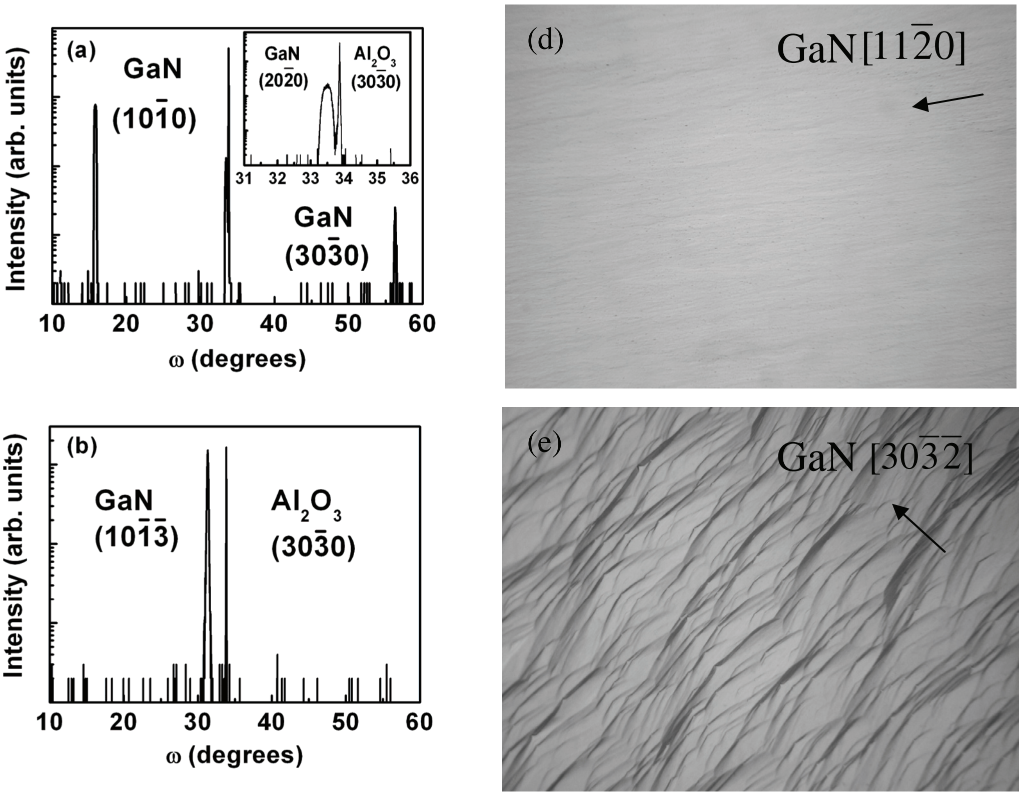

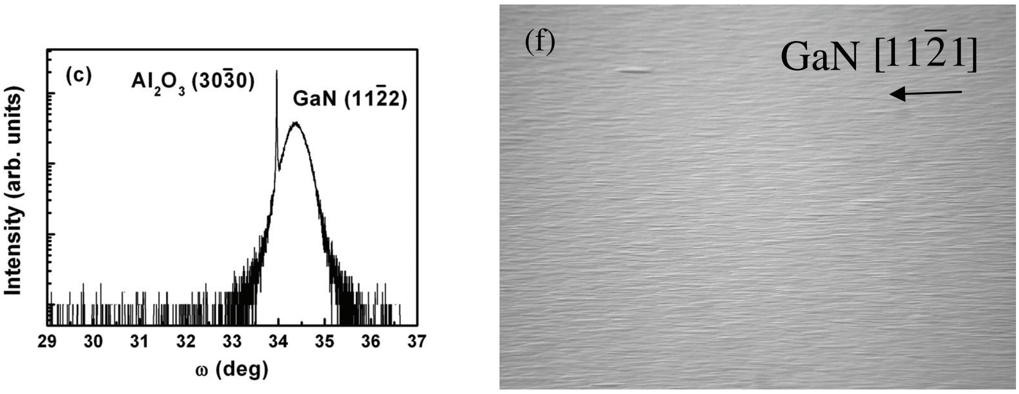

Figure 3.3.1 (a) – (c) spectra of XRD symmetric $\omega - 2\theta$ scans for samples A – C, respectively. (d) – (f) Nomarski optical micrographs (700 × 525 μm^2) of samples A-C, respectively.

Discussion of *in situ* sapphire surface treatment

Sapphire surface treatment may cause change in two aspects: surface chemistry (*e.g.* chemical composition) and surface physics (*e.g.* surface reconstruction). Particularly, it is reported that $(10\bar{1}0)$ *m*-plane sapphire under long-time HT annealing (t > 1 hour, T > 1000 °C) can form inclined facet of $(1\bar{1}02)$ and $(10\bar{1}1)$ orientations, driven by a minimization of the surface free energy.[54] This indicates that *m*-plane sapphire is not as thermally stable as *r*- or *c*-plane. To study the effect of surface treatment, the GaN/sapphire interfaces of samples A – C have been characterized by TEM.[††]

First, let us discuss the difference between samples A and B. Experiments have demonstrated that *in situ* sapphire surface treatments before the deposition of LT GaN NL decisively affect the crystal orientations of as-grown GaN layers. Indeed, with identical growth procedure, different surface preparations result in different GaN planes, *i.e.* either non-polar *m*-plane $(10\bar{1}0)$ or semi-polar $(10\bar{1}\bar{3})$.

Figure 3.3.2 shows two TEM images of GaN/sapphire interfaces for samples A and B, respectively. For sample A, the growth direction is GaN $[10\bar{1}0]$ and the growth direction for sample B is $[10\bar{1}\bar{3}]$. Both interfaces are quite abrupt, without much perturbation. No micro facet or step bunching can be identified, since the annealing temperature is lower than 1000 °C and the time is short (10 min). Therefore, interface morphology is not responsible for the difference of GaN orientation. Besides, there are BSFs in GaN epilayers, originating from the interface, as marked by arrows.

[††] TEM characterizations have been conducted by P. Vennéguès from Centre de Recherche sur l'Hétéroépitaxie et Ses Applications – Centre National de la Recherche Scientifique (CRHEA-CNRS).

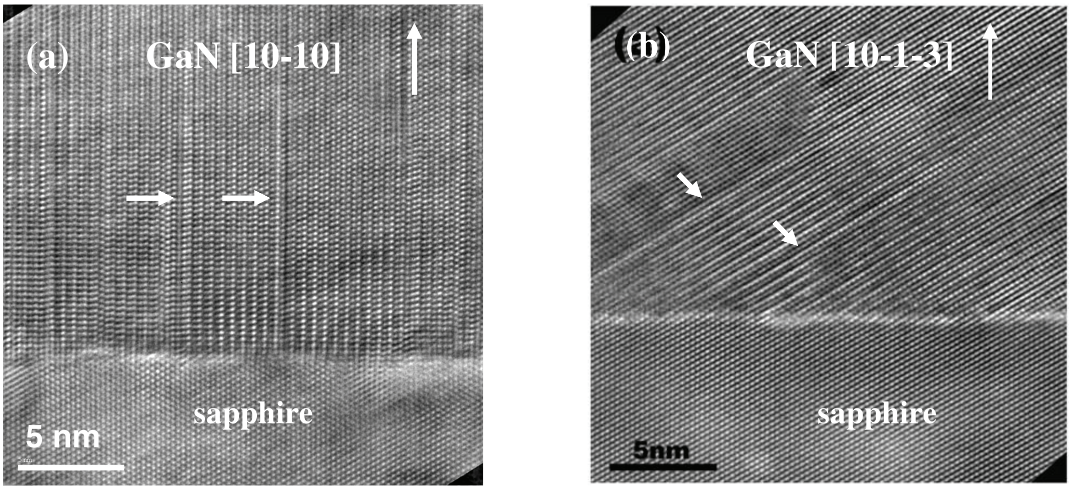

Figure 3.3.2 TEM images at the interface of GaN/sapphire for (a) sample A and (b) sample B, in the zone axis of sapphire [0001]. Arrows indicate BSFs, which originate from the interface. (By courtesy of P. Vennégués at CRHEA-CNRS)

Instead, surface chemistry related to H_2 cleaning and NH_3 nitridation could be the main cause. On *m*-plane sapphire, the ideal surface is terminated by both Al and O atoms, as described in section 1.5. However, the surface chemistry of as-received sapphire wafers is probably modified since the surface may experience oxidation when exposed to air. As a result, the surface chemical reactivity can be reduced and accordingly affects the following nitridation process. Thermal annealing of sapphire substrates in H_2 ambient is basically a “cleaning” process. It is a conventional technique to remove surface damage,[55] restore and de-oxidize the surface.[56] To confirm that H_2 cleaning is necessary, two additional samples D and E were prepared without H_2 cleaning, *i.e.* only NH_3 nitridation at T ~ 600 and 900 °C, respectively (table 3.3.2). We found that the orientation remains $(10\bar{1}\bar{3})$.

Samples	**H_2 Cleaning (T ~ 900 °C)**	**NH_3 (T ~ 600 °C)**	**NH_3 (T ~ 900 °C)**	**GaN planes by XRD**
A	X	X		*m*-plane $(10\bar{1}0)$
B	X		X	Semi-polar $(10\bar{1}\bar{3})$
D		X		Semi-polar $(10\bar{1}\bar{3})$
E			X	Semi-polar $(10\bar{1}\bar{3})$
F	X			Semi-polar $(10\bar{1}\bar{3})$

Table 3.3.2 Samples grown by the same two-step procedure but with different *in situ* surface treatments of *m*-plane sapphire substrates, and crystal orientations of the as-grown GaN epilayers.

Even so, H_2 thermal cleaning alone is necessary but not sufficient to obtain *m*-plane GaN. In fact, sample F with H_2 cleaning alone results in semi-polar $(10\bar{1}\bar{3})$ orientation, too. Actually, a specific nitridation step is required to promote the *m*-plane GaN orientation.

The effects of nitridation at HT (800 – 1100 °C) on *c*-plane sapphire have been extensively studied.[1, 57, 58, 59] It was shown that the adsorbed N atoms diffuse into sapphire and substitute to O atoms. The diffusion depth of nitrogen-related species depends on parameters such as temperature, time and pressure. The various reported values range from a few MLs up to several nanometers, along with the formation of either AlN[57] or Al-O-N[1] amorphous thin layer near the surface. In the case of *m*-plane, if the surface is supposed to be highly de-oxidized after H_2 cleaning, the nitridation of sample B, performed at T ~ 900 °C, is then expected to strongly modify the surface chemistry. This could be the driving force for the formation of GaN semi-polar orientation. In fact, this observation is consistent with other reports on HT-nitridated *m*-plane sapphire which lead to semi-polar GaN.[53, 60] On the other hand, for nitridation at T ~ 600 °C, the calculated nitrogen diffusion depth in *c*-plane sapphire by Hashimoto *et al.*[58] is less than a single Al_2O_3 ML, indicating that the reaction is limited to the surface. Though relevant reference on *m*-plane sapphire is lacking, it is reasonable to assume that the diffusion depth of sample A (nitridation T ~ 600 °C) is much smaller than that of sample B (nitridation T ~ 900 °C). In addition, complete nitridation at this low temperature is expected since the full dehydrogenation of the adsorbed NH_3 occurs at ~ 500 °C.[59] In our experiments, providing NH_3 for a minimum of 3 min at T ~ 600 °C results in *m*-plane GaN, reproducibly and uniformly. Shorter exposure time leads to non-reproducible orientations, likely due to insufficient nitridation.

After the discussion of sample A and B, let us take a look at sample C, which uses a single-step HT growth procedure. Figure 3.3.3 shows the interface of GaN and sapphire in the zone axis of sapphire $[11\bar{2}0]$, where periodic micro facets of $(1\bar{1}02)$ and $(1\bar{1}01)$ are formed at sapphire surface, driven by a minimization of surface energy.[54] They are induced by longer-time surface treatment at higher temperature (T ~ 1040 °C), compared to samples A and B. Especially, $(1\bar{1}02)$ *r*-plane nano-facets are formed with a tilt of 32.4° from the interface plane (marked by arrows), which provide nucleation sites for *a*-plane GaN, and that is why the growth orientation is semi-polar ($11\bar{2}2$). This phenomenon has been reported in MOVPE–grown GaN $(11\bar{2}2)$ samples by P. Vennégués *et al.*[61] Therefore, a LT GaN NL is mandatory to protect the sapphire surface from HT-annealing-induced surface faceting.

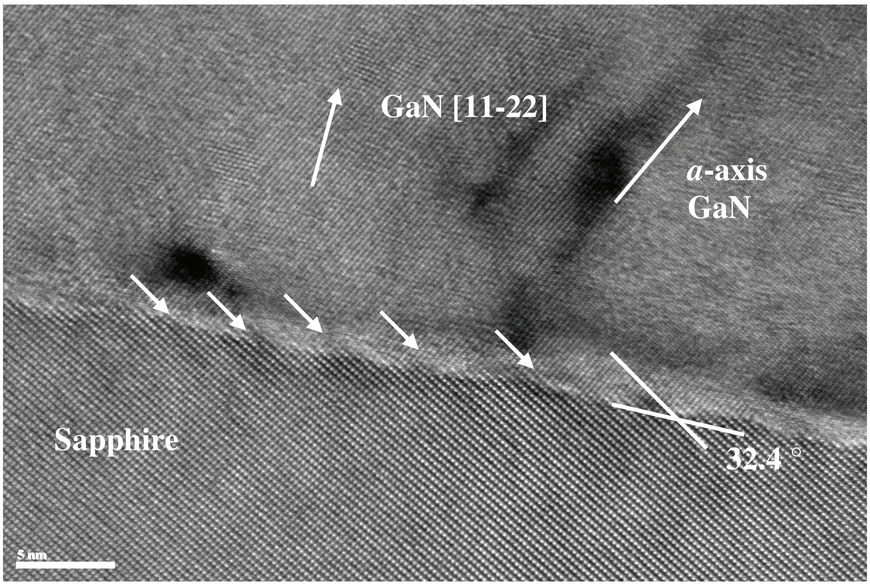

Figure 3.3.3 TEM images of GaN/sapphire interface in the zone axis of GaN $[1\bar{1}00]$ for sample C. The arrows indicate the inclined *r*-plane nano-facets formed at the GaN/sapphire interface. (By courtesy of P. Vennégués at CRHEA-CNRS)

In conclusion, it is probably the sapphire surface chemistry that leads to two different GaN orientations $(10\bar{1}0)$ and $(10\bar{1}\bar{3})$, while GaN $(1\bar{1}02)$ is due to the formation of *r*-plane nano-facets at sapphire surface, *i.e.* a change in surface physics.

3.3.2 *M*-plane GaN – growth and characterizations

Growth procedures

The standard experiment procedure has been recorded by *in situ* LR (figure 3.3.4). The substrates are on-axis (± 0.1°) *m*-plane sapphire. No *ex situ* treatment is needed. After loading as-received sapphire substrate into the HVPE chamber, the temperature rises up to 900 °C with N_2 carrier gas. The substrate is first thermally annealed in H_2 and N_2 environment for about 10 min. Next, the substrate is nitrided at ~ 600 °C in NH_3 and N_2 environment. These combined two steps are the aforementioned *in situ* surface treatments. AFM scan on the treated sapphire shows that the surface is featured by atomic steps with height of ~ 0.2 nm [figure 3.3.4 (a)]. They are randomly distributed and no obvious pattern is observed. Such morphology is similar to that of the wafers received from the supplier. The rms roughness is ~ 0.06 nm on the scale of 1 × 1 μm^2. As I mentioned before, *m*-plane sapphire surface is not stable under thermal annealing at high temperature (> 1000 °C) for quite long time (hours up to one day), leading to microscopic-facet formation due to a minimization of the surface free energy.[54, 62] However, such micro-facets are not found here. The reason is that the temperature used is lower than 1000 °C and the time is rather short (~ 10 min).

After surface treatment, the growth begins with the deposition of a LT (T ~ 600 °C) GaN NL (*d* ~ 30 nm). This LT NL is quasi-2D, judging from *in situ* LR. AFM scan (1 × 1 μm^2) shows that the rms roughness is about 3 nm, with average height ~ 10 nm [figure 3.3.4 (b)].

Then, the temperature rises up to T ~ 1040 °C under $H_2/NH_3/N_2$ environment for recrystallization. The reflectance signals increase gradually with T due to a T-dependant change in the optical constants and then decrease slightly after T reaches 1000 °C, as a result of etching of ~ 5 nm by H_2.[28] The AFM scan (1 × 1 μm^2) shows that the recrystallized NL is actually composed of pillars (size ~ 100 nm) [figure 3.3.4 (c)]. *In situ* LR is not sensitive to such small feature and accordingly the reflectivity does not drop. The rms roughness is about 6 nm. The average height is ~ 25 nm, equivalent to the NL thickness (30 nm minus 5 nm etched-away). Both AFM and LR characterizations suggest that the formation of large GaN crystal islands on NL, which occurs in the case of *c*-plane, is somehow missing for *m*-plane. This situation also happens to *a*-plane, as discussed in section 3.1.2. Therefore, the defect density in *m*-plane GaN is expected to be much larger than that of planar *c*-GaN.

HT growth (T ~ 1040 °C) follows the recrystallization. The growths were performed at atmospheric pressure, with V/III ratio about 100. The HT growth duration was about 20 min with a growth rate of 15 – 20 μm/h. The GaN layer thicknesses are ~ 6 μm. The corresponding reflectance signals drop initially, then rise gradually, and oscillations are clearly observed, indicating a 2D growth mode. There is a strong in-plane growth anisotropy with elongated "slate-like" feature along GaN $[11\bar{2}0]$ direction, which has also been reported in planar *m*-plane GaN epilayers grown on γ–$LiAlO_2$ substrate [figure 3.3.4 (d)].[47] The rms roughness on 1 × 1 μm^2 AFM scan is ~ 0.5 nm, with an average height of 2 nm. This kind of feature is not related to intrinsic property of *m*-plane, instead it is due to high-density of defects. Kim *et al.* has also reported such feature in their planar layers, while the surface of their ELO layers is characterized by well-defined atomic steps similar to those observed in *c*-plane due to "step flow" growth mode.[63] A. Hirai *et al.* has reported that the yield of this kind of "slate" morphology in *m*-plane GaN epilayers grown on SiC substrates is correlated with the high-density BSFs.[64]

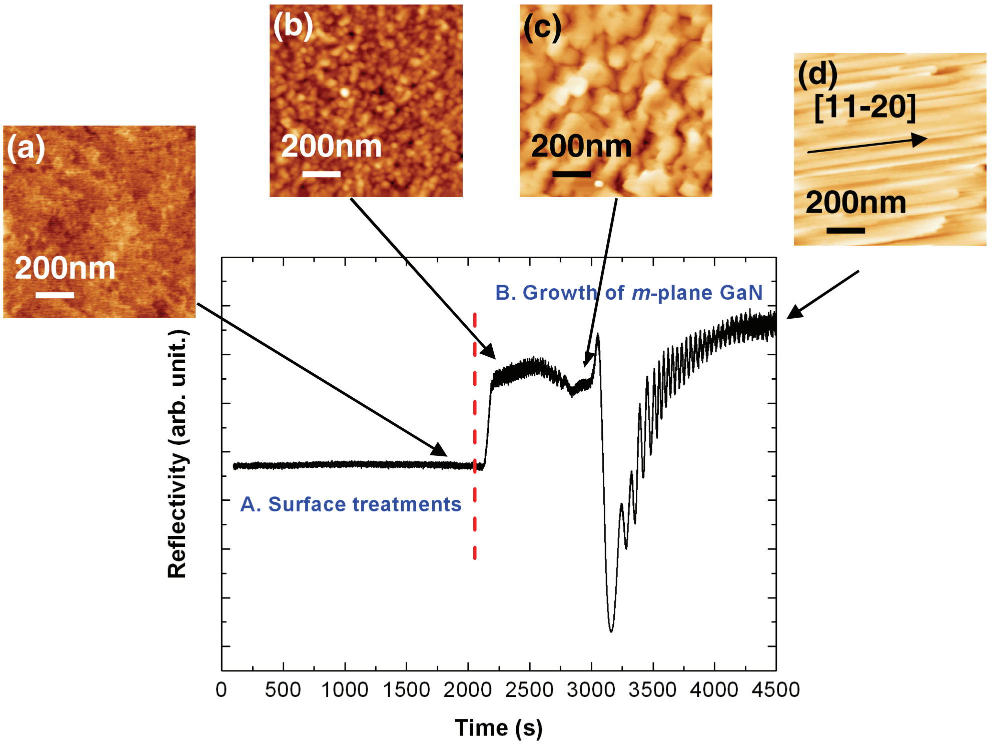

Figure 3.3.4 *In situ* LR signals of the entire experiment process of growing *m*-plane GaN on *m*-plane sapphire. Insets are AFM images (1 × 1 μm^2) of the template surface at different experiment stages: (a) *m*-plane sapphire right after the surface treatments, (b) LT GaN NL, (c) the recrystallized NL, and (d) the as-grown *m*-plane GaN layer.

At this stage, it is worthwhile to mention that planar *a*-plane GaN epilayers are also featured by the presence of high-density BSFs, but its anisotropy is along [0001] direction with no "slate-like" morphology (section 3.1.1). In other words, the surface morphology of *a*-plane GaN seems not to be affected by BSFs.

To explain this issue, let us take a look at how BSFs affect *m*- and *a*-plane surface, repectively. Figure 3.3.5 (a) is a cross-section view of GaN hexagonal structure in $\{11\bar{2}0\}$ direction. It illustrate a protruding step on $\{10\bar{1}0\}$ *m*-plane, which is introduced by a type I_1 BSF (marked by the arrow) as the stacking sequence changes from AB to ABC. [65] This step provides nucleation sites and promotes the growth along $\{11\bar{2}0\}$ direction. By comparing the normal configuration (red dash-line frame) with the BSF-related configuration (blue dash-line frame), one can see that the effect of BSF is to rotate the normal configuration by 180°. This change is clearer from the top view in [0001] direction, as shown in figure 3.3.5 (b). In contrast, *a*-plane is not impacted by the BSF, because this 180° rotation does not introduce additional steps on the surface. This explanation is consistent with the report of Moram *et al.* that I_1 and I_2 BSFs affect symmetric ω-scans on *m*-plane, but not on *a*-plane.[30]

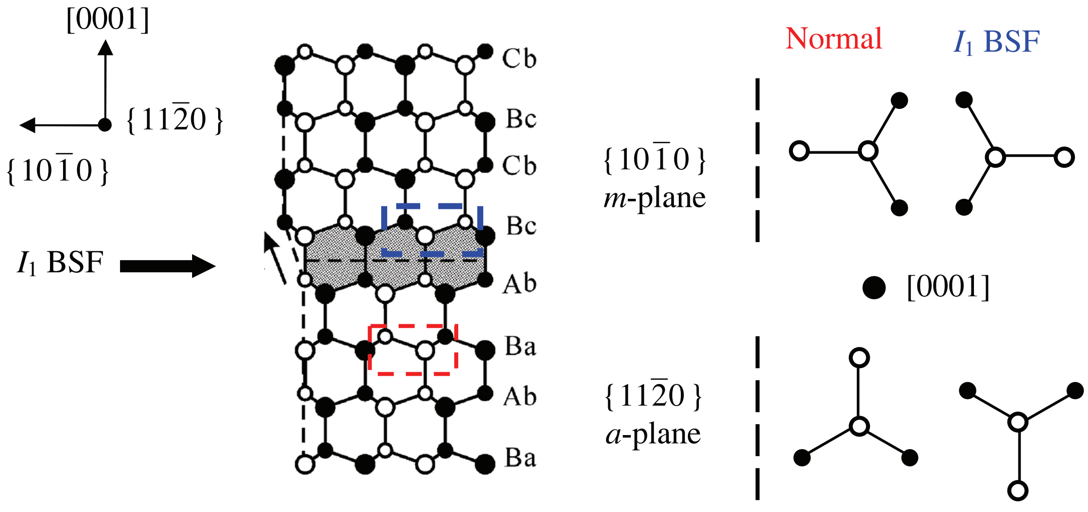

(a) (b)

Figure 3.3.5 (a) is a cross-section of GaN hexagonal structure in $\{11\bar{2}0\}$ direction. It illustrates a step introduced by a type I_1 BSF. The red and blue dash-line frames indicate the normal and the BSF-related configurations, respectively, after Ref. 65. (b) is a top view of the normal and the BSF-related configurations in [0001] direction for *m*- and *a*-planes, respectively.

Discussions of experimental parameters

(a) The temperature of H_2 thermal annealing

Effective thermal annealing can be achieved in the range of 800–900 °C. If the temperature is further increased to 1000 °C or higher, the orientations of GaN epilayer turn to be a mixture of $(10\bar{1}0)$ and $(10\bar{1}\bar{3})$. A possible explanation is that unintentional contaminations from parasitic depositions in the reactor occur near the standard growth temperature for GaN. Some N-species decomposed from parasitic depositions may partially nitridate the surface and thus change the surface chemistry.

(b) H_2 in the carrier gases

For HT growth after recrystallization, keeping other parameters identical, the growth rate is larger when H_2 is cut off. From the thermodynamics point of view, the increase of H_2 mole fraction in the carrier gas reduces the reaction rate.[22] Besides, the absence of H_2 results in dense cracks in the layer, as shown in figure 3.3.6. This has also been reported in HVPE *c*-GaN homoepitaxy layers.[66] The cracks appear to be related to grain boundaries. To avoid that, H_2 is required for HVPE growth of *m*-plane GaN.

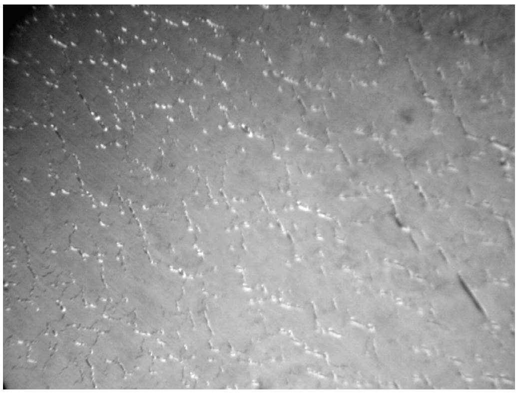

Figure 3.3.6 Nomarski optical micrograph of *m*-plane GaN epilayer grown without H_2 carrier gas (140 × 105 μm^2). Dense crack network can be observed in the surface.

(c) Growth temperature T_g

After recrystallization, the growth is usually conducted at $T_g \sim 1040$ °C, similar to that of *c*-plane GaN. Further increase to 1060 – 1080 °C *i.e.* T_g suitable for *a*-plane GaN does not make significant difference in terms of surface morphology. However, if T_g is reduced to below 1000 °C, surface morphology starts to change. Figure 3.3.7 (a) is a Nomarski optical micrograph of *m*-plane GaN epilayer grown at 900 °C. The surface is covered by macroscopic pyramidal hillocks with average size of about 200 × 100 μm^2. This kind of hillocks has been reported by A. Hirai *et al.* on *m*-plane GaN homoepitaxially grown on bulk substrates.[67] Figure 3.3.7 (b) is a Nomarski optical micrograph in transmission mode taken at the identical position of (a), where dense cracks can be observed. The cracks are roughly aligned parallel to GaN *a*-axis.

These hillocks are probably induced by dislocations, because in the center of each hillock there seems to be a dislocation core, as marked by the arrows in figure 3.3.7. The dislocations may introduce spiral growth. Therefore, to suppress hillocks, T_g should be kept above 1000 °C.

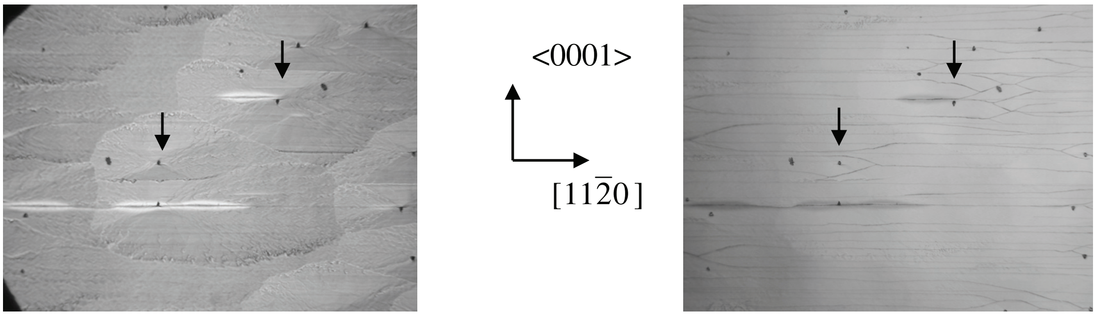

Figure 3.3.7 (a) Nomarski optical micrograph (700 × 525 μm^2) *m*-plane GaN grown at 900°C, (b) is a micrograph taken in transmission mode at the same position of (a).

The in-plane epitaxial relationship – Non-unique polarity

The epitaxial relationship between *m*-plane GaN and *m*-plane sapphire has been investigated by XRD and TEM[‡‡].

XRD off-axis ϕ scans are presented in figure 3.3.8. Due to the symmetry of hexagonal structure, *i.e.* the set of $\{10\bar{1}0\}$ planes for both GaN and sapphire are 60° off each other, the sample was tilted ($\chi = 60°$) to reveal GaN $(10\bar{1}0)$ [figure 3.3.8 (a)] and sapphire $(30\bar{3}0)$ planes [figure 3.3.8 (b)]. The peaks of these two planes are 90°-off each other. It means that the in-plane crystal orientations of GaN are perpendicular to those of sapphire, *i.e.* GaN <0001> // sapphire $[11\bar{2}0]$ and GaN $[11\bar{2}0]$ // sapphire [0001]. There are three points worth mentioning: first, XRD cannot determine the polarity of GaN <0001>, *i.e.* either [0001] or $[000\bar{1}]$; secondly, in figure 3.3.8 (b) the intensities of GaN $(20\bar{2}0)$ peaks are low, because here 2θ was set at 68.27° to match sapphire $(30\bar{3}0)$ instead of GaN $(20\bar{2}0)$, whose calculated value is nearby at 67.78°; third, *m*-plane ZnO, with the lattice constants ($a = 3.250$ Å, $c = 5.207$ Å) close to those of GaN, has the same epitaxial relationship when grown on *m*-plane sapphire.[68]

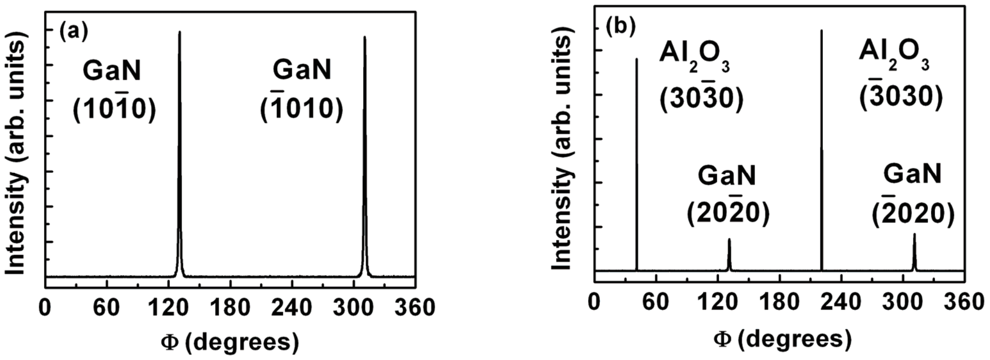

Figure 3.3.8 XRD off-axis ϕ scans for *m*-plane GaN grown on *m*-plane sapphire (sample A). The sample was tilted ($\chi = 60°$) to reveal (a) GaN $(10\bar{1}0)$ and (b) sapphire $(30\bar{3}0)$ planes, with 2θ set at 31.97 and 68.27°, respectively.

This epitaxial relationship has been confirmed by TEM measurements. Figure 3.3.9 (a) is the selected area electron diffraction (SAED) patterns taken in GaN $[11\bar{2}0]$ zone axis, where GaN $[11\bar{2}0]$ zone axis (green) overlap sapphire $[0001]$ zone axis (red). Following this relationship, the projection of bulk *m*-plane GaN on *m*-plane sapphire is presented in figure 3.3.9 (b). The solid-line and dash-line rectangles represent the unit cell of GaN and sapphire, respectively. In average, there are four units of GaN on each sapphire unit. The calculated average lattice mismatch along the GaN [0001] and $[11\bar{2}0]$ directions are 8.9 and -1.8 %, respectively.

[‡‡] TEM characterizations on *m*-plane GaN samples have been performed by P. Vennéguès (CRHEA-CNRS).

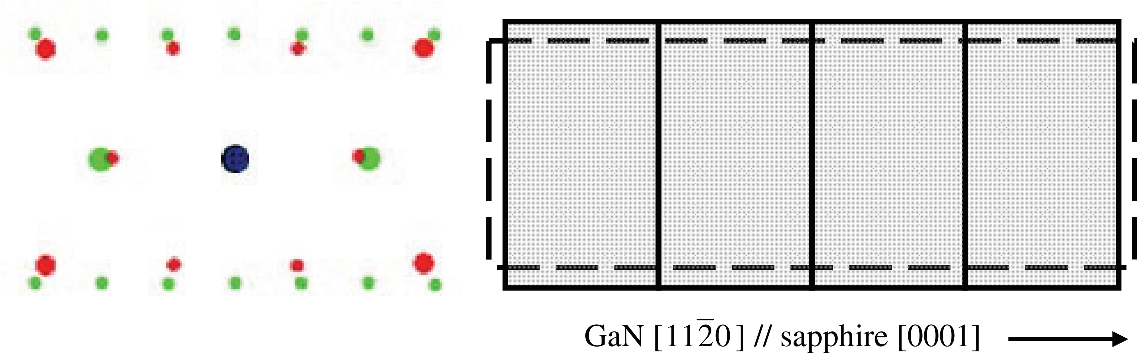

(a) (b)

Figure 3.3.9 (a) The SAED patterns of *m*-plane GaN and *m*-plane sapphire, where the red circles represent sapphire $[0001]$ zone axis, and the green ones GaN $[11\bar{2}0]$ zone axis. [By courtesy of P. Vennégués (CRHEA-CNRS)] (b) Projection of bulk *m*-sapphire and *m*-plane GaN, where the solid-line and dash-line rectangles represent the unit cell of GaN and sapphire, respectively;

As we know, *c*-plane layer has Ga- or N-polarity, but neither XRD nor SAED can discriminate the difference. In fact, the polarity is found to be non-unique. Figure 3.3.10 is a top-view TEM image showing the inversion domains in *m*-plane GaN epilayer. The polarities measured by CBED for the adjacent regions are the opposite, *i.e.* –*c*, +*c*, and –*c* for regions A, B, and C, respectively. In comparison, in-plane polarity of *a*-plane GaN grown on *r*-sapphire is unique. A mechanism that accounts for this phenomenon is explained in details by P. Vennégués *et al.*[69] In short, the in-plane polarity uniqueness of non-polar GaN epilayer is determined by that of sapphire substrate: if the sapphire substrate has a unique polarity, *e.g.* *r*-plane, so will be the GaN epilayer (*i.e.* *a*-plane). In comparison, *m*-plane sapphire is not unique in polarity, nor will be the GaN epilayer (*i.e.* *m*-plane).

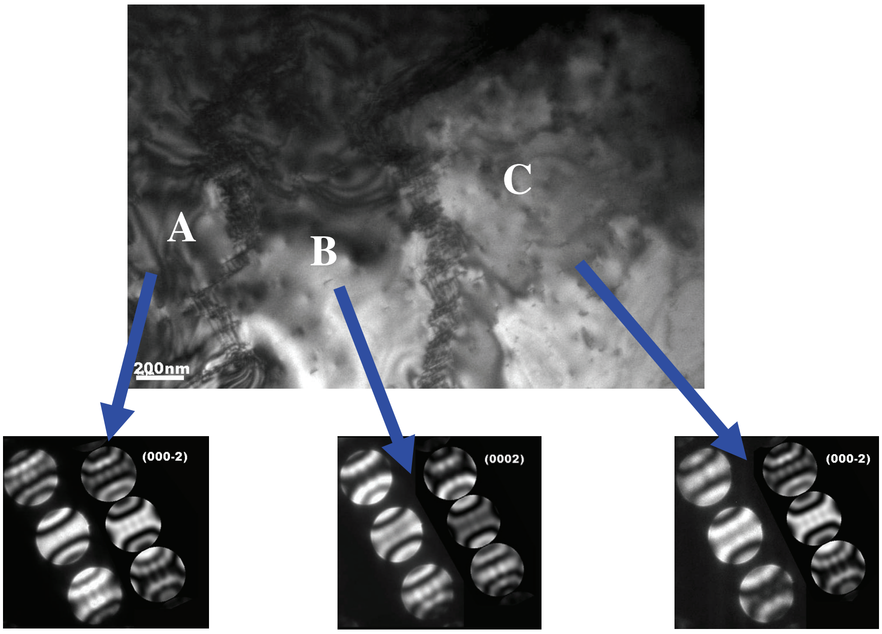

Figure 3.3.10 TEM image on *m*-plane GaN reveals inversion domains. The different polarities are determined by CBED experiments and simulations. By courtesy of P. Vennégués (CRHEA-CNRS).

Structural properties

The FWHMs of XRD ω rocking curves were measured to assess the crystal quality of *m*-plane GaN layers. The anisotropy of FWHMs as a function of the X-ray azimuth angles, similar to that for *a*-plane GaN, has been found. The FWHMs with incident X-ray beam aligned along GaN [0001] and GaN $[11\bar{2}0]$ directions are 0.87 and 0.25°, respectively. These values are comparable to those of planar *m*-plane GaN grown on *m*-plane SiC[51] and *m*-plane sapphire substrates[52] by MOVPE. Similar situation for a-plane has been discussed in section 3.1.4. In addition, M. B. McLaurin *et al.* has reported that FWHM broadening in [0001] direction is related to BSFs.[70]

A set of TEM cross-section images are presented in figure 3.3.11: (a) shows the region near GaN/sapphire interface. Occasionally, there are some voids at the interface, as marked by the arrow. Besides, the round circle indicates a tiny GaN crystal island (height ~ 10 nm and diameter ~ 10 nm) with semipolar orientation. Nevertheless, on the whole the single crystal orientation is not affected by these minor imperfections. (b) is a low magnification image, covering both LT NL and HT-grown layer. It seems that NL helps moderately to reduce the dislocation density, since the density is quite high close to the interface and decreases a bit after 30-40 nm, roughly equal to NL thickness. Even so, TD density in the upper layer is still about one order of magnitude higher than that of *c*-GaN – 1×10^{10} cm^{-2}. The average density of BSFs is ~ 4×10^{5} cm^{-1}. Also, PSFs have been found, as marked by the arrows. Basically, the defect structures are not that much different from those of *a*-plane GaN epilayers described in section 3.1.4.

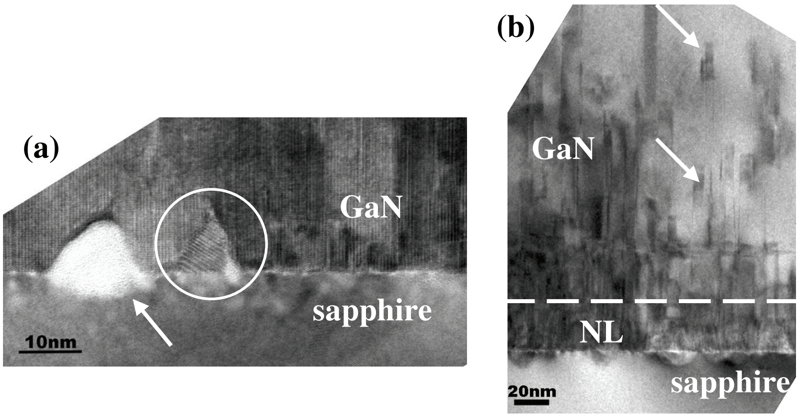

Figure 3.3.11 TEM cross-section images of *m*-plane GaN/*m*-plane sapphire interface: (a) show the interface of GaN/sapphire. The arrow marks a perturbation and the circle indicates a GaN crystal island of semipolar orientation; (b) is a low magnification image. The arrows mark PSFs, and the dash line gives a rough guide of NL. By courtesy of P. Vennéguès (CRHEA-CNRS)

Optical Properties

M-plane GaN samples have been characterized by LT (T = 10 K) PL. A representative spectrum is presented in figure 3.3.12. The peak is dominated by an emission peak at 3.426 eV, which is related to BSFs. The large linewidth (FWHM ~ 50 meV) indicates an inhomogeneous distribution of BSFs.[38] The emission peak near 3.32 eV is not yet clear, Liu *et al.* reported that this emission can be associated either with the PSFs or with the stair-rod dislocations at the intersection between BSFs and PSFs.[71] The near-band emission near 3.48 eV has low intensity and appears as a shoulder to the peak of BSFs.

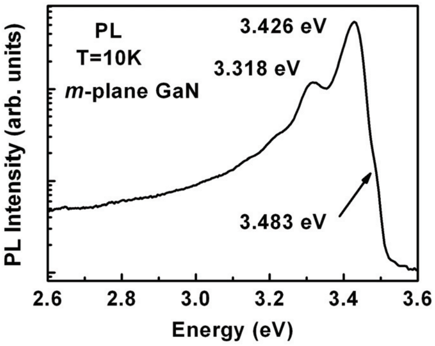

Figure 3.3.12 LT PL spectrum of HVPE planar *m*-plane GaN sample.

Discussion of misoriented sapphire substrates

It has been reported that substrates with small-misoriented angles can improve the structural properties of *c*-plane GaN epilayers of either Ga-[72] or N-polarity[73], whereas relevant report on *m*-plane is lacking. Here, three misoriented angles of *m*-plane sapphire have been tested: 1° off toward sapphire *c*-plane, and 1° and 2° off toward sapphire *a*-plane. The growth procedure is identical to that of on-axis substrate, with GaN layer thickness ~ 5 μm.

The surface morphologies of these three samples (together with an on-axis reference) are characterized by Nomarski optical micrograph with size of 280×210 μm^2, as shown in figure 3.3.13. The insets are AFM images with size of 10×10 μm^2. (a) is the reference sample, the surface is optically smooth. AFM scans shows that the surface is featured by slates in GaN $[11\bar{2}0]$ direction. The rms roughness is about 10 nm. (b) is the sample with substrate 1° toward sapphire *c*-plane. Its surface turns to be much rougher optically and is featured by grains aligned roughly along GaN $[11\bar{2}0]$ direction. The rms roughness is about 25 nm. (c) is the sample with substrate 1° toward sapphire *a*-plane. The slate-like feature along GaN $[11\bar{2}0]$ direction is quite distinct in both the optical micrograph and the AFM image. The rms roughness is about 15 nm. (d) is the sample with substrate 2° toward sapphire *a*-plane. Its surface morphology is similar to that of (c), but the rms roughness is reduced to about 7 nm.

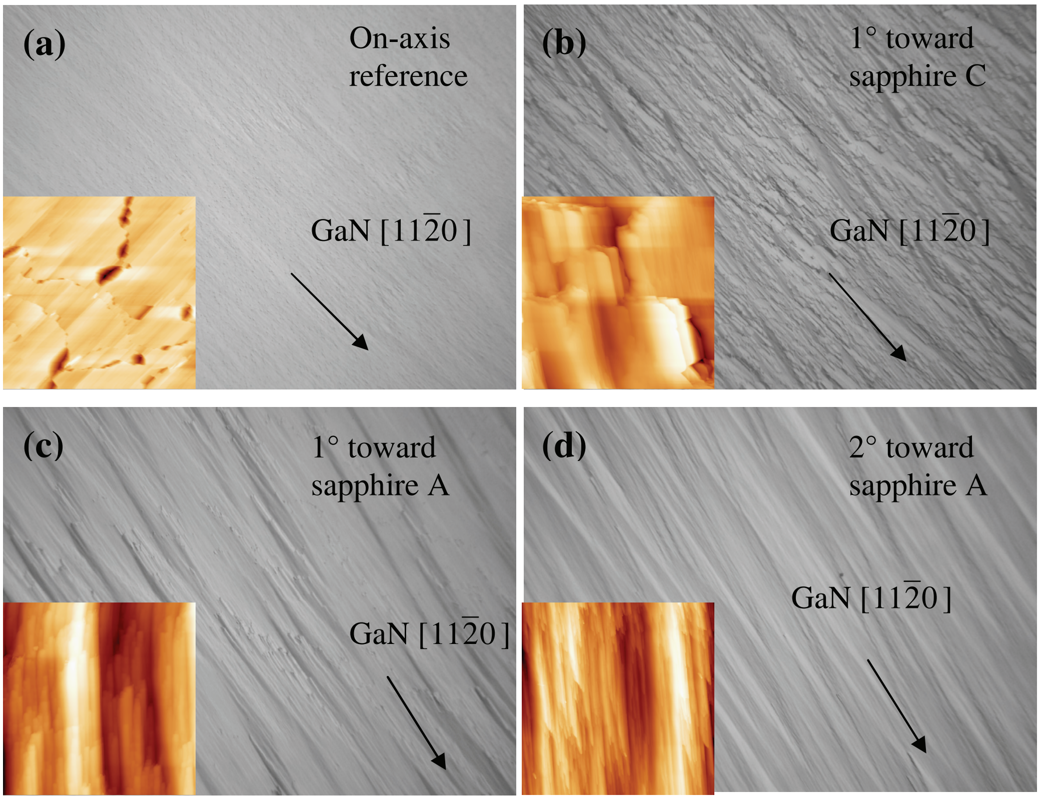

Figure 3.3.13 Nomarski optical micrographs (280 × 210 μm^2) of *m*-plane GaN epilayer grown on *m*-plane sapphire with misorientation angles of (a) 0, *i.e.* on-axis, (b) 1° toward sapphire *c*-plane, (c) 1° toward sapphire *a*-plane, and (d) 2° toward sapphire *a*-plane. The insets are AFM images (10 × 10 μm^2).

The surfaces of samples (c) and (d) are smoother than that of sample B. A possible explanation is that the misoriented angles toward sapphire *a*-plane (*i.e.* GaN *c*-plane) may introduce structural steps along GaN <0001> direction, which could moderately help to balance the strong growth anisotropy perpendicular to that direction. In fact, with a misorientation angle of 2°, the surface of (d) is smoother than the rest. Therefore, misoriented angles toward sapphire *a*-plane can help to improve surface morphology.

Besides, these four samples have been characterized by XRD and PL. However, no significant difference has been found among them. It suggests that the misoriented sapphire substrates do not strongly influence the material quality of GaN epilayers except the surface morphology.

3.3.3 Summary

This section deals with two issues:

(1) Three different GaN orientations can be grown on *m*-plane sapphire through the modification of surface chemistry and/or growth procedure:

M-plane can be obtained by sapphire surface treatment with H_2 cleaning (T ~ 900 °C) + nitridation (T ~ 600 °C), followed by two-step growth.

Semi-polar $(10\bar{1}\bar{3})$ can be obtained by sapphire surface treatment with H_2 cleaning (T ~ 900 °C) + nitridation (T ~ 900 °C), followed by two-step growth.

Semi-polar $(11\bar{2}2)$ can be obtained by HT nitridation (T > 1000 °C) and single-step growth.

(2) The experimental growth procedure of *m*-plane GaN epilayers have been described, together with impacts of some growth parameters. The samples have been characterized in terms of surface morphologies, structural and optical properties. The overall material quality is comparable to that of *a*-plane and is poorer than *c*-plane, as the defect density is high. Misoriented substrates can influence the surface morphology, but not the structural and optical properties. Therefore, ELO technique should be applied to reduce the defect density.

3.4 Epitaxy lateral overgrowth of *m*-plane GaN

3.4.1 Preliminary investigations

Results from previous section 3.3 demonstrate that HVPE growth procedure of planar *m*-plane GaN is similar to that of *c*-plane, except the sapphire surface treatments. Thus, the initial study of ELO growth on patterned *m*-plane templates began with these conditions applicable for *c*-plane: P_g = atmospheric pressure, V/III ratio ~ 100, T ~ 1040 °C. The mask stripes are aligned along GaN $[11\bar{2}0]$ direction, because BSFs are aligned in this direction. The ELO pattern is made of 5 μm window + 30 μm mask.

Figure 3.4.1 (a) is a SEM image for a growth of 30 min. One striking feature of ELO morphology is that the lateral growth rate is not uniform. For example, areas A and B (marked by arrows) have a faster growth rate but their directions are the opposite. It is attributed to the in-plane inversion domains found in *m*-plane GaN planar templates, as discussed in section 3.3.2. Besides, the top-view Nomarski optical micrograph inset shows that the overgrown GaN layer is not always continuous along $[11\bar{2}0]$ direction.

This morphology issue can be alleviated by increasing the surface mobility of adsorbed precursors through pressure reduction, temperature increase, and lower V/III ratio. For our HVPE system, the growth temperature ~ 1040 °C is already near the upper limit and V/III ratio change does not have significant impact except the growth rate. Hence, P_g was reduced to 200 mbar with other parameters unchanged and the ELO morphology is presented in figure 3.4.1 (b). The Nomarski optical micrograph inset shows that the uniformity is much improved in both *a*- and *c*-axis. It appears that low pressure is suitable for ELO growth to suppress the negative impact from inversion domains.

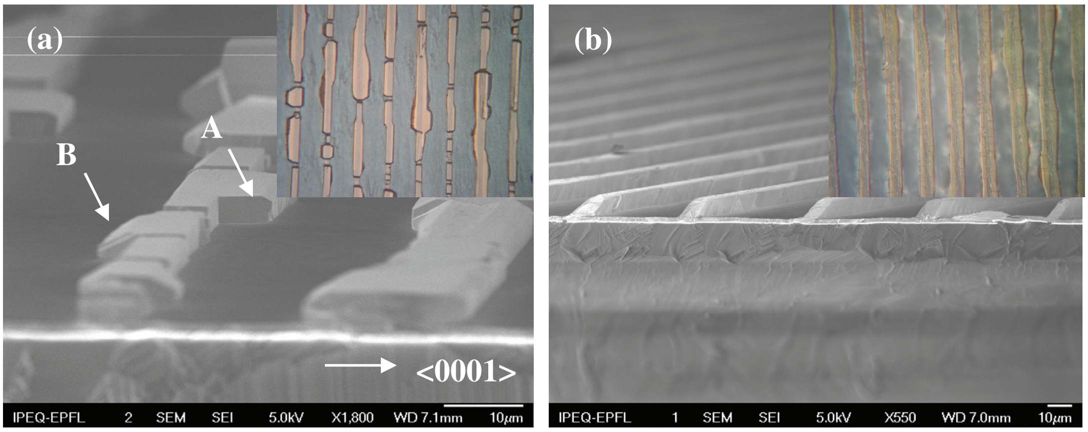

Figure 3.4.1 (a) and (b) are SEM cross-section images (taken from tilted angles) of *m*-plane HVPE ELO layer, grown at P_g at atmospheric and 200 mbar, respectively. The insets are top-view Nomarski optical micrographs (280 × 210 μm^2).

3.4.2 Coalesced ELO layer

Surface morphology

Several fully-coalesced ELO templates have been grown with P_g: 150 – 200 mbar. Top-view Nomarski optical micrograph (140 × 105 μm^2) shows the surface of a representative sample, which looks smooth at the macro-scale [figure 3.4.2 (a)]. AFM scans have been performed on three different positions: (b) near the border between mask and window areas (10 × 10 μm^2), (c) on the mask (2 × 2 μm^2), and (d) the coalescence front where two lateral growth planes meet (20 × 20 μm^2).

In the window area, the surface is featured by slate-like morphology. There is a strong growth anisotropy towards $[11\bar{2}0]$ direction like the planar template [figure 3.4.2 (b)]. In comparison, the surface in the mask area appears to be much smoother. The rms roughnesses for window and mask areas are 2.5 and 0.2 nm on 5 × 5 μm^2 scan, respectively. A closer look at the wing area reveals that the surface is not characterized by slate-like features. Instead, the typical feature is "step-flow", similar to that of *c*-GaN, as shown in figure 3.4.2 (c). The steps are not aligned to any specific crystallographic direction. The average height of the terrace is ~ 0.6 nm and the widths 100 - 200 nm. Figure 3.4.2 (d) reveals the coalescence area, where the front can be clearly identified (dash line). The growth along $[11\bar{2}0]$ direction seems not completely continuous, as there are some "plateaus", probably due to different growth rates of inversion domains. However, the height difference for the adjacent plateaus is only ~ 3 nm and the rms is ~ 2 nm for 20 × 20 μm^2.

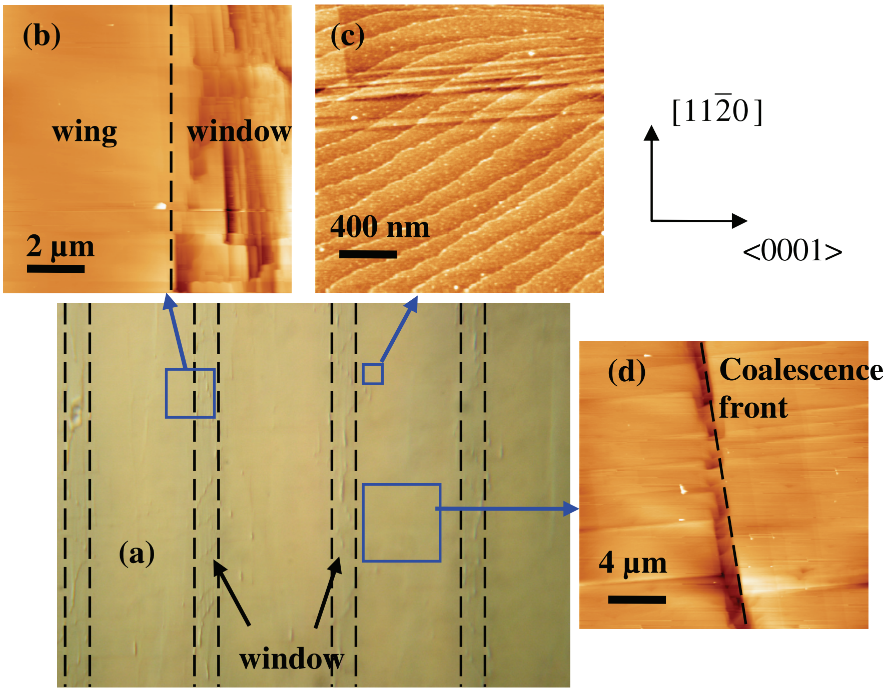

Figure 3.4.2 (a) Nomarski optical micrograph of a fully-coalesced *m*-plane GaN HVPE ELO layer, with size of 140 × 105 μm^2. The dash lines are guide to the window area. The AFM images (b) – (d) focus on three different positions, marked by the squares (blue). Dash line in (b) is a guide indicating the border between window and wing; dash line in (d) is a guide indicating the coalescence front.

XRD

XRD ω-scans have been performed on several samples with X-ray parallel to *a*- and *c*-axis, respectively. Average FWHMs of rocking curves are ~ 0.15° (//*a*) and ~ 0.27° (//*c*), much smaller than those of planar templates in both directions. It indicates significant improvement in the structural quality.

μ-PL and μ-RL

ELO *m*-plane GaN samples have been characterized by LT (T = 4K) μ-PL on both mask and window areas. The typical spectra are presented in figure 3.4.3 (a). In the window area, the spectrum is quite similar to that of planar template in the sense that it is still dominated by the emission peak near 3.43 eV, which is associated with BSFs. The peak related to NBE at ~ 3.47 eV appears as a shoulder on the BSF peak. The peak at 3.32 eV is associated either with the PSFs or with the stair-rod dislocations at the intersection between BSFs and PSFs.[71]

Spectrum measured on the mask area is dominated by the NBE-related peak at ~ 3.47 eV. The intensity of BSFs-related peak gets much lower, indicating defect reduction. Furthermore, high resolution spectrum [figure 3.4.3 (b)] reveals that NBE peak are actually made of two peaks: the neutral donor bound exciton (D^0,X_A) at 3.471 eV and the free-exciton X_A at 3.478 eV. The energy of X_A peak suggests that ELO *m*-plane GaN layer is free of strain. This is not surprising as the layer is quite thick (~ 20 μm) and thus is likely to be fully relaxed. The free exciton position is confirmed by μ-RL spectrum, though it is difficult to tell precisely the RL peak position because of the inhomogeneous broadening.

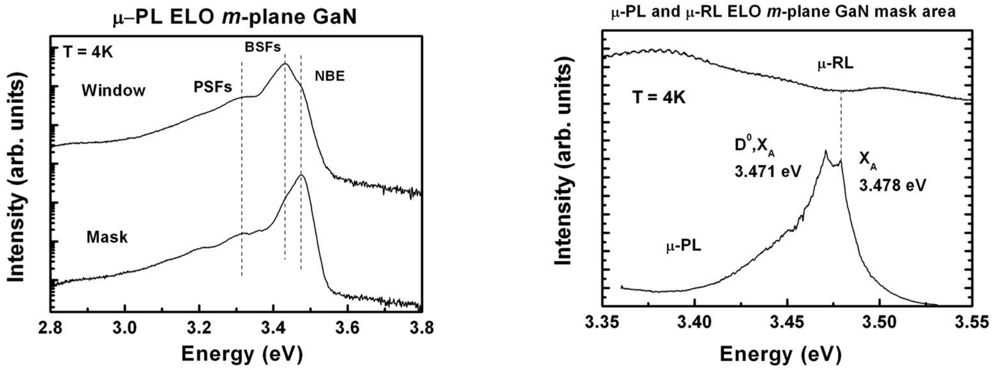

Figure 3.4.3 LT (T = 4K) (a) μ-PL spectra of *m*-plane GaN ELO template on both window and mask areas; (b) μ-PL and μ-RL on mask area.

CL[§§]

LT (T = 32 K) CL scans have been performed on one fully-coalesced ELO sample at wavelength of 357, 362, and 373 nm, as shown in figure 3.4.4 (a)–(c), respectively. They correspond to the emission peak of 3.47 (NBE), 3.43 (BSF), and 3.32 eV in figure 3.4.3 (a). By comparing these three images, it appears that the defect density in the mask areas is lower than that in the window areas, since the defects-related emissions are much brighter in windows. It confirms an effective defect reduction in the mask area by means of ELO technique. High-density defects are introduced where the lateral fronts coalesce, as marked by the arrows in (a). Besides, by comparing figure 3.4.3 (b) and (c), one can see a strong correlation between BSF-related peak at 3.43 eV and the emission peak at 3.32 eV. It suggests that the emission peak at 3.32 eV is maybe related to PSF or the stair-rod dislocation where BSF and PSF meet.

[§§] The CL measurements have been performed by P. Corfdir at LOEQ, EPFL.

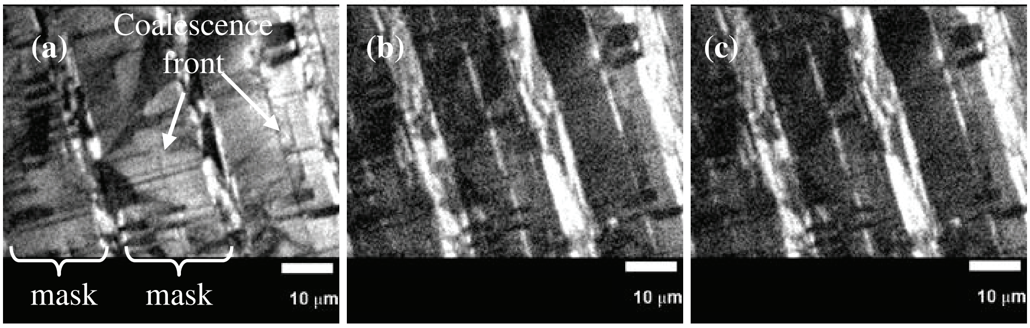

Figure 3.4.4 LT (T= 32 K) CL maps of a fully-coalesced ELO *m*-plane GaN with an acceleration voltage of 8 kV, taken at the recombination energy of (a) 3.47 (b) 3.43 and (c) 3.32 eV, respectively. The mask areas and the coalescence front are marked in (a). (By courtesy of P. Corfdir at LOEQ EPFL)

3.4.3 Summary

ELO technique has been applied to patterned *m*-plane GaN templates. Two aspects are addressed:

(1) Inversion domains, *i.e.* in-plane non-unique polarities, have a negative impact on ELO morphology. This detrimental effect can be alleviated by increasing surface mobility through pressure reduction.

(2) Material quality in the mask areas is improved in terms of surface smoothness, structural and optical properties, compared to the windows. Although TEM results are not available here, the densities of BSFs and TDs are believed to be similar to those of *a*-plane ELO templates. Therefore, overgrown ELO GaN templates are good candidate for the fabrication of nanostructures.

3.5 Summary

This chapter describes both the HVPE growth and the characterizations of *a*- and *m*-plane GaN planar and ELO templates on *r*- and *m*-plane sapphire substrates, respectively.

For planar templates:
A-plane GaN epilayers can be grown on *r*-plane sapphire substrates by either single-step, two-step, or P-V methods. It is found in single-step growth that the surface morphology is highly pressure-dependent. P-V method is thus developed to take advantage of this characteristic and moderate improvement in material quality is achieved. Two-step method fails to significantly improve the material quality as in the case of *c*-plane, due to a lack of effective NL evolution where large GaN crystal islands form.

Three GaN orientations (two semi-polar and one non-polar) can be grown on *m*-plane sapphire. *M*-plane GaN epilayers is obtained by the two-step method with a specific sapphire surface treatment prior to the growth. Surface chemistry is suggested to be the main cause that leads to this crystal orientation.

Both *a*- and *m*-plane GaN planar templates are featured by (a) strong in-plane growth anisotropy and (b) high-density BSFs and TDs. Particularly, *m*-plane GaN surface is featured by “slate-like” morphology, due to protruding steps introduced by BSFs.

For ELO templates:
A- and *m*-plane ELO templates have been obtained. The mask stripes should always be perpendicular to GaN *c*-axis to avoid BSFs propagating into the mask area. The surface roughness in the mask area is close to that of *c*-plane. A significant reduction of defect density has been achieved. The overall material quality in +*c* wing mask area is close to that of *c*-plane and is thus good enough as substrates for the fabrication of nanostructures.

Biblography

---

[1] K. Uchida, A. Watanabe, F. Yano, M. Kouguchi, T. Tanaka, and S. Minagawa, “Nitridation process of sapphire substrate surface and its effect on the growth of GaN”, *Journal of Applied Physics*, vol. 79, no. 7, pp. 3487-3491, 1996.

[2] M. Huth, K. A. Ritley, J. Oster, H. Dosch, and H. Adrian, “Highly ordered Fe and Nb stripe arrays on facetted α-Al2O3$(10\bar{1}0)$”, *Advanced Functional Materials*, vol. 12, no. 5, pp. 333-338, 2002.

[3] S. Hussy, E. Meissner, B. Birkmann, I. Brauer, J. Off, F. Scholtz, H.P. Strunk, and G. Müller, “Morphology and microstructure of a-plane GaN players grown by MOVPE and by low pressure solution growth (LPSG)”, *physica. status. solidi. (a)*, vol. 203, no. 7, pp. 1676-1680, 2006.

[4] E. Ejder, “Growth and morphology of GaN”, *Journal of Crystal Growth*, vol. 22, no. 1, pp. 44-46, 1974.

[5] D. Elwell, R. S. Feigelson, M. M. Simkins, and W. A. Tiller, “Crystal growth of GaN by the reaction between gallium and ammonia”, *Journal of Crystal Growth*, vol. 66, no. 1, pp. 45-54, 1984.

[6] K. Hiramatsu, K. Nishiyama, A. Motogaito, H. Miyake, Y. Iyechika, and T. Maeda, “Recent progress in selective area growth and epitaxial lateral overgrowth of III-nitrides: effects of reactor pressure in MOVPE growth”, *physica. status. solidi. (a)*, vol. 176, no. 1, pp. 535-543, 1999.

[7] F. Wu, M. D. Craven, S. –H. Lim, and J. S. Speck, “Polarity determination of a-plane GaN on r-plane sapphire and its effects on lateral overgrowth and heteroepitaxy”, *Journal of Applied Physics*, vol. 94, no. 2, pp. 942-947, 2003.

[8] B. A. Haskell, F. Wu, S. Matsuda, M. D. Craven, P. T. Fini, S. P. DenBaars, J. S. Speck, and S. Nakamura, “Structural and morphological characteristic of planar $(11\bar{2}0)$ *a*-plane gallium nitride grown by hydride vapor phase epitaxy”, *Applied Physics Letters*, vol. 83, no. 8, pp. 1554-1556, 2003.

[9] M. D. Craven, S. H. Lim, F. Wu, J. S. Speck, and S. P. DenBaars, “Structural characterization of nonpolar $(11\bar{2}0)$ a-plane GaN thin films grown on $(1\bar{1}02)$ r-plane sapphire”, *Applied Physics Letters*, vol. 81, no. 3, pp. 469-471, 2002.

[10] H. Wang, C. Chen, Z. Gong, J. Zhang, M. Gaevski, M. Su, J. Yang, and M. A. Khan, “Anisotropic structural characteristics of $(11\bar{2}0)$ GaN templates and coalesced epitaxial lateral overgrown films deposited on $(10\bar{1}2)$ sapphire”, *Applied Physics Letters*, vol. 84, no. 4, pp. 499-501, 2004.

[11] X. Ni, Y. Fu, Y. T. Moon, N. Biyikli, and H. Morkoç, “Optimization of $(11\bar{2}0)$ *a*-plane GaN growth by MOCVD on $(1\bar{1}02)$ *r*-plane sapphire”, *Journal of Crystal Growth*, vol. 290, no. 1, pp. 166-170, 2006.

[12] A. Kobayashi, S. Kawano, K. Ueno, J. Ohta, H. Fujioka, H. Amanai, S. Nagao, and H. Horie, “Growth of a-plane GaN on lattice-matched ZnO substrates using a room-temperature buffer layer”, *Applied Physics Letters*, vol. 91, no. 19, pp. 191905-1-3, 2007.

[13] M. D. Craven, F. Wu, A. Chakraborty, B. Imer, U. K. Mishra, S. P. DenBaars, and J. S. Speck, "Microstructural evolution of *a*-plane GaN grown on *a*-plane SiC by metalorganic chemical vapor deposition", *Applied Physics Letters*, vol. 84, no. 8, pp. 1281-1283, 2004.

[14] L. Lymperakis and J. Neugebauer, "Large anisotropic adatom kinetics on nonpolar GaN surfaces: consequences for surface morphologies and nanowire growth", *Physical Review B*, vol. 79, no. 24, pp. 241308(R), 2009.

[15] T. Lei, K. F. Ludwig Jr., T. D. Moustakas, "Heteroepitaxy, polymorphism, and faulting in GaN thin films on silicon and sapphire substrates", *Journal of Applied Physics*, vol. 74, no. 7, pp. 4430-4437, 1993.

[16] S. Hearne, E. Chason, J. Han, J. A. Floro, J. Figiel, J. Hunter, H. Amano, and I. S. T. Tsong, "Stress evolution during metalorganic chemical vapor deposition of GaN", *Applied Physics Letters*, vol. 74, no. 3, pp. 356-358, 1999.

[17] T. Böttcher, S. Einfeldt, S. Figge, R. Chierchia, H. Heinke, D. Hommel, and J. S. Speck, "The role of high-temperature island coalescence in the development of stresses in GaN films", *Applied Physics Letters*, vol. 78, no. 14, pp. 1976-1978, 2001.

[18] J. Napierala, D. Martin, N. Grandjean, and M. Ilegems, "Stress control in GaN/sapphire templates for the fabrication of crack-free thick layers", *Journal of Crystal Growth*, vol. 289, no. 2, pp. 445-449, 2006.

[19] B. W. Sheldon, K. H. A. Lau, and A. Rajamani, "Intrinsic stress, island coalescence, and surface roughness during the growth of polycrystalline films", *Journal of Applied Physics*, vol. 90, no. 10, pp. 5097-5103, 2001.

[20] Z. Liliental-Weber and D. N. Zakharov, "Defects formed in nonpolar GaN grown on SiC and Al2O3 and their reduction in pendeo-epitaxial and laterally overgrown GaN layers", Book contribution in: *Nitrides with Nonpolar Surfaces* (Ed. T Paskova), Wiley VCH Verlag (2008)

[21] M. Matumi, F. Satoh, Y. Kumagai, K. Takemoto, and A. Koukitu, "Thermodynamic analysis and in situ gravimetric monitoring of GaN decomposition", *Proceedings of International Workshop on Nitride Semiconductors*, 38-41, 2000.

[22] A. Koukitu, S. Hama, T. Taki, and H. Seki, "Thermodynamic analysis of hydride vapor phase epitaxy of GaN", *Japanese Journal of Applied Physics*, vol. 37, no. 3A, pp. 762-765, 1998.

[23] E. Aujol, A. Trassoudaine, L. Siozade, A. Pimpinelli, R. Cadoret, "Hydrogen and nitrogen ambient effects on epitaxial growth of GaN by hydride vapor phase epitaxy", *Journal of Crystal Growth*, vol. 230, no. 3-4, pp. 372-376, 2001.

[24] D. D. Koleske, A. E. Wickenden, R. L. Henry, J. C. Culbertson, M. E. Twigg, "GaN decomposition in H_2 and N_2 at MOVPE temperatures and pressures", *Journal of Crystal Growth*, vol. 223, no. 4, pp. 466-483, 2001.

[25] X. H. Wu, D. Kapolnek, E. J. Tarsa, B. Heying, S. Keller, B. P. Keller, U. K. Mishra, S. P. DenBaars, and J. S. Speck, "Nucleation layer evolution in metal-organic chemical vapor deposition grown GaN", *Applied Physics Letters*, vol. 68, no. 10, pp. 1371-1373, 1996.

---

[26] K. Lorenz, M. Gonsalves, W. Kim, V. Narayanan, and S. Mahajan, “Comparative study of GaN and AlN nucleation layers and their role in growth of GaN on sapphire by metalorganic chemical vapor deposition”, *Applied Physics Letters*, vol. 77, no. 21, pp. 3391-3393, 2000.

[27] S. Gradečak, P. Stadelmann, V. Wagner, and M. Ilegems, “Bending of dislocations in GaN during epitaxial lateral overgrowth”, *Applied Physics Letters*, vol. 85, no. 20, pp. 4648-4850, 2004.

[28] D. D. Koleske, M. E. Coltrin, K. C. Cross, C. C. Mitchell, and A. A. Allerman, “Understanding GaN nucleation layer evolution on sapphire”, *Journal of Crystal Growth*, vol. 273, no. 1, pp. 86-99, 2004.

[29] T. Paskova, V. Darakchieva, P. P. Paskov, J. Birch, E. Valcheva, P. O. A. Persson, B. Arnaudov, S. Tungasmitta, and B. Monemar, “Properties of nonpolar a-plane GaN films grown by HVPE with AlN buffers”, *Journal of Crystal Growth*, vol. 281, no. 1, pp. 55-61, 2005.

[30] M. Moram, C. F. Johnson, J. L. Hollander, M. J. Kappers, and C. J. Humphreys, “Understanding x-ray diffraction of nonpolar gallium nitride films”, *Journal of Applied Physics*, vol. 105, no. 11, pp. 113501, 2009.

[31] T. Paskova, R. Kroeger, S. Figge, D. Hommel, V. Darakchieva, B. Monemar, E. Preble, A. Hanser, N. M. Williams, and M. Tutor, “High-quality bulk *a*-plane GaN sliced from boules in comparison to heteroepitaxially grown thick films on *r*-plane sapphire”, *Applied Physics Letters*, vol. 89, no. 5, pp. 051914-1-3, 2006.

[32] C. Roder, S. Einfeldt, S. Figge, T. Paskova, D. Hommel, P. P. Paskov, B. Monemar, U. Behn, B. A. Haskell, P. T. Fini, and S. Nakamura, “Stress and wafer bending of *a*-plane GaN layers on *r*-plane sapphire substrates”, *Journal of Applied Physics*, vol. 100, no. 10, pp. 103511, 2006.

[33] B. Heying, X. H. Wu, S. Keller, Y. Li, D. Kapolnek, B. P. Keller, S. P. DenBaars, and J. S. Speck, “Role of threading dislocation structure on the x-ray diffraction peak widths in epitaxial GaN films”, *Applied Physics Letters*, vol. 68, no. 5, pp. 643-645, 1996.

[34] E.V. Etzkorn and D. R. Clarke, “Cracking of GaN films”, *Journal of Applied Physics*, vol. 89, no. 2, pp. 1025-1034, 2001.

[35] D. N. Zakharov, Z. Liliental-Weber, B. Wagner, Z. J. Reitmeier, E. A. Preble, and R. E. Davis, “Structural TEM study of nonpolar *a*-plane gallium nitride grown on $(11\bar{2}0)$ *4H*-SiC by organometallic vapor phase epitaxy”, *Physical Review B*, vol. 71, no. 23, pp. 235334, 2005.

[36] C. Stampfl and C. G. Van de Walle, “Energetics and electronic structure of stacking faults in AlN, GaN, and InN”, *Physcial Review B*, vol. 57, no. 24, R15052-15055, 1998.

[37] X. H. Wu, L. M. Brown, D. Kapolnek, S. Keller, B. Keller, S. P. DenBaars, and J. S. Speck, “Defect structure of metal-organic chemical vapor deposition-grown epitaxial (0001) GaN/Al_2O_3”, *Journal of Applied Physics*, vol. 80, no. 6, pp. 3228-3237, 1996.

[38] P. P. Paskov, R. Schifano, B. Monemar, T. Paskova, S. Figge, and D. Hommel, “Emission properties of a-plane GaN grown by metal-organic chemical-vapor deposition”, *Journal of Applied Physics*, vol. 98, no. 9, pp. 092519-1-7, 2005.

---

[39] D. Du, D. J. Srolovitz, M. E. Coltrin, and C. C. Mitchell, “Systematic prediction of kinetically limited crystal growth morphologies”, *Physical Review Letters*, vol. 95, no. 15, pp. 155503, 2005.

[40] M. D. Craven, S. H. Lim, F. Wu, J. S. Speck, and S. P. DenBaars, “Threading dislocation reduction via laterally overgrown nonpolar $(11\bar{2}0)$ *a*-plane GaN”, *Applied Physics Letters*, vol. 81, no. 7, pp.1201-1203, 2002.

[41] P. Corfdir, P. Lefebvfre, J. Levrat, A. Dussaigne, J.-D. Ganière, D. Martin, J. Ristic, T. Zhu, N. Grandjean, and B. Deveaud-Plédran, “ Exciton localization on basal stacking faults in a-plane epitaxial lateral overgrown GaN grown by hydride vapor phase epitaxy”, *Journal of Applied Physics*, vol. 105, no. 4, pp. 043102, 2009.

[42] T. Gühne, Z. Bougrioua, P. Vennégués, and M. Leroux, “Cathodoluminescence spectroscopy of epitaxial-lateral-overgrown nonpolar (11-20) and semipolar (11-22) GaN in relation to microstructural Characterization”, *Journal of Applied Physics*, vol. 101, no. 11, pp. 113101, 2007.

[43] Z. Liliental-Weber, “TEM studies of GaN layers grown in non-polar direction: laterally overgrown nd pendeo-epitaxial layers”, *Journal of Crystal Growth*, vol. 310, pp. 4011-4015, 2008.

[44] X. Ni, Ü. Özgür, H. Morkoç, Z. Liliental-Weber, H. O. Everitt, “Epitaxial lateral overgrowth of a-plane GaN by metalorganic chemical vapor deposition”, *Journal of Applied Physics*, vol. 102, no. 05, pp. 053506, 2007.

[45] J.-J. Huang, K.-C. Shen, W.-Y. Shiao, Y.-S. Chen, T.-C. Liu, T.-Y. Tang, C.-F. Huang, and C. C. Yang, “Improved a-plane GaN quality grown with flow modulation epitaxy and epitaxial lateral overgrowth on r-plane sapphire substrate”, *Applied Physics Letters*, vol. 92, no. 23, pp. 231902, 2008.

[46] A. E. Romanov, P. Fini, and J. S. Speck, “Modeling the extended defect evolution in lateral epitaxial overgrowth of GaN: subgrain stability”, *Journal of Applied Physics*, vol. 93, no. 1, pp. 106-114, 2003.

[47] P. Waltereit, O. Brandt, M. Ramsteiner, R. Uecker, P. Reiche, and K.H. Ploog, “Growth of m-plane GaN$(1\bar{1}00)$ on γ-LiAlO$_2$(100)”, *Journal of Crystal Growth*, vol. 218, no. 2-4, pp. 143-147, 2000.

[48] B. A. Haskell, A. Chakraborty, F. Wu, H. Sasano, P. T. Fini, S. P. DenBaars, J. S. Speck, and S. Nakamura, “Microstructure and enhanced morphology of planar nonpolar *m*-plane GaN grown by hydride vapor phase epitaxy”, *Journal of Electronic Materials*, vol. 34, no. 4, pp. 357-360, 2005.

[49] A. Kobayashi, S. Kawano, Y. Kawaguchi, J. Ohta, and H. Fujioka, “Room temperature epitaxial growth of *m*-plane GaN on lattice-matched ZnO substrates”, *Applied Physics Letters*, vol. 90, no. 4, pp. 041908, 2007.

[50] R. Armitage, M. Horita, J. Suda, and T. Kimoto, “*m*-plane GaN layers grown by rf-plasma assisted molecular beam epitaxy with varying Ga/N flux ratios on m-plane 4H-SiC substrates”, *Journal of Applied Physics*, vol. 101, no. 3, pp. 033534, 2007.

[51] B. Imer, F. Wu, M. D. Craven, J. S. Speck, and S. P. DenBaars, “Stability of $(1\bar{1}00)$ m-plane GaN films grown by metalorganic chemical vapor deposition”, *Japanese Journal of Applied Physics*, vol. 45, no. 11, pp. 8644-8647, 2006.

[52] R. Armitage and H. Hirayama, “*M*-plane GaN grown on *m*-sapphire by metalorganic vapor phase epitaxy”, *Applied Physics Letters*, vol. 92, no. 9, pp. 092121, 2008.

[53] T. J. Baker, B. A. Haskell, F. Wu, J. S. Speck, and S. Nakamura, “Characterization of planar semipolar gallium nitride films on sapphire substrates”, *Japanese Journal of Applied Physics*, vol. 45, no. 6, pp. L154-L157, 2006.

[54] J. R. Heffelfinger, M. W. Bench, and C. Barry Carter, “On the faceting of ceramic surfaces”, *Surface Science*, vol. 343, no. 1-2, pp. L1161-1166, 1995.

[55] H. Amano, N. Sawaki, I. Akasaki, and Y. Toyoda, “Metalorganic vapor phase epitaxial growth of a high quality GaN film using an AlN buffer layer”, *Applied Physics Letters*, vol. 48, no. 5, pp. 353-355, 1986.

[56] M. Tsuda, K. Watanabe, S. Kamiyama, H. Amano, and I. Akasaki, “The surface treatment of sapphire substrate and its effects on the initial stage of GaN growth by MOVPE”, *phys. stat. sol.* (c), vol. 0, no. 7, pp. 2163–2166, 2003.

[57] N. Grandjean, J. Massies, and M. Leroux, “Nitridation of sapphire. Effect of the optical properties of GaN epitaxial overlayers”, *Applied Physics Letters*, vol. 69, no. 14, pp. 2071-2073, 1996.

[58] T. Hashimoto, Y. Terakoshi, M. Yuri, M. Ishida, O. Imafuji, T. Sugino, and K. Itoh, “Quantitative study of nitridated sapphire surfaces by x-ray photoelectron spectroscopy”, *Journal of Applied Physics*, vol. 86, no. 7, pp. 3670-3675, 1999.

[59] F. Dwikusuma and T. F. Kuech, “X-ray photoelectron spectroscopic study on sapphire nitridation for GaN growth by hydride vapor phase epitaxy: nitridation mechanism”, *Journal of Applied Physics*, vol. 94, no. 9, pp. 5656-5664, 2003.

[60] T. Wei, R. Duan, J. Li, Z. Huo, J. Yang, and Y. Zeng, “Microstructure and optical properties of nonpolar m-plane GaN films grown on m-plane sapphire by hydride vapor phase epitaxy”, *Japanese Journal of Applied Physics*, vol. 47, no. 5, pp. 3346-3349, 2008.

[61] P. Vennéguès, Z. Bougrioua, and T. Gühne, “Microstructural characterization of semipolar GaN templates and epitaxial-lateral-overgrowth films deposited on m-plane sapphire by metalorganic vapor phase epitaxy”, *Japanese Journal of Applied Physics*, vol. 46, no. 7A, pp. 4089-4095, 2007.

[62] J. Oster, M. Kallmayer, L. Wiehl, H. J. Elmers, H. Adrian, F. Porrati, and M. Huth, “Crystallography, morphology, and magnetic properties of Fe nanostructures on faceted α-Al_2O_3 m-plane”, *Journal of Applied Physics*, vol. 97, no. 1, pp. 014303, 2005.

[63] K-C Kim, M. C. Schmidt, F. Wu, M. B. McLaurin, A. Hirai, S. Nakamura, S. P. DenBaars, and J. S. Speck, “Low extended defect density nonpolar m-plane GaN by sidewall lateral epitaxial overgrowth”, *Applied Physics Letters*, vol. 93, no. 14, pp. 142108, 2008.

---

[64] A. Hirai, B. A. Haskell, M. B. McLaurin, F. Wu, M. C. Schmidt, K. C. Kim, T. J. Baker, S. P. DenBaars, S. Nakamura, and J. S. Speck, “Defect-mediated surface morphology of nonpoalr *m*-plane GaN”, *Applied Physics Letters*, vol. 90, no. 12, pp. 121119, 2007.

[65] J. Kioseoglou, G. P. Dmitrakopulos, H. M. Polatoglou, L. Lymperakis, G. Nouet, and Ph. Komninou, “Atomic-scale models of interactions between inversion domain boundaries and intrinsic basal stacking faults in GaN”, *Diamond and Related Materials*, vol. 11, pp. 905-909, 2002.

[66] F. Habel, P. Bruckner, J. Tsay, W. Liu, F. Scholz, D. Schmitz, A. Alam, and M. Heuken, “Hydride vapor phase epitaxial growth of thick GaN layers with improved surface flatness”, *phys. stat. sol. (c)*, vol. 2, no. 7, pp. 2049-2052, 2005.

[67] A. Hirai, Z. Jia, M. C. Schmidt, R. M. Farrell, S. P. DenBaars, S. Nakamura, J. S. Speck, and K. Fujito, “Formation and reduction of pyramidal hillocks on m-plane $\{1\bar{1}00\}$ GaN”, *Applied Physics Letters*, vol. 91, no. 19, pp. 191906, 2007.

[68] T. Moriyama and S. Fujita, “Growth behavior of nonpolar ZnO on *m*-plane and *r*-plane sapphire by metalorganic vapor phase epitaxy”, *Journal of Applied Physics*, vol. 44, no. 11, pp. 7919-7921, 2005.

[69] P. Vennéguès, T. Zhu, J. M. Chauveau, Z. Bougrioua, D. Martin, J. Zuniga-Perez and N. Grandjean, “In-plane polarities of nonpolar wurtzite epitaxial films deposited on M- and R-plane sapphire substrates”, *Japanese Journal of Applied Physics*, vol. 48, no. 9, pp. 090211, 2009.

[70] M. B. McLaurin, A. Hirai, E. Young, F. Wu, and J. S. Speck, “Basal plane stacking-fault related anisotropy in X-ray rocking curve widths of *m*-plane GaN”, *Japanese Journal of Applied Physics*, vol. 47, no. 7, pp. 5429-5431, 2008.

[71] R. Liu, A. Bell, F. A. Ponce, C. Q. Chen, J. W. Yang, and M. A. Khan, “Luminescence from stacking faults in gallium nitride”, *Applied Physics Letters*, vol. 86, no. 2, pp. 021908, 2005.

[72] F. Scholz, P. Bruckner, F. Habel, M. Peter, and K. Kohler, “Improved GaN layer morphology by hydride vapor phase epitaxy on misoriented Al_2O_3 wafers”, *Applied Physics Letters*, vol. 87, no. 18, pp. 181902, 2005.

[73] S. Keller, N. A. Fichtenbaum, F. Wu, D. Brown, A. Rosales, S. P. DenBaars, J. S. Speck, and U. K. Mishra, “Influence of the substrate misorientation on the properties of N-polar GaN films grown by metal organic chemical vapor deposition”, *Journal of Applied Physics*, vol. 102, no. 08, pp. 083546, 2007.

4. MBE growth of non-polar III-Nitrides

In the beginning, MBE had been planned to grow only nanostructures on ELO templates prepared by HVPE. However, since NH_3-source MBE growth experience of non-polar nitrides was lacking in our laboratory, some preliminary work has also been carried out and is reported altogether. In this chapter, homo- and heteroepitaxy of nonpolar GaN layers are discussed in sections 4.1 and 4.2, respectively. Investigations of nanostructures like single QWs and more complex ones (*e.g.* distributed Bragg reflectors and microcavities) are presented in sections 4.3 and 4.4.

4.1 Homoepitaxy of *a*- and *m*-plane GaN

Homoepitaxy is a shortcut to understand how the growth parameters influence the crystal habits. For *a*-plane the growth was performed on ELO templates, while for *m*-plane the growth was performed on planar templates.

4.1.1 Homoepitaxy of *a*-plane GaN on HVPE ELO non-coalesced templates

As demonstrated in section 3.1, *a*-plane GaN has a narrow growth window since other planes like $\{1\bar{1}01\}$ are more stable under N-rich conditions. To understand the effects of temperature and V/III ratio, *a*-plane GaN epilayers have been deposited on several non-coalesced HVPE ELO templates as summarized in table 4.1. The growth rate is ~ 0.6 μm/h and layer thickness is about 1 μm for all six samples. Top-view Nomarski optical micrographs of samples A-F are presented in figures 4.1.1 (a) – (f), respectively, with identical size of 120 × 105 μm^2. Note there are two mask patterns: window 5 μm + mask 10 μm for samples A, C, and D, and window 5 μm + mask 45 μm for samples B, E, and F.

Sample Mask patterns	A (5/10 μm)	B (5/45 μm)	C (5/10 μm)	D (5/10 μm)	E (5/45 μm)	F (5/45 μm)
T_g (°C)	870	870	820	820	770	770
NH_3 flux (sccm)	80	60	80	60	80	60

Table 4.1 Homoepitaxy of *a*-plane GaN by MBE on HVPE ELO templates with different growth temperatures and NH_3 fluxes (V/III ratio).

Strong in-plane growth anisotropy has been observed, as +*c* plane grows faster than –*c* plane. For example, the inset in figure 4.1.1 (d) is a SEM cross-section image, where the dash-line indicates the interface of HVPE/MBE grown materials. For the MBE-grown layer of sample D, the growth rate of [0001] direction seems even larger than that of $[11\bar{2}0]$ direction, as the lateral extentsion overhangs like an eave. Such eave-like morphology is found in all six samples, though it is hardly visible for samples E and F since the extent of lateral growth decreases with the reduction of growth temperature. Besides, ellipsoidal features that are elongated along *c*-axis can be clearly observed when T_g = 870 °C and 820 °C, whereas they are difficult to identiy for T_g = 770 °C. In other words, high temperature promotes lateral growth in +*c* direction and reinforces growth anisotropy. In comparison, the variation of NH_3 flux (*i.e.* V/III ratio) does not seem to change drastically the macro-scale morphology. Besides, there are micrometer-scale GaN inclusions randomly distributed over the surface. Inset in figure 4.1.1 (c) provides an enlarged view of the surface by SEM, where these inclusions are actually polycrystalline crystals. Their origin is linked to contanminations unintentionally introduced during the sample preparation, *i.e.* when a 2-inch wafer is cut into quarters by wafer dicing saw. This problem has been solved in later work by protecting the substrate surface with a thin film of photoresist. On the micro-scale, rms roughness (5 × 5 μm^2) is about 4 – 5 nm for all the samples, measured by AFM in mask areas free of inclusions. It is about one magnitude higher than that of HVPE ELO templates (~ 0.4 nm as mentioned in section 3.2.2), probably due to the kinetic roughening, which is usually observed in MBE-grown *c*-plane GaN under N-rich conditions.[1]

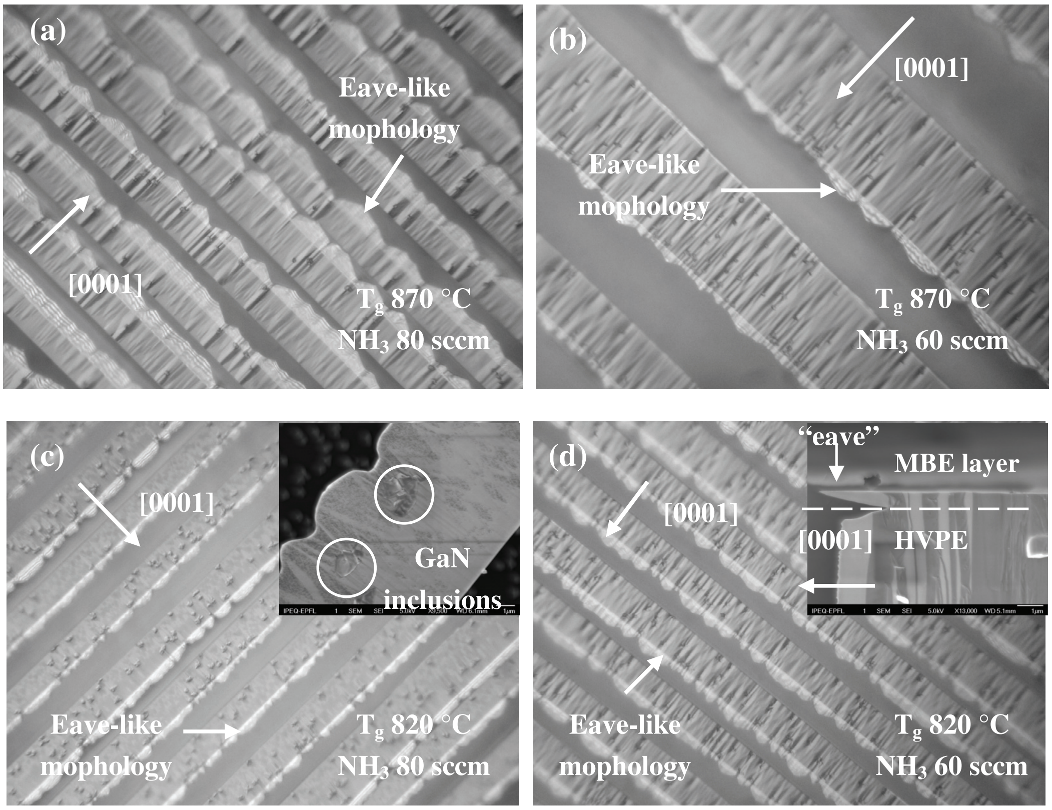

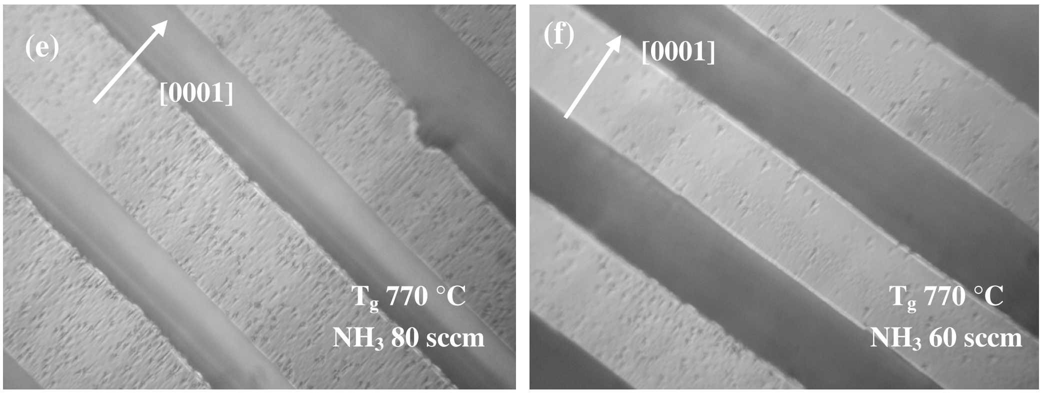

Figure 4.1.1 (a) – (f) are top-view Nomarski optical micrographs (120 × 105 μm^2) of samples A-F, respectively. Inset in (c) is a top-view SEM image for sample C, where the circles mark the GaN particales. Inset in (d) is a cross-section SEM image of sample D, where the arrow indicates the lateral extention "eave" in [0001] direction.

4.1.2 Homoepitaxy of *m*-plane GaN on HVPE planar templates

As discussed in section 3.3, *m*-plane can be grown with similar conditions of those used for *c*-plane by HVPE. As for MBE, certain fine-tuning of T_g and V/III ratio has been tested, with constant growth rate ~ 0.65 ML/s. Their surface morphology is shown in figure 4.1.2, together with T_g and NH_3 flux values. Figure 4.1.2 (a) is the reference HVPE planar template, with rms ~ 6 nm (10 × 10 μm^2). The surface is featured by slate-like morphology along $[11\bar{2}0]$ *a*-axis and terraces, as described in section 3.3. Figures 4.1.2 (b) and (c) correspond to MBE homoepitaxial layer with T_g of 830 and 800 °C, repectivley, with NH_3 flux of 80 sccm. Elongated mound-like features along *a*-axis can be found on both samples. Their rms roughnesses increase to (b) 10 and (c) 15 nm (10 × 10 μm^2), respectively. This surface roughening has a kinetic origin: MBE growth temperature is lower than MOVPE/HVPE, so the species diffusion length is lower and the surface is not as close to thermodynamic equilibrium as that of MOVPE/HVPE.[1] Rms of (b) is lower than that of (c), because T_g of (b) is slightly higher than that of (c). This argument is supported by the observation that further reduction of T_g below 800 °C leads to a deterioration of RHEED streaky patterns (not shown here).

By comparing figures (c) and (d), which correspond to same T_g (800 °C) but different NH_3 flux (80 vs. 60 sccm), one can see that the micro-scale morphologies are quite different. With the decrease of V/III ratio, other crystal facets appear in the form of pyramidal hillocks [figure 4.1.2 (d)]. A possible explanation is that lower NH_3 flux increases the Ga diffusion length and thus favors the formation of facets with lower surface energy. Higher T_g has similar effect, which is in agreement with the observation in (b).

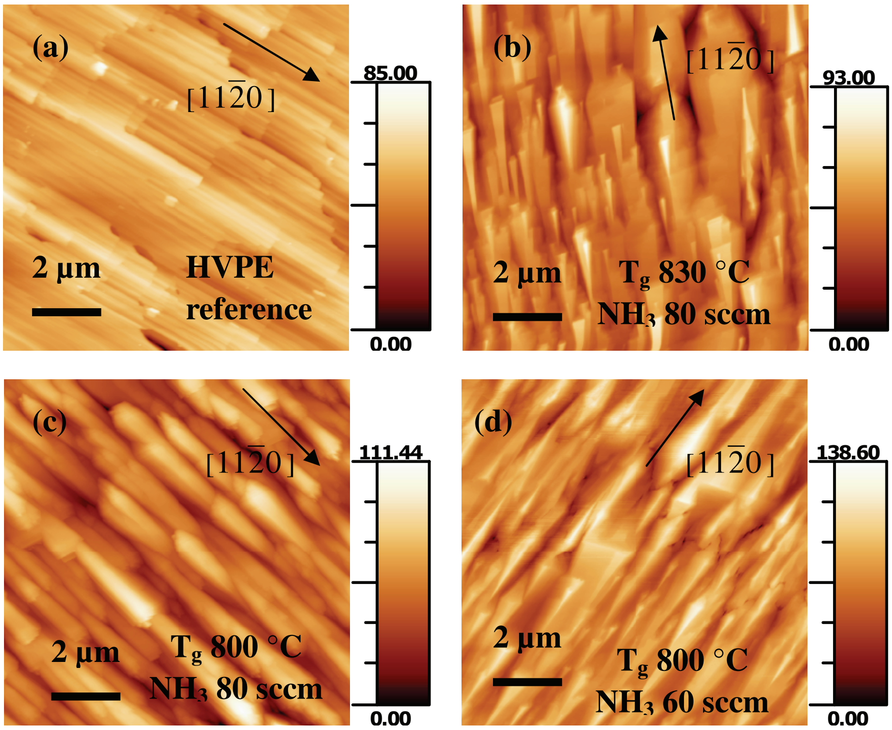

Figure 4.1.2 AFM images (10 × 10 µm^2) for (a) reference HVPE *m*-plane GaN planar template; (b) –(d) are MBE homoepitaxy layers with various T_g and NH_3 flux.

In summary, kinetic roughening occurs during homoepitaxy of non-polar GaN by MBE, similar to what is observed on *c*-plane. For *a*-plane, the growth anisotropy is promoted by higher temperature, while change in V/III ratio does not have a significant impact. For *m*-plane, the optimal growth conditions are similar to those used for *c*-plane. Lower V/III ratio or higher temperature introduces additional faceting and thus should be avoided

4.2 Heteroepitaxy of *a*-plane GaN on *r*-plane sapphire

The growth procedure of *c*-plane GaN on *c*-plane sapphire by NH_3-source MBE resembles that of MOVPE in a way that a LT (T ~ 500 °C) NL is first deposited and followed by a HT (T ~ 800 °C) growth.[2] The conventional HT growth conditions for *c*-plane GaN are substrate temperature of 800 °C, NH_3 flux of 80 sccm, and growth rate of ~ 1 ML/s (~ 0.93 µm/h). For *a*-plane GaN, references on NH_3-source MBE are lacking.

Recall that *a*-plane GaN can be grown on *r*-sapphire by MOVPE and HVPE without using a LT NL, because the defects filtering mechanism of NL recrystallization does not work as effectively for non-polar *a*- and *m*-plane as for polar *c*-plane (section 3.1 and 3.3) Therefore, one-step HT growth procedure has been chosen to investigate the heteroepitaxy.

Before each run, the sapphire substrate was nitridated at 900 °C for 10 min. The surface modification can be observed *in situ* by RHEED, as the corresponding patterns turn into broad streaks, indicating the formation of an AlN layer.[3] A set of growth conditions are summarized in table 4.2. The layer thickness is about 1 μm for all samples. Sample A was grown with the conventional *c*-plane conditions. After a deposition of ~ 50 nm layer, RHEED pattern turned to be spotty, indicating the formation of 3D islands. This observation is confirmed by the AFM image (rms roughness ~ 18 nm), which shows that the surface is fully convered by crystal islands with an average diameter of 250 nm [figure 4.2.1 (a)]. *In situ* LR with a wavelength of 635 nm is not sensitive to such small islands. That is why the signal intensity (red) does not decrease significantly, as shown in figure 4.2.2. Besides, the FWHMs of X-ray ω scan rocking curves recorded on the 1-μm-thick layers are ~ 1° in both the [0001] and $[1\bar{1}00]$ directions, due to the poor structural properties. Thus, the growth conditions for *c*-plane are not applicable for *a*-plane.

Samples	Growth temperature (°C)	Growth rate (μm/h)	Layer thickness (μm)
A	800	~ 0.74	~ 1
B	870	~ 0.77	~ 1
C	T_g^1: 870 T_g^2: 800	~ 0.29 ~ 0.32	~ 0.15 ~ 0.7

Table 4.2 Parameters for one-step growth of GaN on *r*-plane sapphire by NH_3-source MBE. The growth rate and layer thickness are derived from *in situ* LR.

In an attempt to promote the lateral growth, the substrate temperature was raised up to 870 °C (sample B). Initially, RHEED patterns were quasi-streaky. However, after a deposition of ~ 200 nm, the pattern turned to be spotty again, suggesting a growth mode transition from 2D to 3D. The surface turns out to be even rougher than that of sample A, with a rms roughness of ~ 50 nm [figure 4.2.1 (b)]. The island size is in average of 1.5 μm, large enough to significantly reduce the LR signal (blue) in figure 4.2.2. In addition, the FWHMs of X-ray ω scan rocking curves are 0.5–0.7° in the [0001] and $[1\bar{1}00]$ directions, not significantly better than sample A.

Further study reveals that after depositing a ~ 150 nm thin layer at 870 °C (T_g^1), the substrate temperature has to be reduced to ~ 800 °C (T_g^2), in order to keep the patterns streaky (sample C). Besides, the growth rate is reduced in order to increase the diffusion length. The representative RHEED patterns in the $[1\bar{1}00]$ and [0001] azimuth angles are displaced in Figure 4.2.1 (d) and (e), respectively. There are primary-order streaks in the $[1\bar{1}00]$ azimuth, with no signs of surface reconstruction. In the [0001] azimuth, however, chevron tails are observed between two adjacent primary-order streaks. They indicate faceting of the surface.[4] AFM scans reveal the strong growth anisotropy with stripe-feature along [0001] direction [figure 4.2.1 (c)]. The rms roughness is about 12 nm (5 × 5 μm^2). The amplitude of LR oscillations does not decrease that much (black) in figure 4.2.2, due to the small-scale roughness. The FHWMs of XRD ω scan rocking curves are featured by the same anisotropy as reported in section 3.1.4, where their minimum and maximum values are 0.38 and 0.75° along [0001] and [1-100] direction, respectively. This demonstrates a better structural quality, compared to samples A and B.

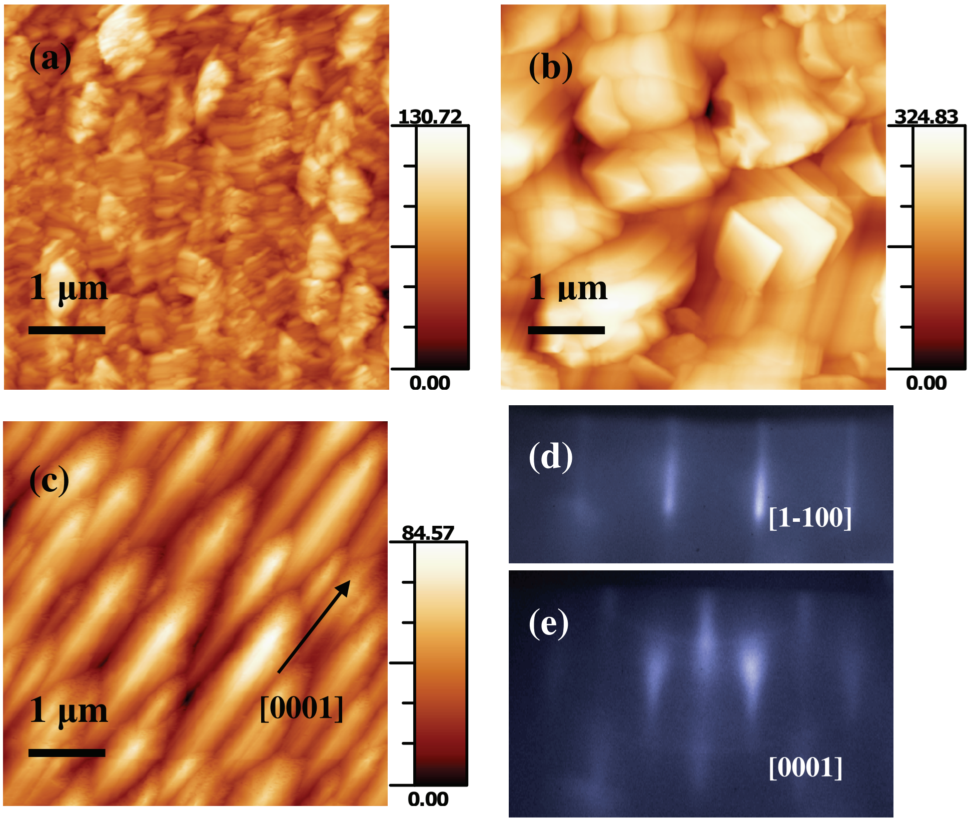

Figure 4.2.1 AFM images (5 × 5 μm^2) for samples (a) A, (b) B, and (c) C, as listed in table 4.2. RHEED patterns of sample C in the azimuth angles of (d) $[1\bar{1}00]$ and (e) [0001], respectively.

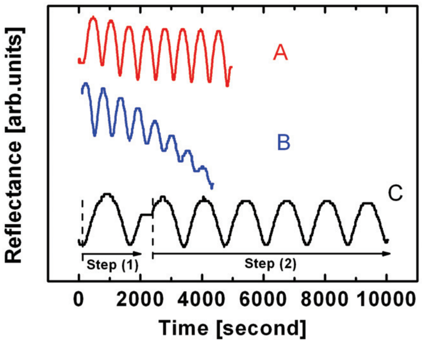

Figure 4.2.2 *in situ* LR record of MBE growth for samples A-C, as listed in table 4.1.

From the above study, it seems that sample C with two–T_g growth method, is appropriate for the heteroepitaxy of *a*-plane GaN. Furthermore, three different growth temperatures have been tested for T_g^2: 800, 760, and 720 °C. XRD FWHMs of ω scan rocking curves measured in the $[1\bar{1}00]$ direction increase from 0.75 to over 1° when T_g^2 decreases from 800 to 720 °C, while in the [0001] direction, FWHMs do not change much. It may arise from the increase of mosaic tilt or dislocation density.[5]

In addition, low temperature (T = 9 K) PL has been performed on these three samples and the spectra are presented in figure 4.2.3. For the sample with T_g^2 = 800 °C, the spectrum is dominated by 3.472 eV luminescence, which is associated with NBE recombination. The FWHM of this peak is ~ 17 meV, still too broad to discriminate the neutral donor bound exciton from the free exciton. The emission peak near 3.42 eV is ascribed to type I_1 BSFs.[6] The emission peak near 3.27 eV is related to the DAP. The emission peaks at 3.18 and 3.09 eV are the LO phonon replicas of DAP. When T_g^2 is decreased to 760 °C, the corresponding spectrum is dominated by DAP luminescence; when it is further down to 720 °C, the peak intensity of BSFs is larger than that of NBE.

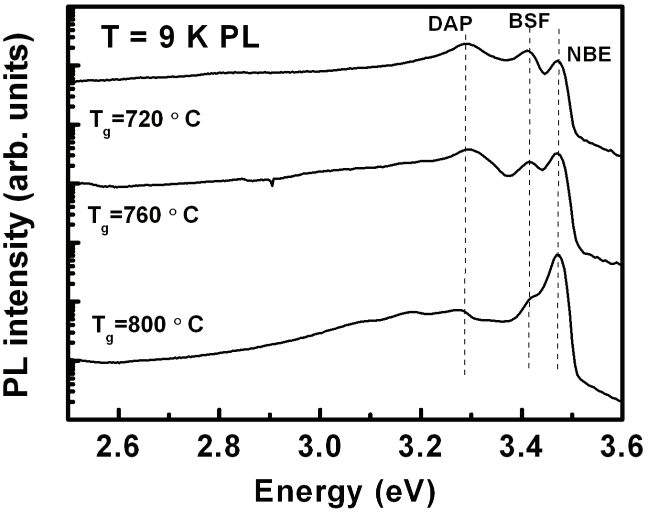

Figure 4.2.3 LT PL spectra of MBE-grown *a*-plane GaN on *r*-sapphire substrate, with the temperature of the 2nd step growth process varies: 800, 760, and 720 °C.

Combining data from both PL and XRD, it is concluded that material quality deteriorates with the decrease of T_g^2, due to the increase of impurities and defects densities.

In conclusion, planar *a*-plane GaN layers can be grown on *r*-sapphire by MBE, using a modified one-step HT growth process. The modification is referred to a change of T_g: from T_g^1 ~ 870 °C to T_g^2 ~ 800 °C. Besides, slower growth rate is also needed in order to increase the diffusion length. The reduction of T_g^2 below 800 °C leads to lower structural and optical properties.

4.3 GaN/AlGaN single quantum wells grown on ELO templates

In sections 3.2 and 3.4, it has been demonstrated that non-polar *a*- and *m*-plane GaN ELO templates have allowed improving the surface morphology and material quality on the mask areas. Thus, they are qualified substrates for the fabrication of nanostructures by MBE.

Heterostructures grown on non-polar planes are expected to be free of QCSE.[7] To verify that point, GaN/AlGaN single quantum wells (SQWs) have been grown on both *a*- and *m*-plane ELO templates. SQW is highly sensitive to polarization-induced electric field, since the latter does not reduce with the decrease of the barrier thickness as in the case of multiple QW structures.[8]

4.3.1 *A*-plane SQWs

A series of GaN/AlGaN SQWs have been grown on *a*-plane HVPE ELO templates, with three nominal QW widths: 2, 5, and 8 nm (figure 4.3.1). For each well width, there are three nominal Al fractions (x): 5, 10, and 20 %. Here, “nominal” means that the Al content is estimated from growth rates measured by RHEED intensity oscillations on *c*-plane. The growth temperature is 800-820 °C.

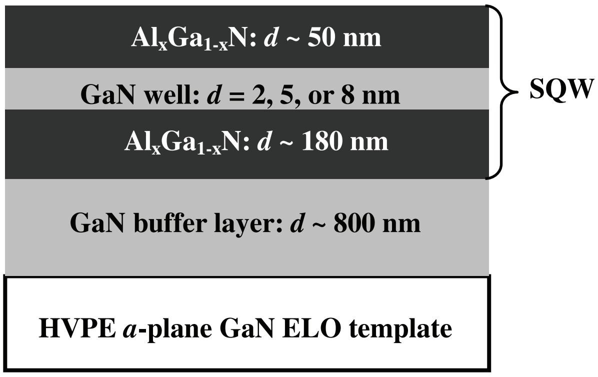

Figure 4.3.1 Schematic structure of GaN/AlGaN SQW grown by MBE on *a*-plane GaN HVPE ELO template.

Interestingly, we observed systematic small discrepancies between the nominal and measured values of Al content and layer thickness:[*] the measured layer thicknesses are lower and the Al fractions are higher, as listed in table 4.3. In an attempt to explain this phenomenon, let us first take a look at (0001) and $(11\bar{2}0)$ GaN planes: if the sticking coefficient (SC) is unity for

---

[*] The layer thicknesses and Al fractions were determined through TEM and Energy Dispersive X-Ray Spectroscopy, performed by Y. Arroyo (CIME, EPFL) and described in section 4.9 of her PhD thesis (EPFL_TH4193).

both planes, then the same Ga flux should results in same thickness (+*c*: Ga densiy 11.4 nm^{-2} and ML 2.59 Å *vs. a*: Ga density 7 nm^{-2} and ML 1.59 Å). However, SC of Ga adatoms on non-polar planes may be different from that on polar *c*-plane. Report on *a*-plane is lacking, but there are a few on *m*-plane: K. A. Bertness *et al.* has reported that Ga SC on *m*-plane is lower than that of *c*-plane.[9] Along this, the study of Ga adlayer adsorption/desorption by S. Choi *et al.* has demonstrated that *m*-plane surface has slower adsorption and faster desorption rates in comparison with *c*-plane.[10] Thus, the GaN growth rate is expected to be lower in *a*-plane than in *c*-plane, leading to an increase of Al content as the SC of Al is equal to 1 at T ~ 800 °C. For example, 20 % decrease in GaN growth rate will increase Al fraction from 20 % to 23.8 % in AlGaN layer. To avoid misunderstanding, all the numbers mentioned below are nominal unless specified.

	AlGaN bottom barrier thickness (nm)	AlGaN top barrier thickness (nm)	GaN SQW width (nm)			Al fractions (%)		
Nominal	200	50	2	5	8	20	10	5
Average Measured	160	40	1.7	3.7	6.1	22.8	13.4	7.8

Table 4.3 Nominal and measured results of thicknesses and Al fractions of *a*-plane GaN/AlGaN SQWs. (By courtesy of Y. Arroyo of CIME, EPFL)

LT μ-PL characterizations have been performed on these SQW structures in the mask areas where defects density is lower. The spectra for three SQWs with 20% Al fraction are displayed in figure 4.3.2 (a). The FWHMs of the peaks range between 17–40 meV. They are comparable to those grown on *c*-plane,[11] indicating a reasonably good optical quality. The peaks do not shift with the increase of excitation power density by two orders of magnitude, which is an indication of polarization-free QWs. The inhomogeneous broadening increases with the decrease of well width, probably due to interface roughness scattering with large wavefunction penetration into the barrier.[12] In addition, the localization energies of QW exciton recombinations have been measured, depending on the well width and Al content in the barriers.[13] For example, the localization energy for 20 % Al fraction and 5nm width is ~ 24 meV, obtained from the temperature-dependant μ-PL with a Varshni simulation [figure 4.3.2 (b)]. The numbers are comparable to those of *c*-plane, which confirm the high quality of the present non-polar QWs.[8]

Figure 4.3.2 (c) shows the transition energy of SQWs with 10% Al fraction and well widths of 2, 5, and 8 nm. The solid and dash lines correspond to simulations of SQW ground-state transitions with built-in electric fields F = 0 and 415 kV/cm, respectively. The exciton localization energies (16, 17, 10 meV for 2, 5, 8 nm well width, respectively) are taken into account. As one can see, the data are well accounted for by the model with no electric filed in the structure. Therefore, this confirms that GaN/AlGaN SQWs grown on *a*-plane GaN ELO templates are free from QCSE.

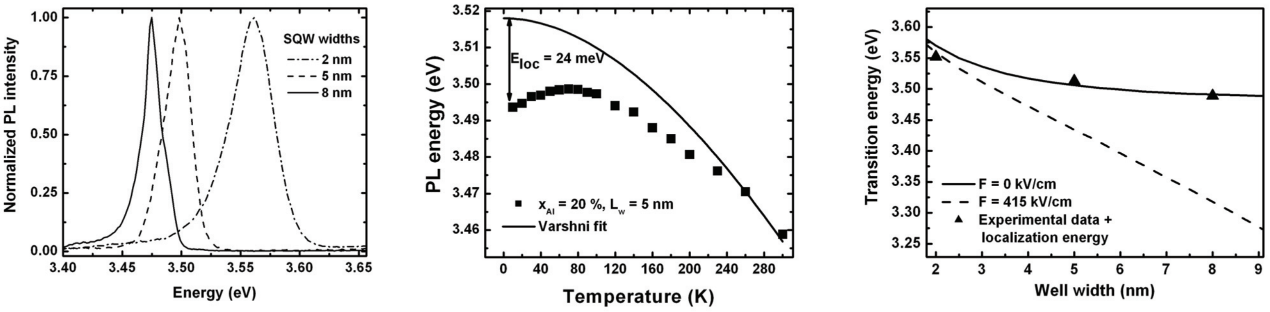

(a) (b) (c)

Figure 4.3.2 (a) LT μ-PL (T = 4K) spectra on SQWs (20 % Al fraction) with well widths of 2, 5, and 8 nm. (b) PL energy as function of termperature for SQW (20% Al fraction) with 5 nm well width. (c) solid- and dash-lines are the calculated transition energies of SQWs (10 % Al fraction) for well widths of 2, 5, and 8 nm, with built-in electric field F = 0 and 415 kV/cm, respectively. Dots are the measured data, including the correction from the localization energy. (By courtesy of A. Dussaigne at LASPE, EPFL)

There is no significant impact on optical properties arising from BSFs in the aforementioned SQWs. However, as mentioned in section 3.2.1, in +*c* wing of mask areas there are still some BSFs accumulated into bundles with density in the range of 10^4 cm^{-1}. They act as type-II QW: zinc-blende-like material sandwiched by wurtzite one. The structure of such QWs is perpendicular to the surface, whereas the as-grown GaN/AlGaN SQWs are parallel to the surface. The intersections of these two QW-structures have been observed by TEM, as shown in figure 4.3.3 (a). The BSFs in AlGaN barriers originate from HVPE ELO templates. It looks like these BSFs are interrupted at the QW interface. Actually, this is not the case as seen in figure 4.3.3 (b), which is an enlarged view near the QW region. High magnification filtered image shows that there are two inserted planes instead of one, as marked by the arrows in figure 4.3.3 (c). A plausible explanation is depicted in figure 4.3.3 (d): there are two BSFs aligned parallel to each other, one BSF extending from the bottom barrier is terminated by a PSF in the left side, and the other BSF originates from the right side and extends further to the top. The distance between these two BSFs is so short that it is difficult to discriminate them in a low magnification image.[14]

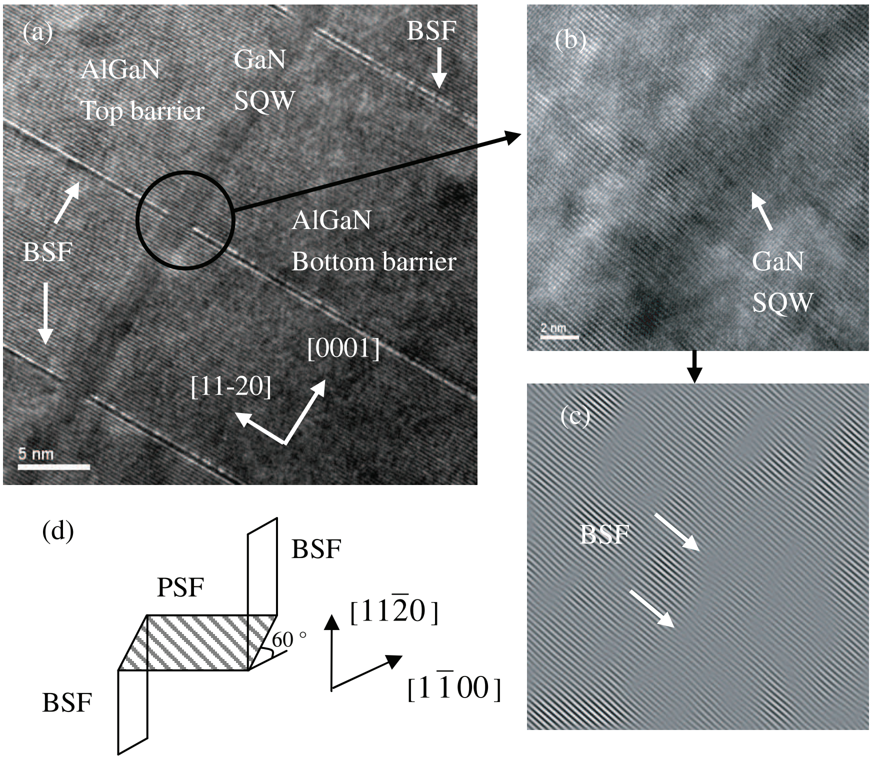

Figure 4.3.3 (a) and (b) are low and high magnification TEM images of GaN/AlGaN SQW structure grown on *a*-plane GaN ELO templates. (c) is the filtered image of (b), where the BSFs are marked by the arrows. (d) schematically depicts two BSFs terminated by one PSF. TEM images (a) – (c) are by courtesy of Y. Arroyo (CIME, EPFL)

The BSF-SQW intersection resembles a quantum-wire structure and thus has an effect on the optical properties. For example, LT μ-PL spectrum for the SQW with 10% Al fraction and 5 nm well width is shown in figure 4.3.4. The emission peak near 3.42 eV is related to BSFs. It means that this μ-PL measurement is performed in an area with bundles of BSFs. The peak around 3.51 eV is due to the recombination of excitons in SQW. Besides, there is another peak around 3.48 eV and it is not likely to be induced by excitons localized at QW inhomogeneities. Instead, it is ascribed to BSF-SQW quantum-wire bound exciton recombinations.[15,16] In comparison, the spectra in figure 4.3.2 (a) are free of the emission of the emission from such quantum-wire structure, because they are mearsured in areas basically free of BSFs.

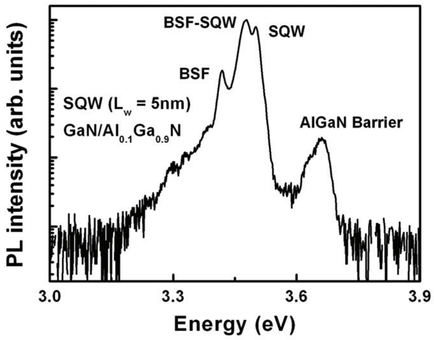

Figure 4.3.4 LT μ-PL spectrum for the SQW with Al fraction 10% and well width 5 nm.

4.3.2 *M*-plane SQWs

Some *m*-plane SQWs have been grown on HVPE non-coalesced ELO templates with various Al fraction and well width. One representative sample corresponds to 5% Al and 8 nm well width. The mask area has been characterized by AFM and μ-PL. Figure 4.3.5 (a) is an AFM image on the mask area. Compared to the "step" surface feature of HVPE ELO mask in figure 3.4.2 (c), the MBE-grown layer has a different morphology, as stripe features perpendicular to $[11\bar{2}0]$ direction are observed. Besides, pyramidal hillocks have been found, with height of ~ 15 nm. The rms roughness is ~ 2.7 nm on an AFM scan area of 5 × 5 μm^2, which is about one order of magnitude higher than that of HVPE ELO (~ 0.2 nm). It is due to kinetic roughening which occurs under N-rich conditions. The rms value is similar to that of *a*-plane.

The LT (T = 4K) μ-PL spetrum is presented in figure 4.3.5 (b). It is dominated by QW peak near 3.48 eV with FHWM ~ 20 meV (the AlGaN barrier is at 3.58 eV), similar to that of *a*-plane (~ 18 meV) with same well width and Al fraction. This value is also comparable to those grown on *c*-plane, indicating good optical property.[11]

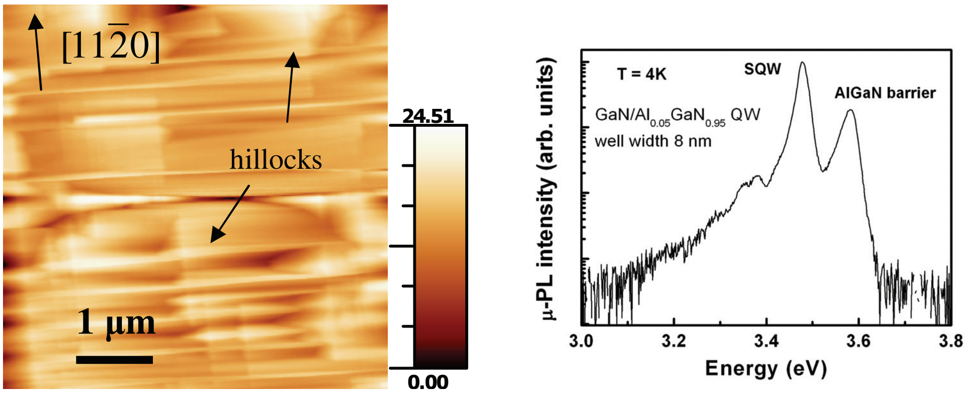

Figure 4.3.5 GaN/AlGaN SQW grown on mask area of HVPE ELO templates: (a) AFM image and (b) LT μ-PL spetrum

It is known that for *c*-plane GaN/AlGaN QWs, the spatial separation of charge carriers within QWs increases with the increase of well width. In some cases, the MQWs emission is no longer observed for wells wider than 5 nm.[8, 17] In contrast, we have observed PL emissions from non-polar SQWs with wells as wide as 8 nm, indicating a drastic improvement of radiative efficiency. Besides, *c*-plane QWs experience redshift with the increase of well width and PL emission from wells wider than 3 nm is usually below the bulk GaN bandgap. However, our data reveal that the emission energy from non-polar SQWs with 8 nm well width is still above the GaN bandgap value.

In conclusion, GaN/AlGaN SQWs with various Al fractions and well-widths have been grown on both *a*- and *m*-plane HVPE ELO templates. LT μ-PL confirms that they are free from QCSE. The emission peak linewidths range from 20 to 40 meV, which are comparable to those of *c*-plane and suggest good optical properties. Particularly, TEM scans reveal that quantum-wire structures are formed where BSF and SQW intersect. The related emission peak can be observed when LT μ-PL is performed on areas with BSFs.

4.4 Distributed Bragg reflectors and microcavities grown on *a*-plane GaN ELO templates

Brief introduction of DBRs and MCs and the motivation for non-polar surfaces

Distributed Bragg reflectors (DBRs) are stacks of quarter-wave layers alternating two materials with different refractive indices (n_1 and n_2), as shown in figure 4.4.1. The combination of the adjacent two layers (one n_1 and one n_2) is called a pair. In short, a DBR works as a selection or filter of certain wavelength, since the corresponding waves propagating along the reflection direction are in phase after multiple reflections. Details on the design and properties of DBRs can be found in the literal of H. A. Macleod[18] and V. Savona[19].

Semiconductor microcavities (MCs) are based on DBRs, since DBRs are suitable to form Fabry-Perot interferometers, and they can be grown by standard thin-film epitaxy techniques (MBE and MOVPE). A typical MC is schematically depicted in figure 4.4.1. It is made of one cavity layer, sandwiched by two DBRs (top and bottom). The cavity layer can be either GaN ("empty") or containing QWs. The "top" and "bottom" DBRs are defined by the order of growth procedure. Note these two DBRs do not need to be identical. For example, for nitride-based MCs, the bottom DBR is usually made of Al(Ga)N/(Al)GaN or AlInN/(Al)GaN, while the top is a dielectric DBR (*e.g.* SiO_2/SiN_x). More details on nitride-based DBRs and

MCs can be found in the paper of R. Butté *et al.*[20]

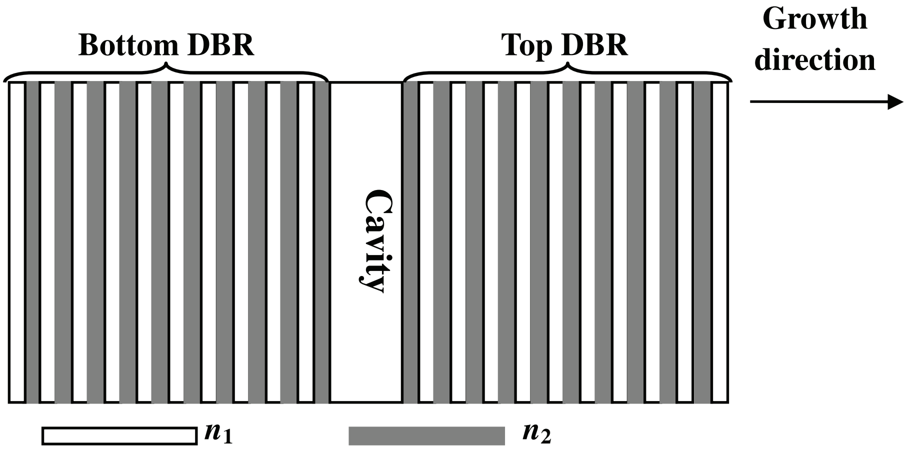

Figure 4.4.1 Schematic structure of a semiconductor MC, formed by two DBRs and a cavity in-between.

With the commercialization of UV-blue light emitting diodes and laser diodes,[21] research on advanced optoelectronic devices, like vertical cavity surface emitting lasers,[22] has attracted increasing attention. Along with this, one of the most attractive approaches relies on polariton lasing,[23] which has been recently reported in polar GaN-based MCs.[24] This class of light emitters is based on strong light-matter interaction, the so-called strong coupling regime (SCR), arising in high-quality MCs. SCR can allow drastically decreasing the lasing threshold thanks to the ultra-low effective mass of cavity polaritons, which are mixed exciton-photon states behaving like bosons.

SCR has already been demonstrated in a MC grown on *c*-plane GaN template using GaN/AlGaN multiple QWs.[25] In Ref. 25, thin QWs were used in order to limit the detrimental impact of QCSE. Furthermore, the broadening of QW absorption, arising from composition inhomogeneities and/or well thickness fluctuations, whose effect is amplified by the QCSE in wide wells, could eventually lead to the disappearance of the SCR.[26] MCs grown on nonpolar surfaces (*a*- or *m*- planes) are thus of particular interest as one may take advantage of polarization-free QWs. Indeed, thick non-polar QWs would exhibit both large oscillator strength and reduced inhomogeneous broadening that would lead to unprecedented large Rabi splittings. This would enable photonic devices based on robust polaritons at RT.[27]

4.4.1 AlN/GaN DBR

After loading the *a*-plane GaN ELO template into the MBE chamber, a standard annealing process was conducted at T ~ 850 °C for about 10 min under NH_3. The ELO template is not fully coalesced to avoid potential introduction of defects in the coalesced regions. Then a

GaN layer (*d* ~ 800 nm) was grown on that, which serves as a buffer in order to avoid contamination from the interface. On top of it, 13 pairs AlN/GaN quarter-wave stack was deposited. The nominal thicknesses of AlN and GaN layers were 47 nm and 41 nm, respectively. The GaN (AlN) growth rate was 1 monolayer (ML)/s (0.1 ML/s) and the growth temperature was 800°C (900°C).

A high magnification SEM cross-section image of this DBR is presented in figure 4.4.2. The AlN/GaN interfaces are well defined and flat at the scale of the SEM image. The measured thicknesses of the AlN and GaN stack layers are ~ 45 nm and ~ 39 nm, respectively. They are uniform across the entire structure and a little bit smaller than the nominal thicknesses. Although the AlN/GaN material system usually suffers from a large in-plane lattice mismatch, no crack could be observed by SEM in the DBR structure. This was further confirmed by phase contrast optical microscopy measurements. This could be attributed to the voids that form at the interface between the MBE GaN template and the first AlN stack layer. Similar voids have already been reported[28] and could be ascribed to plastic relaxation through buried cracks originating from the tensile biaxial strain occurring at the interface of GaN ELO template and the AlN/GaN DBR. They are 20 - 50 nm wide and separated by a distance varying randomly from 100 nm to a few micro-meters. Plus, the accumulated stress may also be partly relieved due to the fact that the ELO layer is not fully coalesced.

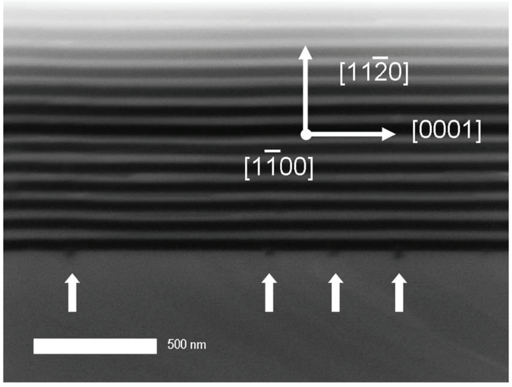

Figure 4.4.2 Cross-section SEM picture of the AlN/GaN DBR structure, where the arrows indicate voids.

Micro-reflectivity measurements were performed at RT on the mask regions (spot size ~1 µm in diameter). The reflectivity spectra were normalized with a calibrated Al mirror measured under the same conditions. Linearly polarized light has been used to observe the birefringence effect. Indeed, wurtzite GaN and AlN exhibit positive linear birefringence ($\Delta n = n_e - n_o$), *i.e.*, for both materials, the refractive index for light polarized perpendicular to the *c*-axis (ordinary refractive index n_o) is lower than that for light polarized parallel to the *c*-axis (extraordinary refractive index n_e). The spectra for each polarization are dispalyed in figure 4.4.3 (a). The peak reflectivity is estimated to ~ 95%, which well compares with those of AlN/GaN DBRs grown on *c*-plane substrates[29,30] using similar period numbers. The center wavelengths with light polarized perpendicular and parallel to the *c*-axis are 371 nm and 373 nm, respectively. Such birefringence effect has also been reported on *m*-plane AlN/GaN DBRs.[31] Both spectra are characterized by a flat stopband, with SBW of ~ 30 nm.

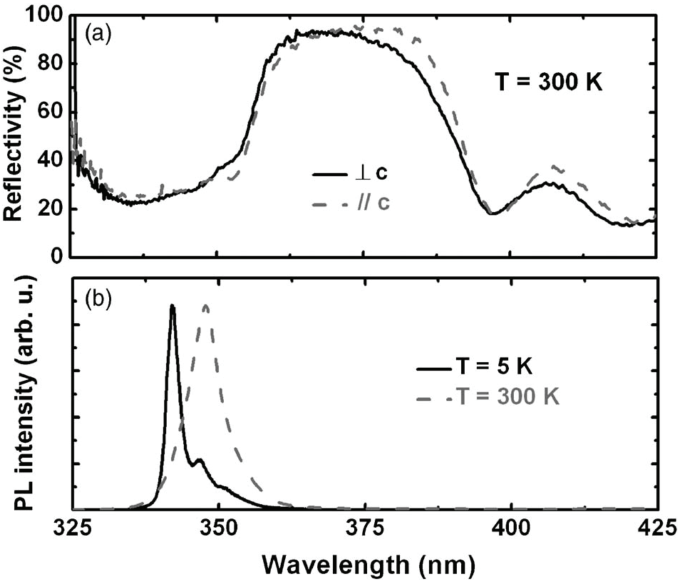

Figure 4.4.3 (a) RT micro-reflectivity spectra of the AlN/GaN DBR (under linearly polarized light), perpendicular to the *c*-axis (black solid line) and parallel to the *c*-axis (gray dashed line). (b) Normalized LT (black solid line) and RT (gray dashed line) μ-PL spectra of the GaN stacked layers.

It is worth noticing that the unstrained RT GaN bandgap (λ ~ 363 nm)[32] would actually be located within the stopband, but the reflectivity spectra do not exhibit any absorption feature on the short wavelength side. To address this point, RT and LT μ-PL measurements were performed on the AlN/GaN DBR within the mask region [figure 4.4.3 (b)]. As the total GaN thickness in the DBR structure (~ 0.5 μm) is much larger than the laser absorption depth (~ 0.3 μm), μ-PL spectra only reflect the optical properties of the GaN stack layers. The NBE emission peak at RT is near 348 nm (3.564 eV) with a FWHM of 6 nm (gray dashed line). At LT, the NBE emission peak is centered at 342 nm (3.623eV) with a FWHM of 3 nm (black solid line). This indicates that the band gap of the GaN stack layers is strongly blue-shifted with respect to that of relaxed bulk GaN. Considering that RT PL corresponds to free-exciton recombinations, one can conclude that the blue-shift is about 150 meV. In other words, GaN stack layers experience a large compressive stress. Assuming that after a few periods, the DBR has reached its average equilibrium in-plane lattice parameter corresponding roughly to an $Al_{0.5}Ga_{0.5}N$ alloy, the in-plane strain would be -1.2% and -2% in the $[1\bar{1}00]$ and [0001] directions, respectively.[33] Furthermore, one has to take into account the difference in thermal expansion coefficients between GaN and AlN along both in-plane directions, which results in compressive strains equal to ε_{yy} = -2% and ε_{zz} = -3% in the $[1\bar{1}00]$ and [0001] directions, respectively. These values accout for the blue-shift of the GaN NBE peak.

4.4.2 Nitride-based MC

A hybrid MC structure with a λ empty GaN cavity (d ~167 nm) was fabricated on a similar ELO GaN template. The nominal thicknesses of AlN and GaN layers in the bottom DBR were adjusted to 51 nm and 42 nm, respectively, to reach a central wavelength of ~400 nm, as predicted by transfer matrix calculations.[18,34] Finally, a top dielectric DBR, made of 10 pairs of SiO_2 (69 nm) and SiN_x (55 nm) layers, was deposited by plasma-enhanced chemical vapor deposition [figure 4.4.4 (a)].

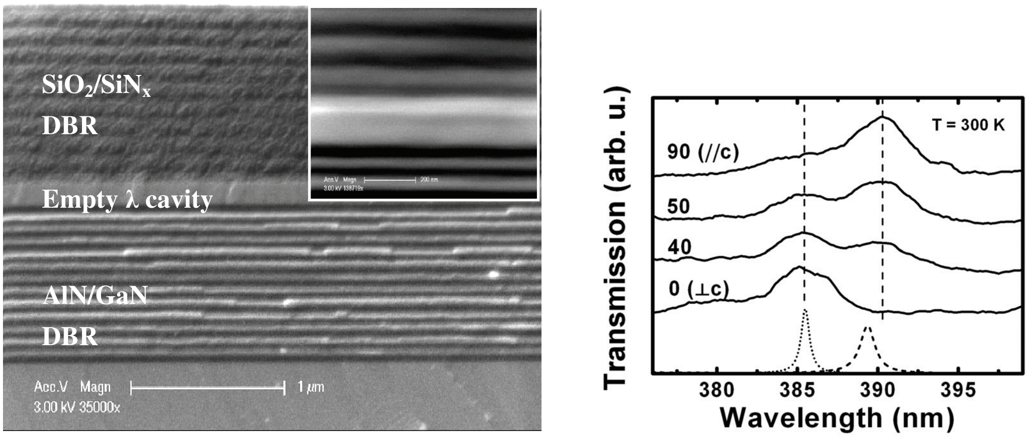

Figure 4.4.4 (a) SEM cross-section image of nitride-based MC, and inset shows is an enlarged view near the cavity region. (b) RT micro-transmission spectra as a function of light polarization angles, after Ref. 33.

Figure 4.4.4 (b) displays the RT micro-transmission spectra (spot size ~ 4 μm) for various light polarization angles (black solid lines). When changing the linear polarization angle from 0° (light polarization perpendicular to the *c*-axis) to 90° (light polarization parallel to the *c*-axis), the transmission peak switches from 384.5 nm to 390.2 nm. These two peaks correspond to cavity modes with the one at 384.5 nm satisfying the resonance condition for the MC with n_o, whereas the one at 390.2 nm satisfies the resonance condition for the MC with n_e. Both modes are clearly resolved and have a linewidth of 4 nm, which corresponds to a quality factor ($Q=\lambda/\Delta\lambda$) of ~100. Simulations were performed by G. Christmann.[35] The refractive indices for AlN and GaN are taken from the work of Shokhovets *et al.*[34] The layer thicknesses have been adjusted in order to have the structure with refractive index n_o matched to 384.5 nm (gray dotted line), which is the experimental mode position for light polarized perpendicular to the *c*-axis. Then, the simulation repeated with the refractive index values changed to n_e (gray dashed line). The calculated cavity mode is centered at 389.4 nm, *i.e.* very close to the experimental value (390.2 nm). The slight discrepancy could be ascribed to the different strain state of GaN and AlN stacked layers compared to those studied in Ref. 34. In addition, the calculated *Q* factors (Q ~ 640/340 for n_0/n_e) are larger than the experimental values. This could be due to in-plane disorder in the MC. Nevertheless, such preliminary result is quite encouraging as the overall optical properties compare favorably with other reports for similar MCs grown on *c*-plane sapphire substrates.[36] Such a structure represents the first step toward polarization-free QW-MCs aimed at realizing polariton lasers and achieving RT Bose-Einstein condensation.

4.5 Summary

- GaN homoepitaxy has been conducted on both *a*- and *m*-plane HVPE templates. The influence of growth parameters have been studied. For *a*-plane, high substrate temperature is found to favor in-plane lateral growth. For *m*-plane, high V/III ratio is favored.

- Heteroepitaxial growth of *a*-plane GaN on *r*-plane sapphire substrate has been studied. A two-temperature growth procedure has been developed and optimized. Although the surface smoothness is inferior to that of HVPE epilayers, the optical properties are slightly improved.

- GaN/AlGaN SQWs with various well widths and Al fractions have been grown on both *a*- and *m*-plane HVPE ELO templates. They are found to be free from QCSE. Sometime, the presence of BSFs in the mask area brings an uncommon local phenomenen to the optical properties, *i.e.* BSFs intersect with QWs, forming a quantum-wire complex. This structure can be observed as an emission peak ~ 30 meV lower than the SQW-related peak.

- DBR and MC structures have been grown *a*-plane ELO templates. Their optical properties are encouraging as they are close to those grown on *c*-plane and open the way for more sophisticated structures aimed at polariton physics.

Bibliography

---

[1] S. Vézian, F. Natali, F. Semond, and J. Massies, "From spiral growth to kinetic roughening in molecular-beam epitaxy of GaN(0001)", *Physical Review B*, vol. 69, no. 12, pp. 125329, 2004.

[2] N. Grandjean, J. Massies, P. Vennéguès, M. Leroux, F. Demangeot, M. Renucci, and J. Frandon, "Molecular-beam epitaxy of gallium nitride on (0001) sapphire substrates using ammonia", *Journal of Applied Physics*, vol. 83, no. 3, pp. 1379-1383, 1998.

[3] N. Grandjean, J. Massies, and M. Leroux, "Nitridation of sapphire. Effect of the optical properties of GaN epitaxial overlayers", *Applied Physics Letters*, vol. 69, no. 14, pp.

2071-2073, 1996.

[4] T. Hanada, B. –H. Koo, H. Totsuka, and T. Yao, “Anisotropic shape of self-assembled InAs quantum dots: Refraction effect on spot shape of reflection high-energy electron diffraction”, *Physical Review B*, vol. 64, no. 16, pp. 165307, 2001.

[5] M. A. Moram, C. F. Johnston, J. L. Hollander, M. J. Kappers, and C. J. Humphreys, “Understanding x-ray diffraction of nonpolar gallium nitride films”, *Journal of Applied Physics*, vol. 105, no. 11, pp. 113501, 2009.

[6] P. P. Paskov, R. Schifano, B. Monemar, T. Paskova, S. Figge, and D. Hommel, “Emission properties of a-plane GaN grown by metal-organic chemical-vapor deposition”, *Journal of Applied Physics*, vol. 98, no. 9, pp. 092519-1-7, 2005.

[7] P. Waltereit, O. Brandt, A. Trampert, H. T. Grahn, J. Menniger, M. Ramsteiner, M. Reiche, and K. H. Ploog, “Nitride semiconductors free of electrostatic fields for efficient white light-emitting diodes”, Nature, vol. 406, pp. 865-868, 2000.

[8] N. Grandjean, B. Damilano, S. Dalmasso, M. Leroux, M. Laügt, and J. Massies, “Built-in electric-field effects in wurtzite AlGaN/GaN quantum wells”, *Journal of Applied Physics*, vol. 86, no. 7, pp. 3714-3720, 1999.

[9] K. A. Bertness, A. Roshko, L. M. Mansfield, T. E. Harvey, and N. A. Sanford, “Mechanism for spontaneous growth of GaN nanowires with molecular beam epitaxy”, Journal of Crystal Growth, vol. 310, pp. 3154, 2008.

[10] S. Choi, T.-H. Kim, H. O. Everitt, A. Brown, M. Losurdo, G. Bruno, and A. Moto, “Kinetics of gallium adlayer adsorption/desorption on polar and nonpolar GaN surfaces”, *Journal of Vaccum Science and Technology B*, vol. 25, no. 3, pp. 969-973, 2007.

[11] F. Natali, D. Byrne, M. Leroux, B. Damilano, F. Semond, A. Le Louarn, S. Vezian, N. Grandjean, and J. Massies, “Inhomogeneous broadening of AlGaN/GaN quantum wells”, *Physical Review B*, vol. 71, no. 07, pp. 075311, 2005.

[12] L. M. Woods, P. Silvestre, P. Thiagarajan, G. A. Patrizi, G. Y. Robinson, K. M. Jones, and M. Al-Jassim, “Photoluminescence and interface abruptness in InGaAsP/InGaAsP quantum wells”, *Journal of Electronic Materials*, vol. 23, no. 11, pp. 1229-1233, 1994.

[13] M. Leroux, N. Grandjean, M. Laügt, J. Massies, B. Gil, P. Lefebvre, and P. Bigenwald, “Quantum confined Stark effect due to built-in internal polarization fields in (Al, Ga)N/GaN quantum wells”, *Physical Review B*, vol. 58, no. 20, pp. R13371-13374, 1998.

[14] Y. Arroyo, PhD Thesis “Characterization of *A*-plane Grown GaN on sapphire substrate by electron microscopy”, Figure 4.46, pp. 116, EPFL_TH4193, 2008.

[15] T. J. Badcock, P. Dawson, M. J. Kappers, C. McAleese, J. L. Hollander, C. F. Johnston, D. V. Sridhara Rao, A. M. Sanchez, and C. J. Humphreys, “Optical properties of GaN/AlGaN quantum wells grown on nonpolar substrates”, *Applied Physics Letter*, vol. 93, no. 10, pp. 101901, 2008.

[16] P. Corfdir, L. Balet, P. Lefebvre, S. Sonderegger, A. Dussaigne, T. Zhu, D. Martin, J.-D. Ganière, N. Grandjean, and B. Deveaud-Plédran, “Time-resolved cathodoluminescence on quantum well and quantum wire excitons in *a*-plane GaN”, submitted to *Applied Physics Letter*

[17] M. D. Craven, P. Waltereit, J. S. Speck, and S. P. DenBaars, “Well-width dependence of photoluminescence emission from a-plane GaN/AlGaN multiple quantum wells”, *Applied Physics Letter*, vol. 84, no. 4, pp. 496-498, 2004.

[18] H. A. Macleod, *Thin-film optical filters*, Adam Hilger, Bristol, second ed., 1986.

[19] V. Savona, *Confined Photon Systems, Fundamentals and Applications*, ch. Linear Optical Properties of Semiconductor Microcavities with Embedded Quantum Well, p. 173. Springer, Berlin, 1999.

[20] R. Butté, E. Feltin, J. Dorsaz, G. Christmann, J.-F. Carlin, N. Grandjean, and M. Ilegems, “Recent Progress in the Growth of Highly Reflective Nitride-Based Distributed Bragg Reflectors and Their Use in Microcavities,” *Japanese Journal of Applied Physics*, vol. 44, pp. 7207–7216, 2005.

[21] S. Nakamura, S. J. Pearton, and G. Fasol, *The Blue Laser Diode, the Complete Story* (Springer-Verlag, Heidelberg, 2nd edition, 2000).

[22] T. Someya, R. Werner, A. Forchel, M. Catalano, R. Cingolani, and Y. Arakawa, “Room temperature lasing at blue wavelength in gallium nitride microcavities”, *Science*, vol. 285, no. 5435, pp. 1905-1906, 1999.

[23] A. Kavokin and B. Gil, “GaN microcavities: giant rabi splitting and optical anisotropy”, *Applied Physics Letter*, vol. 72, no. 22, pp. 2880-2881, 1998.

[24] S. Christopoulos, G. Baldassarri Höger von Högersthal, A. J. D. Grundy, P. G. Lagoudakis, A. V. Kavokin, J. J. Baumberg, G. Christmann, R. Butté, E. Feltin, J.-F. Carlin, and N. Grandjean, “Room-temperature polariton lasing in semiconductor microcavities”, *Physical Review Letter*, vol. 98, no. 12, pp. 126405, 2007.

[25] E. Feltin, G. Christmann, R. Butté, J.-F. Carlin, M. Mosca, and N. Grandjean, “Room temperature polariton luminescence from a GaN/AlGaN quantum well microcavity”, *Applied Physics Letter*, vol. 89, no. 07, pp. 071107, 2006.

---

[26] G. Christmann, R. Butté, E. Feltin, J.-F. Carlin, and N. Grandjean, “Impact of inhomogeneous excitonic broadening on the strong exciton-photon coupling in quantum well nitride microcavities”, *Physical Review B*, vol. 73, no. 15, pp. 153305, 2006.

[27] M. A. Mastro, E. A. Imhoff, J. A. Freitas, J. K. Hite, and C. R. Eddy Jr., “Towards a polariton-based light emitter based on non-polar GaN quantum wells”, *Solid State Communications*, article in press, 2009.

[28] J.-M. Bethoux, P. Vennéguès, F. Natali, E. Feltin, O. Tottereau, G. Nataf, P. De Mierry, and F. Semond, “Growth of high quality crack-free AlGaN films on GaN templates using plastic relaxation through buried cracks”, *Journal of Applied Physics*, vol. 94, no. 10, pp. 6499-6507, 2003.

[29] H. M. Ng, T. D. Moustakas, and S. N. G. Chu, “High reflectivity and broad bandwidth AlN/GaN distributed Bragg reflectors grown by molecular-beam epitaxy”, *Applied Physics Letter*, vo. 76, no. 20, pp. 2818-2820, 2000.

[30] T. Ive, O. Brandt, H. Kostial, T. Hesjedal, M. Ramsteiner, and K. H. Ploog, “Crack-free and conductive Si-doped AlN/GaN distributed Bragg reflectors grown on 6H-SiC (0001)”, *Applied Physics Letter*, vo. 85, no. 11, pp. 1970-1972, 2004.

[31] D. M. Schaadt, O. Brandt, S. Ghosh, T. Flissikowski, U. Jahn, and H. T. Grahn, “Polarization-dependent beam switch based on an *M*-plane GaN/AlN distributed Bragg reflector”, *Applied Physics Letter*, vo. 90, no. 23, pp. 231117, 2007.

[32] W. Shan, R. J. Hauenstein, A. J. Fischer, J. J. Song, W. G. Perry, M. D. Bremser, R. F. Davis, and B. Goldenberg, “Strain effects on excitonic transitions in GaN: deformation potentials”, *Physics Review B*, vol 54, no. 19, pp. 13460-13463, 1996.

[33] T. Zhu, A. Dussaigne, G. Christmann, C. Pinquier, E. Feltin, D. Martin, R. Butte, and N. Grandjean, “Nonpolar GaN-based microcavity using AlN/GaN distributed Bragg reflector”, *Applied Physics Letter*, vo. 92, no. 6, pp. 061114, 2008.

[34] S. Shokhovets, R. Goldhahn, G. Gobsch, S. Piekh, R. Lantier, A. Rizzi, V. Lebedev, and W. Richter, “Determination of the anisotropic dielectric function for wurtzite AlN and GaN by spectroscopic ellipsometry”, *Journal of Applied Physics*, vol. 94, no. 1, pp. 307-312, 2003.

[35] G. Christmann, PhD Thesis “III-Nitride based microcavities: towards polariton condensation at room termperature”, EPFL_TH4285.

[36] G. S. Huang, H.-G. Chen, J.-R. Chen, T. C. Lu, H. C. Kuo, and S. C. Wang, phys. stat. sol. (a) 204, pp. 1977-1981, 2007.

Conclusion and Perspective

Summary of the experimental results

The objectives of this PhD thesis consist of two parts: (1) growing non-polar (*a*- and *m*-planes) GaN epilayers with reasonable material quality on sapphire substrates by HVPE, and (2) investigating nanostructrues on such templates by NH_3-source MBE with the aim of getting rid of the QCSE and achieve brand new physical properties, especially in the field of strong light-matter interaction.

First Objective

Highlights:

- **Pressure-variation method for *a*-plane GaN on *r*-plane sapphire**
- **Growth of *m*-plane GaN on *m*-plane sapphire**

HVPE-grown *a*-plane planar GaN templates was the first obtained.[1] A striking feature is that their surface morphology is quite sensitive to the growth pressure, as the growth mode transfers from 3D to 2D with the decrease of pressure. Therefore, a pressure-variation method was developed to take advantage of this observation, resulting in moderate improvement in structural and optical properties. Besides, the two-step growth procedure similar to that conventionally performed on *c*-plane (*i.e.* using a LT GaN NL) was tested. Unfortunately, it failed to improve the material quality significantly. Both AFM and *in situ* LR reveal that the effective NL evolution observed on *c*-plane during temperature ramping, which leads to the formation of large 3D crystal islands, is missing here. In addition, TEM investigations show that edge and mixed dislocations propagate towards the top surface and do not bend since the basal *c*-plane is most stable for them.

Next, *m*-plane GaN has been successfully grown on *m*-plane sapphire for the first time by HVPE, using a LT GaN NL.[2] Actually, we have demonstrated that three different GaN orientations (two semi-polar and one non-polar *m*) can be achieved. We propose that sapphire surface chemistry is the main factor influencing the nucleation, and subsequently, the GaN thin film orientation of *m*-plane. The material quality, though not satisfactory, is comparable to that grown on more-expensive non-polar SiC substrates. In addition, there is one distinct feature: the in-plane polarity uniqueness of GaN epilayer is determined by that of sapphire substrate. *M*-sapphire does not have that kind of uniqueness, leading to the formation of in-plane inversion domains in the epilayers.[3]

A- and *m*-plane GaN epilayers share something in common: in terms of surface morphology, there is a strong growth anisotropy on both planes and their surfaces are quite rough, with rms about an order of magnitude higher than that of planar *c*-plane. XRD on-axis ω scans reveal structural anisotropy, probably due to a complex interplay between defects and surface roughness. Both have high defects density: TD ~ 10^{10} cm^{-2} and BSF ~ 10^5 cm^{-1}. In other words, they are inferior in material quality to the planar *c*-GaN grown on *c*-sapphire. Thus, single-step ELO templates were applied. On the +*c* side of the mask areas, the defects densities are reduced: TD 10^8-10^9 cm^{-2} and BSF ~ 10^4 cm^{-1}, and the rms roughness is close to that of *c*-plane. Therefore, these ELO templates are good enough as substrates for the subsequent MBE epitaxy of nanostructures.

Second Objective

Highlights:

- **Homoepitaxy of *m*-plane GaN**
- **Heteroepitaxy of *a*-plane GaN on *r*-plane sapphire**
- **Intersection of SQW and BSF (quantum-wire structure)**
- ***A*-plane AlN/GaN DBRs and nitride-based MCs**

Some preliminary investigations of MBE growth parameters were conducted, since non-polar planes had not been studied in our group before. For example, homo- and hetero-epitaxy of GaN layers reveal that under N-rich condition surface kinetic roughening occurs, accompanied by characteristic growth anisotropy related to the crystal orientation. Besides, the heteroepitaxy of *a*-GaN on *r*-sapphire by MBE was studied too. Although the optical properties are slightly better than those of HVPE samples, possibly due to lower BSF density, the surface is much rougher, because the growth conditions are far from thermodynamic equilibrium when rather lower growth temperatures are used.

Then, GaN/AlGaN SQWs were deposited on HVPE ELO templates. It was confirmed that they are free from QCSE. Their emission linewidths are 20-40 meV, depending on the Al fraction and well width. Thin wells are more sensitive to interface-inhomogeneity-induced broadening. Exciton localization in QW is also observed. Both emission linewidths and localization energies are comparable to those of *c*-plane QWs, indicating good optical qualities. Meanwhile, a new effect emerges: LT μ-PL and TEM measurements demonstrate that the intersections of BSFs and SQWs behave like quantum-wire structures.

Next, AlN/GaN DBRs and nitride-based MC structures have been grown on *a*-plane HVPE ELO templates.[4] From the epitaxy point of view, GaN interlayers are under high compressive strains: ε_{yy} = -2% and ε_{zz} = -3% in $[1\bar{1}00]$ and [0001] directions, respectively. When characterizing the optical properties, the light is linearly polarized as a result of positive linear birefringence effect (*i.e.* $\Delta n = n_e - n_o > 0$). The peak reflectivity of 13-pair AlN/GaN DBR is around 95%, close to that of *c*-plane. Nitride-based MC with a λ empty GaN cavity has been demonstrated for the first time. Two modes have been identified: with the change of linear polarization angle from 0° (light polarization perpendicular to the *c*-axis) to 90° (light polarization parallel to the *c*-axis), the transmission peak switches from 384.5 nm to 390.2 nm. Both modes have a linewidth of ~ 4 nm (quality factor ~ 100). Although the quality factor is relatively lower than that of *c*-plane, this preliminary result is quite encouraging.

Perspectives

Nowadays, LEDs and LDs grown on non-polar GaN templates are attracting more and more attention from not only research institutions[5,6] but also industry field[7], in an effort to push for longer wavelength and better performance. These devices are always demonstrated on free-standing templates that are, at least for the time being, small, expensive, and not suitable for wide commercial applications. Meanwhile, competition from conventional *c*-plane is tight.[8] Therefore, from the epitaxy point of view, future experimental studies will aim at the improvement of material quality. The growth window of *a*-plane is quite narrow due to intrinsic characteristics, so more efforts will be devoted to *m*-plane GaN grown on *m*-plane sapphire, which is cheaper and available in large scales compared to SiC or $LiAlO_2$. Defects reduction through modifications of growth procedures is one possible solution. Since the dislocation bending phenomenon occurred in *c*-plane does not apply to non-polar, we have to invent other mechanism. One possible solution is the insertion of an AlGaN interlayer, which was reported to introduce bending and coalescence of dislocations in the GaN layer grown upon it.[9] Even so, the reduction of BSFs is still a big issue since they always propagate vertically to the top surface.

Another aspect is to pursue room-temperature polariton lasing on non-polar nitride-based MCs. Such devices require high quality factor: both high reflectivity DBRs (> 99 %) and wide MQWs with low inhomogeneous broadening. Higher reflectivity means more pairs of stacking layers, a demanding task for strain engineering. Besides, if such structures are to be realized by MBE, the performance of MBE-grown MQWs needs improving. Overall, it is a challenging mission.

To some extent, my work is limited to eptiaxial growth of III-V nitride semiconductor materials and related characterizations. However, from a broader view, it is among the worldwide efforts aimed to improve the performance of nitride-based LEDs and LDs and to expand the emission wavelengths from blue to UV and green regions. I believe these targets are indeed challenging but quite achievable, and they will have significant influences not only in research and industry but in our daily life as well.

Bibliography

---

[1] T. Zhu, D. Martin, R. Butté, J. Napierala, and N. Grandjean, "*a*-plane GaN grown on *r*-plane sapphire substrates by hydride vapor phase epitaxy", *Journal of Crystal Growth*, vol. 300, pp. 186-189, 2007.

[2] T. Zhu, D. Martin, and N. Grandjean, "*M*-plane GaN grown on *m*-plane sapphire by hydride vapor phase epitaxy", *Japanese Journal of Applied Physics*, vol. 48, pp. 020556, 2009.

[3] P. Vennéguès, T. Zhu, J. M. Chauveau, Z. Bougrioua, D. Martin, J. Zuniga-Perez and N. Grandjean, "In-plane polarities of nonpolar wurtzite epitaxial films deposited on M- and R-plane sapphire substrates", accepted by *Japanese Journal of Applied Physics.*

[4] T. Zhu, A. Dussaigne, G. Christmann, C. Pinquier, E. Feltin, D. Martin, R. Butte, and N. Grandjean, "Nonpolar GaN-based microcavity using AlN/GaN distributed Bragg reflector", *Applied Physics Letters*, vol. 92, pp. 061114, 2008.

[5] K. Okamoto, H. Ohta, S. F. Chichibu, J. Ichihara, and H. Takasu, "Continuous-wave operations of m-plane InGaN quantum well laser diodes", *Japanese Journal of Applied Physics*, vol. 46, pp. L187-L189, 2007.

---

[6] K. M. Kelchner, Y-D. Lin, M. T. Hardy, C. Y. Huang, P. S. Hsu, R. M. Farrell, D. A. Haeger, H. C. Kuo, F. Wu, K. Fujito, D. A. Cohen, A. Chakraborty, H. Ohta, J. S. Speck, S. Nakamura, and S. P. DenBaars, “Nonpolar AlGaN-cladding-free blue laser diodes with InGaN waveguiding”, *Applied Physics Express*, vol. 2, pp. 071003, 2009.

[7] K. Okamoto, J. Kashiwagi, T. Tanaka, and M. Kubota, “Nonpolar m-plane InGaN multiple quantum well laser diodes with a lasing wavelength of 499.8 nm”, *Applied Physics Letters*, vol. 94, pp. 071105, 2009.

[8] T. Miyoshi, S. Masui, T. Okada, T. Yanamoto, T. Kozaki, S. Nagahama, and T. Mukai, “510-515 nm InGaN-based green laser diodes on *c*-plane GaN substrate”, *Applied Physics Express*, vol. 2, pp. 062201, 2009.

[9] M. Imura, A. Hoshino, K. Nakano, M. Tsuda, M. Iwaya, S. Kamiyama, H. Amano, and I. Akasaki, “Flat $(11\bar{2}0)$ GaN thin film on precisely offset-controlled $(1\bar{1}02)$ sapphire substrate”, *Japanese Journal of Applied Physics*, vol. 44, pp. 7418-7420, 2005.

Acknowledgements

First of all, I would like to express my warmest gratitude to Professor Nicolas Grandjean, my thesis advisor, for providing the rare opportunity to conduct my doctoral research at LASPE/IPEQ/EPFL, and his instructive discussions and sincere encouragements. Particularly, my work benefits hugely from the free research environment and comprehensive team organization that he endeavors to develop and preserve.

I would have never been able to learn so much hands-on experience of HVPE and MBE without the remarkable support from my colleagues – research engineer Denis Martin and scientific collaborator Amélie Dussaigne. They have also generously passed on those “little secrets” of III-nitrides epitaxy to me, a green hand, in the past four years. Besides, my relatively limited knowledge about MOVPE is attributed to Eric Feltin and Jean-François Carlin.

Material characterization is an essential part of my research. Therefore, my warm thanks go to Raphaël Butté, Dobri (Dob) Simeonov, Gabriel Christmann, Nicolay Sylvain, Jacques Levrat for their strong support in spectroscopy (both PL and reflectance). Especially, without the delicate “home-made” µ-PL setup built by Dob and others, some nice pictures in this thesis would be missing. For TEM measurement, many thanks go to Yadira Arroyo from Professor Pierre Stadelmann’s group at CIME EPFL and Philippe Vennéguès at CRHEA-CNRS (France). The task has been quite demanding while their results are more than satisfactory. I also thank Pierre Corfdir and Jean-Daniel Ganiere (LOEQ EPFL) for their timely CL results, Jean-François Carlin and Daniel Ariosa (LNNME EPFL) for their experience in XRD, and Benjamin Dwir (LPN EPFL) for his instructions of AFM and SEM. In addition, discussions with Marcus Gonschorek and Marcel Py are very fruitful.

Some experiments have been conducted in the clean rooms of LASPE and CMI. I appreciate very much the technical assistance from Antonino Castiglia, Julien Dorsaz, Nicolas Leiser, Damien and Yoan Trolliet, Hans-Jörg Bühlmann, Cyrille Hibert and Yvan Deillon (CMI EPFL).

Furthermore, I would like to thank numerous people at IPEQ for creating a pleasant research atmosphere. I can only mention some of them: Aline Gruaz, Gatien Cosendey, Samuel Sonderegger, Nils Kaufmann, Alexei Altoukhov, Rémy Sachot, Roger Rochat, Mauro Mosca, Luca Sulmoni…

Finally, I am grateful to my friends and family for all their moral support during this work.

Publications

- Philippe Vennéguès, Tiankai Zhu, Zahia Bougrioua, Denis Martin, Jesus Zuniga-Perez, and N. Grandjean, “In-plane polarities of nonpolar wurtzite epitaxial films deposited on *M*- and *R*-plane sapphire substrates”, *Japanese Journal of Applied Physics*, vol. 48, pp. 090211, 2009.

- Tiankai Zhu, Denis, Martin, and Nicolas Grandjean, “*M*-plane GaN grown on *m*-plane sapphire by hydride vapor phase epitaxy”, *Japanese Journal of Applied Physics*, vol. 48, pp. 020556, 2009.

- P. Corfdir, J. Ristič, P. Lefebvre, T. Zhu, D. Martin, A. Dussaigne, J. D. Ganière, N. Grandjean, and B. Deveaud-Plédran, “Low-temperature time-resolved cathodoluminescence study of exciton dynamics involving basal stacking faults in a-plane GaN”, *Applied Physics Letters*, vol. 94, pp. 201115, 2009.

- P. Corfdir, P. Lefebvre, J. Levrat, A. Dussaigne, J.-D. Ganiere, D. Martin, J. Ristic, T. Zhu, N. Grandjean, and B. Deveau-Pledran, “Exciton localization on basal stacking faults in *a*-plane epitaxial lateral overgrowth GaN grown by hydride vapor phase epitaxy”, *Journal of Applied Physics*, vol. 105, pp. 043102, 2009.

- T. Zhu, A. Dussaigne, G. Christmann, C. Pinquier, E. Feltin, D. Martin, R. Butte, and N. Grandjean, “Nonpolar GaN-based microcavity using AlN/GaN distributed Bragg reflector”, *Applied Physics Letters*, vol. 92, pp. 061114, 2008.

- T. Zhu, D. Martin, R. Butte, J. Napierala, and N. Grandjean, “*a*-plane GaN grown on *r*-plane sapphire substrates by hydride vapor phase epitaxy”, *Journal of Crystal Growth*, vol. 300, pp. 186-189, 2007.

- D. Simeonov, E. Feltin, H.-J. Buhlmann, T. Zhu, A. Castiglia, M. Mosca, J.-F. Carlin, R. Butte, and N. Grandjean, “Blue lasing at room temperature in high quality factor GaN/AlN microdisks with InGaN quantum wells”, *Applied Physics Letters*, vol. 90, pp. 061106, 2007.

- Fredrik Olsson, Tiankai Zhu, Gael Mion, and Sebastian Lourdudoss, “Large mask area effects in selective area growth”, *Journal of Crystal Growth*, vol. 289, pp. 24-30, 2006.

Conferences

- 8th International Conference on Nitride Semiconductors (ICNS), Jeju, South Korea, 2009.

  "Study of non-polar and semi-polar GaN grown on *m*-plane sapphire by HVPE: surface treatment and misorientation", poster presentation.

- International Workshop on Nitride semiconductors (IWN), Montreux, Switzerland, 2008.

  "*m*-plane GaN directly grown on *m*-plane sapphire by hydride vapor phase epitaxy", poster presentation.

- 7th ICNS, Las Vegas, United States, 2007.

  "Non-polar a-plane GaN grown on r-plane sapphire by ammonia-source molecular beam epitaxy", poster presentation.

  "Non-polar *a*-plane AlN/GaN distributed Bragg reflectors", poster presentation.

- First International Symposium on Growth of III-Nitrides, Linköping, Sweden, 2006.

  "*a*-plane GaN directly grown on *r*-plane sapphire substrates by HVPE", poster presentation.

Curriculum Vitae

Tiankai ZHU

Gender: Male
Nationality: China
Date of birth: 1981.09.17
tkzhu917@gmail.com

Bâtiment 6, CH A3 494
Lausanne CH-1015, Switzerland
Cell phone: +41 797 486 985
Phone (work): +41 21 6934530

Education

(2005.08 – 2009.12) PhD student in Photonics

Ecole Polytechnique Fédérale de Lausanne (Swiss Federal Institute of Technology), Switzerland.

Thesis advisor: Prof. Nicolas Grandjean

(2003.08 – 2005.03) M.S., Electrical Engineering

Kungliga Tekniska Högskolan (Royal Institute of Technology), Sweden

(1999.08 – 2003.06) B.S., Electrical Engineering

Shanghai Jiao Tong University, China

Professional Experience

Ecole Polytechnique Fédérale de Lausanne, Switzerland

As research assistant, I grow non-polar *a*- and *m*-plane GaN planar and epitaxial lateral overgrowth templates on *r*- and *m*-plane sapphire substrates by HVPE, respectively. I also grow nano-structures on *a*- and *m*-plane templates by NH_3-source MBE. In addition, I am familiar with polar *c*-plane GaN growth by HVPE and MBE.

Kungliga Tekniska Högskolan, Sweden

I conducted computer simulation on the selective area growth technique of gallium arsenide using the software COMSOL FEMLAB.